LEVERAGING MULTI-MESSENGER ASTROPHYSICS FOR DARK MATTER SEARCHES

By

Daniel Nicholas Salazar-Gallegos

A DISSERTATION

Submitted to
Michigan State University
in partial fulfillment of the requirements
for the degree of

Physics—Doctor of Philosophy
Computational Mathematics in Science and Engineering—Dual Major

Today

ABSTRACT

I did Dark Matter with HAWC and IceCube. I also used Graph Neural Networks

ACKNOWLEDGMENTS

I love my friends. Thanks to everyone that helped me figure this out. Amazing thanks to the people at LANL who supported me. Eames, etc Dinner Parties Jenny and her child Kaydince Kirsten, Pat, Andrea Family. You're so far but so critical to my formation. Unconditional love. Roommate

TABLE OF CONTENTS

LIST OF TABLES . . . vii

LIST OF FIGURES . . . viii

LIST OF ABBREVIATIONS . . . xiv

CHAPTER 1 INTRODUCTION . . . 1

CHAPTER 2 DARK MATTER IN THE COSMOS . . . 2
2.1 Introduction . . . 2
2.2 Dark Matter Basics . . . 3
2.3 Evidence for Dark Matter . . . 4
2.4 Searching for Dark Matter: Particle DM . . . 11
2.5 Sources for Indirect Dark Matter Searches . . . 16
2.6 Multi-Messenger Dark Matter . . . 18

CHAPTER 3 MULTIMESSENGER ASTROPHYSICS: DETECTING HIGH ENERGY NEUTRAL MESSENGERS . . . 21
3.1 Introduction . . . 21
3.2 Charged Particles in a Medium . . . 21
3.3 Photons (γ) . . . 22
3.4 Neutrinos (ν) . . . 22
3.5 Opportunities to Combine for Dark Matter . . . 22

CHAPTER 4 HIGH ALTITUDE WATER CHERENKOV (HAWC) OBSERVATORY . . . 24
4.1 The Detector . . . 24
4.2 Events Reconstruction and Data Acquisition . . . 24
4.3 Remote Monitoring . . . 24

CHAPTER 5 ICECUBE NEUTRINO OBSERVATORY . . . 25
5.1 The Detector . . . 25
5.2 Events Reconstruction and Data Acquisition . . . 25
5.3 Northern Test Site . . . 25

CHAPTER 6 GLORY DUCK: MULTI-WAVELENGTH SEARCH FOR DARK MATTER ANNIHILATION TOWARDS DWARF SPHEROIDAL GALAXIES . . . 26
6.1 Introduction . . . 26
6.2 Dataset and Background . . . 28
6.3 Analysis . . . 29
6.4 Likelihood Methods . . . 34
6.5 HAWC Results . . . 40
6.6 Glory Duck Combined Results . . . 43
6.7 HAWC Systematics . . . 48

6.8 J-factor distributions 49
6.9 Discussion and Conclusions 55

CHAPTER 7 MULTITHREADING HAWC ANALYSES FOR DARK MATTER SEARCHES 59
7.1 Introduction 59
7.2 Dataset and Background 59
7.3 Analysis 60
7.4 Likelihood Methods 65
7.5 Computational Methods: Multithreading 65
7.6 Analysis Results 71

CHAPTER 8 HEAVY DARK MATTER ANNIHILATION SEARCH WITH ICE-CUBE'S NORTH SKY TRACK DATA 76

CHAPTER 9 NU DUCK 77

APPENDIX A MULTI-EXPERIMENT SUPPLEMENTARY FIGURES 78

APPENDIX B MULTITHREADING SUPPLEMENTARY FIGURES 79
B.1 `mpu_analysis.py` 80

BIBLIOGRAPHY 89

LIST OF TABLES

Table 6.1 Summary of the relevant properties of the dSphs used in the present work. Column 1 lists the dSphs. Columns 2 and 3 present their heliocentric distance and galactic coordinates, respectively. Columns 4 and 5 report the J-factors of each source given from the $\mathcal{GS}$ and $\mathcal{B}$ independent studies and their estimated $\pm 1\sigma$ uncertainties. The values $\log_{10} J$ ($\mathcal{GS}$ set) [45] correspond to the mean J-factor values for a source extension truncated at the outermost observed star. The values $\log_{10} J$ ($\mathcal{B}$ set) [47] are provided for a source extension at the tidal radius of each dSph. **Bolded sources are within HAWC's field of view and provided to the Glory Duck analysis.** 34

Table 6.2 Summary of dSph observations by each experiment used in this work. A '-' indicates the experiment did not observe the dSph for this study. For Fermi-LAT, the exposure at 1 GeV is given. For HAWC, $|\Delta\theta|$ is the absolute difference between the source declination and HAWC latitude. HAWC is more sensitive to sources with smaller $|\Delta\theta|$. For IACTs, we show the zenith angle range, the total exposure, the energy range, the angular radius θ of the signal or ON region, the ratio of exposures between the background-control (OFF) and signal (ON) regions (τ), and the significance of gamma-ray excess in standard deviations, σ. 35

Table 7.1 Summary of the relevant properties of the dSphs used in the present work. Column 1 lists the dSphs. Columns 2 and 3 present their heliocentric distance and galactic coordinates, respectively. Column 4 reports the J-factors of each source given from the $\mathcal{LS}$ studies and estimated $\pm 1\sigma$ uncertainties. The values $\log_{10} J$ ($\mathcal{LS}$ set) [65] correspond to the mean J-factor values for a source extension truncated at 0.5°. 63

Table 7.2 Timing summaries for analyses for serial and multithreaded processes. M tasks is the number of functional-parallel tasks ran for the computation. $T_{p,c}$ is a single run time in hours:minutes:seconds for runs utilizing p nodes and c threads. Runs are run interactively on the same computer to maximize consistency. Empty entries are indicated with '-'. $(\cdot)$ entries are estimated entries extrapolated from data earlier in the column. 69

Table 7.3 Speed up summaries for analyses for serial and multithreaded processes. M tasks is the number of functional-parallel tasks ran for the computation. $S_{p,c}$ is a single speedup comparison for runs utilizing p nodes and c threads. $[\cdot]$ are the estimated speedups calculated from Tab. 7.2, Eq. (7.10), and Eq. (7.5). Empty entries are indicated with '-'. 71

Proof I know how to include

LIST OF FIGURES

Figure 2.1 Rotation curve fit to NGC 6503 from [7]. Dashed line is the contribution from visible matter. Dotted curves are from gas. Dash-dot curves are from dark matter (DM). Solid line is the composite contribution from all matter and DM sources. Data are indicated with bold dots with error bars. Data agree strongly with a matter + DM composite prediction. 5

Figure 2.2 Light from distant galaxy is bent in unique ways depending on the distribution of mass between the galaxy and Earth. Yellow dashed lines indicate where the light would have gone if the matter were not present [8]. 7

Figure 2.3 (left) Optical image of galactic cluster 1E0657-558. (right) X-ray image of the cluster with redder meaning hotter and higher baryon density. (both) Green contours are reconstruction of gravity contours from weak lensing. White rings are the best fit mass maxima at 68.3%, 95.5%, and 99.7% confidence. The matter maxima of the clusters are clearly separated from x-ray maxima. [9] 8

Figure 2.4 Plank CMB sky. Sky map features small variations in temperature in primordial light. These anisotropies are used to make inferences about the universe's energy budget and developmental history. [10] 9

Figure 2.5 Observed Cosmic Microwave Background power spectrum as a function of multipole moment from Plank [10]. Blue line is best fit model from Λ**CDM**. Red points and lines are data and error, respectively. 10

Figure 2.6 Predicted power spectra of CMB for different $\Omega_m h^2$ values for fixed baryon density from [11]. (left) Low $\Omega_m h^2$ increases the prominence of first and second peaks. (middle) $\Omega_m h^2$ is most similar to the observed power spectrum. The second and third peaks are similar in height. (right) $\Omega_m h^2$ is large which suppresses the first peak and raises the prominence of the third peak. 10

Figure 2.7 The Standard Model (SM) of particle physics. Figure taken from http://www.quantumdiaries.org/2014/03/14/the-standard-model-a-beautiful-but-flawed-theory/ 12

Figure 2.8 Simplified Feynman diagram demonstrating with different ways DM can interact with SM particles. The 'X's refer to the DM particles whereas the SM refer to fundamental particles in the SM. The large circle in the center indicates the vertex of interaction and is purposely left vague. The colored arrows refer to different directions of time as well as their respective labels. The arrows indicate the initial and final state of the DM -SM interaction in time. 13

Figure 2.9 A single jet event in ATLAS detector from 2017 [16]. Jet momentum was observed to be 1.9 TeV. Missing transverse momentum was observed to be 1.9 TeV compared to the initial transverse momentum of the event was 0. Implied MET is traced by a red dashed line in event display. 14

Figure 2.10 More detailed pseudo-Feynman diagram of particle cascade from dark matter annihilation into 2 quarks. The quarks hadronize and down to stable particles like γ or the anti-proton (p^-). Diagram pulled from ICRC 2021 presentation on DM annihilation search [17]. 15

Figure 2.11 Dark Matter (DM) decay spectrum for $b\bar{b}$ initial state and γ final state. Redder spectra are for larger DM masses. Bluer spectra are light DM masses. x is a unitless factor defined as the ratio of the mass of DM, m_χ, and the final state particle energy E_γ. Figure from [19]. 17

Figure 2.12 Different dark matter density profiles compared. Some models produce exceptionally large densities at small r [20]. 18

Figure 2.13 The Milky Way Galaxy in photons (γ) and neutrinos (ν) [22]. The Galactic center is at l=0°and is the brightest region in all panels. (top) An Optical color image of the Milky Way galaxy seen from Earth. Clouds of gas and dust obscure some light from stars. (2nd down) Integrated flux of γ-rays observed by the Fermi-LAT telescope [23]. (middle) Expected neutrino emission that corresponds with Fermi-LAT observations. (2nd up) Expected neutrino emission profile after considering detector systematics of IceCube. (bottom) Observed neutrino emission from region of the galactic plane. Substantial neutrino emission was detected. 19

Figure 2.14 Dark Matter annihilation spectra for different final state particle and standard model annihilation channels [24]. Photons (red), $e^\pm$ (green), $\bar{p}$ (blue), ν (black). 20

Figure 3.1 TODO: Show a nuclear reactor with cherenkov radiation[NEEDS A SOURCE][FACT CHECK THIS] 22

Figure 3.2 TODO: absorption spectrum of liquid and solid water[NEEDS A SOURCE][FACT CHECK THIS] 23

Figure 6.1 Sensitivities of five gamma-ray experiments compared to percentages of the Crab nebula's emission and dark matter annihilation. Solid lines present estimated sensitivities to power law spectra [FACT CHECK THIS]for each experiment. Green lines are Fermi-LAT sensitivities where lighter green is the sensitivity to the galactic center and dark green is its sensitivity to higher declinations. Orange, red, and purple solid lines represent the MAGIC, HESS, and VERITAS 50 hour sensitivities respectively. The maroon and brown lines are the HAWC 1 year and 5 year sensitivities. Across four decades of gamma-ray energy, these experiments have similar sensitivities on the order 10^{-12} erg $cm^{-2}s^{-1}$. The dotted lines are estimated dark matter fluxes assuming m_χ = 5 TeV DM annihilating to bottom quarks (red), tau leptons (blue), and W bosons (green). Faded gray lines outline percentage flux of the Crab nebula. Figure is an augmented version of [25] 27

Figure 6.2 Effect of Electroweak (EW) corrections on expected DM annihilation spectrum for $\chi\chi \rightarrow W^- W^+$. Solid lines are spectral models that consider EW corrections. Dash-dot lines are spectral models without EW corrections. Red lines are models for $M_\chi = 1$ TeV. Blue lines represent models for $M_\chi = 100$ TeV. All models are sourced from the PPPC4DMID [44]. 31

Figure 6.3 $\frac{dJ}{d\Omega}$ maps for Segue1 (top) and Coma Berenices (bottom). Origin is centered on the specific dwarf spheroidal galaxies (dSph). X and Y axes are the angular separation from the center of the dwarf. Plots of the remaining 11 dSph HAWC studied are linked in Fig. A.1. 33

Figure 6.4 Illustration of the combination technique showing a comparison between $-2\ln\lambda$ provided by four instruments (colored lines) from the observation of the same dSph without any J nuisance and their sum, $i.e.$ the resulting combined likelihood (thin black line). According to the test statistics of Equation (6.6), the intersection of the likelihood profiles with the line $-2\ln\lambda$ = 2.71 indicates the 95% C.L. upper limit on $\langle\sigma v\rangle$. The combined likelihood (thin black line) shows a smaller value of upper limit on $\langle\sigma v\rangle$than those derived by individual instruments. We also show how the uncertainties on the J factor effects the combined likelihood and degrade the upper limit on $\langle\sigma v\rangle$(thick black line). All likelihood profiles are normalized so that the global minimum $\widehat{\langle\sigma v\rangle}$ is 0. We note that each profile depends on the observational conditions in which a target object was observed. The sensitivity of a given instrument can be degraded and the upper limits less constraining if the observations are performed in non-optimal conditions such as a high zenith angle or a short exposure time. 38

Figure 6.5 HAWC upper limits at 95% confidence level on $\langle\sigma v\rangle$versus DM mass for seven annihilation channels, using the set of J-factors from Ref. [53] The solid line represents the observed combined limit. Dashed lines represent limits from individual dSphs. 41

Figure 6.6 HAWC TS values for best fit $\langle\sigma v\rangle$ versus m_χ for seven SM annihilation channels with J factors from $\mathcal{GS}$. The solid black line shows the combined best fit TS values. The colored, dashed lines are the TS values for each of the 13 sources HAWC studied. 42

Figure 6.7 HAWC Brazil bands at 95% confidence level on $\langle\sigma v\rangle$versus DM mass for seven annihilation channels with J-factors from $\mathcal{GS}$ [53]. The solid line represents the combined limit from 13 dSphs. The dashed line is the expected limit. The green band is the 68% containment. The yellow band is the 95% containment. 43

Figure 6.8 Upper limits at 95% confidence level on $\langle\sigma v\rangle$in function of the DM mass for eight annihilation channels, using the set of J factors from Ref. [53] ($\mathcal{GS}$ set in Table 6.1). The black solid line represents the observed combined limit, the black dashed line is the median of the null hypothesis corresponding to the expected limit, while the green and yellow bands show the 68% and 95% containment bands. Combined upper limits for each individual detector are also indicated as solid, colored lines. The value of the thermal relic cross-section in function of the DM mass is given as the red dotted-dashed line [54]. 44

Figure 6.9 Same as Fig. 6.8, using the set of J factors from Ref. [47, 55] ($\mathcal{B}$ set in Table 6.1). 45

Figure 6.10 Comparisons of the combined limits at 95% confidence level for each of the eight annihilation channels when using the J factors from Ref. [53] ($\mathcal{GS}$ set in Table 6.1), plain lines, and the J factor from Ref. [47, 55] ($\mathcal{B}$ set in Table 6.1), dashed lines. The cross-section given by the thermal relic is also indicated [54]. 47

Figure 6.11 Comparisons of the combined limits at 95% confidence level for a point source analysis and extended source using [53] $\mathcal{GS}$ J-factor distributions and PPPC [44] annihilation spectra. Shown are the limits for Segue1 which will have the most significant impact on the combined limit. 6 of the 7 DM annihilation channels are shown. Solid lines are extended source studies. Dashed lines are point source studies. Overall, the extended source analysis improves the limit by a factor of 2. 49

Figure 6.12 Same as Fig. 6.11 on Coma Berenices. This dSph also contributes significantly to the limit. The limits are identical in this case. 50

Figure 6.13 Comparison of combined limits when correcting for HAWC's pointing systematic. All DM annihilation channels are shown. The solid black line is the ratio between published limit to the declination corrected limit. The blue solid line or "Combined_og" represented the limits computed for Glory Duck. The solid orange line or "Combined_ad" represented the limits computed after correcting for the pointing systematic. 51

Figure 6.14 Differential map of dJ/Ω from model built in Section 6.8.1 and profiles provided directly from authors. (Top) Differential from Segue1. (bottom) Differential from Coma Berenices. Note that their scales are not the same. Segue1 shows the deepest discrepancies which is congruent with its large uncertainties. Both models show anuli where unique models become apparent. . . 52

Figure 6.15 HAWC limits for Coma Berenices (top) and Segue1 (bottom) for two different map sets. Blue lines are limits calculated on maps with poor model representation. Orange lines are limits calculated on spatial profiles provided by the authors of [45]. Black line is the ratio of the poor spatial model limits to the corrected spatial models. The left y-axis measures $\langle \sigma v \rangle$for the blue and orange lines. The right y-axis measures the ratio and is unitless. 53

Figure 6.16 Comparisons between the J-factors versus the angular radius for the computation of J factors from Ref. [53] ($\mathcal{GS}$ set in Table 6.1) in blue and for the computation from Ref. [47, 55] ($\mathcal{B}$ set in Tab. 6.1) in orange. The solid lines represent the central value of the J-factors while the shaded regions correspond to the 1σ standard deviation. 56

Figure 6.17 Comparisons between the J-factors versus the angular radius for the computation of J factors from Ref. [53] ($\mathcal{GS}$ set in Tab. 6.1) in blue and for the computation from Ref. [47, 55] ($\mathcal{B}$ set in Tab. 6.1) in orange. The solid lines represent the central value of the J-factors while the shaded regions correspond to the 1σ standard deviation. 57

Figure 7.1 Difference between spectral hypotheses from PPPC [44] and HDM [64]. Shown is the expected DM annihilation spectrum for $\chi\chi \to W^-W^+$. Solid lines are spectral models with EW corrections from the PPPC. Dash-dot lines are spectral models from HDM. Red lines are models for $M_\chi = 1$ TeV. Blue lines represent models for $M_\chi = 100$ TeV. 62

Figure 7.2 Photon spectra for $\chi\chi \to \gamma\gamma$ (left) and $\chi\chi \to ZZ$ (right) after gaussian convolution of line features. Both spectra have δ-features at photon energies equal to the DM mass. Bluer lines are annihilation spectra with lower DM mass. Redder lines are spectra from larger DM mass. All Spectral models are sourced from the Heavy Dark Matter models [64]. Axes are drawn roughly according to the energy sensitivity of HAWC. 63

Figure 7.3 $\frac{dJ}{d\Omega}$ maps for Coma Berenices, Draco, Segue1, and Sextans. Columns are divided for the $\pm 1\sigma$ uncertainties in $dJ/d\Omega$ around the mean value from $\mathcal{LS}$ [65]. Origin is centered on the specific dwarf spheroidal galaxies (dSph). θ and ϕ axes are the angular separation from the center of the dwarf 64

Figure 7.4 Infographic on how jobs and DM computation was organized in Section 6.3. Jobs were built for each permutation of `CHANS` and `SOURCES` shown by the left block in the figure. Each job, which took on the order 2 hrs to compute, had the following work flow: 1. Import HAWC analysis software, 2 min to run. 2. Load HAWC count maps, 5 min to run. 3. Load HAWC energy and spatial resolutions, 4 min. 5. Load DM spatial source templates and spectral models, less than 1 s. 6. Perform likelihood fit on data and model, about 8 min per DM mass. 7. Write results to file, less than 1s. 66

Figure 7.5 Graphic of Gustafson parallel coding pattern. f_s is the fraction of a program, in time, spent on serial computation. f_p is the fraction of computing time that is parallelizable. T_p is the total time for a parallel program to run. T_1 is the total time for a parallel program to run if only 1 processor is allocated. P_N is the N-th processor where it's row is the computation the processor performs. The Gustafson pattern is most similar to what is implemented for this analysis. Figure is pulled from [67]. 67

Figure 7.6 Task chart for one multi-threaded job developed for this project. Green blocks indicate a shared resource across the threads AND computation performed serially. Red blocks indicate functional parallel processing within each thread. 3 threads are represented here, yet many more can be employed during the full analysis. Jobs are defined by the `SOURCE` as these require unique maps to be loaded into the likelihood estimator. The m_χ, `CHAN`, and $\langle\sigma v\rangle$ variables are entered into the thread pool and allocated as evenly as possible across the threads. 69

Figure 7.7 TODO: combined 95 results of new duck. See if we can include Draco[NEEDS A SOURCE][FACT CHECK THIS] 72

Figure 7.8 TODO: combined 95 results. There will definitely be 2[NEEDS A SOURCE][FACT CHECK THIS] 73

Figure 7.9 TODO: TS of analysis of results. See if we can include Draco[NEEDS A SOURCE][FACT CHECK THIS] 74

Figure 7.10 TODO: TS of analysis of results. There will definitely be 2[NEEDS A SOURCE][FACT CHECK THIS] 75

Figure A.1 Sister figure to Figure 6.3. Sources in the first row from left to right: Bootes I, Canes Venatici I, II. In second row: Draco, Hercules, Leo I. In the first row: Leo II, Leo IV, Sextans. In the final row: Ursa Major I, Ursa Major II. 78

Figure B.1 Sister figure to Figure 7.2 for remaining SM primary annihilation channels studied for this thesis. These did not require any post generation smoothing and so are directly pulled from [64] with a binning scheme most helpful for a HAWC analysis. 79

LIST OF ABBREVIATIONS

MSU Michigan State University

LANL Los Alamos National Laboratory

DM Dark Matter

SM Standard Model

HAWC High Altitude Water Cherenkov Observatory

dSph Dwarf Spheroidal Galaxy

CHAPTER 1

INTRODUCTION

Is the text not rendering right? Ah ok it knows im basically drafting the doc still

CHAPTER 2

DARK MATTER IN THE COSMOS

2.1 Introduction

The dark matter problem can be summarized in part by the following thought experiment.

Let us say you are the teacher for an elementary school classroom. You take them on a field trip to your local science museum and among the exhibits is one for mass and weight. The exhibit has a gigantic scale, and you come up with a fun problem for your class.

You ask your class, "What is the total weight of the classroom? Give your best estimation to me in 30 minutes, and then we'll check your guess on the scale. If your guess is within 10% of the right answer, we will stop for ice cream on the way back."

The students are ecstatic to hear this, and they get to work. The solution is some variation of the following strategy. The students should give each other their weight or best guess if they do not know. Then, all they must do is add each student's weight and get a grand total for the class. The measurement on the giant scale should show the true weight of the class. When comparing the measured weight to your estimation, multiply the measurement by 1.0 ±0.1 to get the ±10% tolerances for your estimation.

Two of your students, Sandra and Mario, return to you with a solution.

They say, "We weren't sure of everyone's weight. We used 65 lbs. for the people we didn't know and added everyone who does know. There are 30 of us, and we got 2,000 lbs.! That's a ton!"

You estimated 1,900 lbs. assuming the average weight of a student in your class was 60 lbs. So, you are pleased with Sandra's and Mario's answer. You instruct your students to all gather on the giant scale and read off the weight together. To all your surprise, the scale reads *10,000 lbs.*! 10,000 is significantly more than a 10% error from 2,000. In fact, it is approximately 5 times more massive than either your or your students' estimates. You think to yourself and conclude there must be something wrong with the scale. You ask an employee to check the scale and verify it is well calibrated. They confirm that the scale is in working order. You weigh a couple of students individually to assess that the scale is well calibrated. Sandra weighs 59 lbs., and Mario weighs

62 lbs., typical weights for their age. You then weigh each student individually and see that their weights individually do not deviate greatly from 60 lbs. So, where does all the extra weight come from?

This thought experiment serves as an analogy to the Dark Matter problem. The important substitution to make however is to replace the students with stars and the classroom with a galaxy, say the Milky Way. Individually the mass of stars is well measured and defined with the Sun as our nearest test case. However, when we set out to measure the mass of a collection of stars as large as galaxies, our well-motivated estimation is wildly incorrect. There simply is no way to account for this discrepancy except without some unseen, or dark, contribution to mass and matter in galaxies. I set out in my thesis to narrow the possibilities of what this Dark Matter could be.

This chapter is organized like the following. . . TODO: Text should look like ... Chapter x has blah blah blah.

2.2 Dark Matter Basics

Presently, a more compelling theory of cosmology that includes Dark Matter (DM) in order to explain a variety of observations is Λ **C**old **D**ark **M**atter, or Λ**CDM**. I present the evidence supporting Λ**CDM** in Section 2.3 yet discuss the conclusions of the Λ**CDM** model here. According to Λ**CDM** fit to observations on the Cosmic Microwave Background (CMB), DM is 26.8% of the universe's current energy budget. Baryonic matter, stuff like atoms, gas, and stars, contributes to 4.9% of the universe's current energy budget [1, 2, 3].

DM is dark; it does not interact readily with light at any wavelength. DM also does not interact noticeably with the other standard model forces (Strong and Weak) at a rate that is readily observed [3]. DM is cold, which is to say that the average velocity of DM is below relativistic speeds [1]. 'Hot' DM would not likely manifest the dense structures we observe like galaxies, and instead would produce much more diffuse galaxies than what is observed [3, 1]. DM is old; it played a critical role in the formation of the universe and the structures within it [1, 2].

Observations of DM have so far been only gravitational. The parameter space available to what DM could be therefore is extremely broad. The broad DM parameter space is iteratively tested in

DM searches by supposing a hypothesis that has not yet been ruled out and performing observations to test them. When the observations yield a null result, the parameter space is constrained further. I present some approaches for DM searches in Section 2.4.

2.3 Evidence for Dark Matter

Dark Matter (DM) has been a looming problem in physics for almost 100 years. Anomalies have been observed by astrophysicists in galactic dynamics as early as 1933 when Fritz Zwicky noticed unusually large velocity dispersion in the Coma cluster. Zwicky's measurement was the first recorded to use the Virial theorem to measure the mass fraction of visible and invisible matter in celestial bodies [4]. From Zwicky in [5], "*If this would be confirmed, we would get the surprising result that dark matter is present in much greater amount than luminous matter.*" Zwicky's and others' observation did not instigate a crisis in astrophysics because the measurements did not entirely conflict with their understanding of galaxies [4]. In 1978, Rubin, Ford, and Norbert measured rotation curves for ten spiral galaxies [6]. Rubin et al.'s 1978 publication presented a major challenge to the conventional understanding of galaxies that could no longer be dismissed by measurement uncertainties. Evidence has been mounting ever since for this exotic form of matter. The following subsections provide three compelling pieces of evidence in support of the existence of DM.

2.3.1 First Clues: Stellar Velocities

Zwicky, and later Rubin, measured the stellar velocities of various galaxies to estimate their virial mass. The Virial Theorem upon which these observations are interpreted is written as

$$2T + V = 0. \tag{2.1}$$

Where T is the kinetic energy and V is the potential energy in a self-gravitating system. The classical Newton's law of gravity from stars and gas was use for gravitational potential modeled in the observed galaxies:

$$V = -\frac{1}{2}\sum_{i}\sum_{j\neq 1}\frac{m_i m_j}{r_{ij}}. \tag{2.2}$$

Zwicky et al. measured just the velocities of stars apparent in optical wavelengths [5]. Rubin et al. added by measuring the velocity of the hydrogen gas via the 21 cm emission line of Hydrogen [6]. The velocities of the stars and gas are used to infer the total mass of galaxies and galaxy clusters via Equation (2.1). An inferred mass is obtained from the luminosity of the selected sources. The two inferences are compared to each other as a luminosity to mass ratio which typically yielded [1]

$$\frac{M}{L} \sim 400\frac{M_\odot}{L_\odot} \tag{2.3}$$

$M_\odot$ and $L_\odot$ referring to stellar mass and stellar luminosity, respectively. These ratios clearly indicate a discrepancy in apparent light and mass from stars and gas and their velocities.

Rubin et al. [6] demonstrated that the discrepancy was unlikely to be an underestimation of the mass of the stars and gas. The inferred "dark" mass was up to 5 times more than the luminous mass. This dark mass also needed to extend well beyond the extent of the luminous matter.

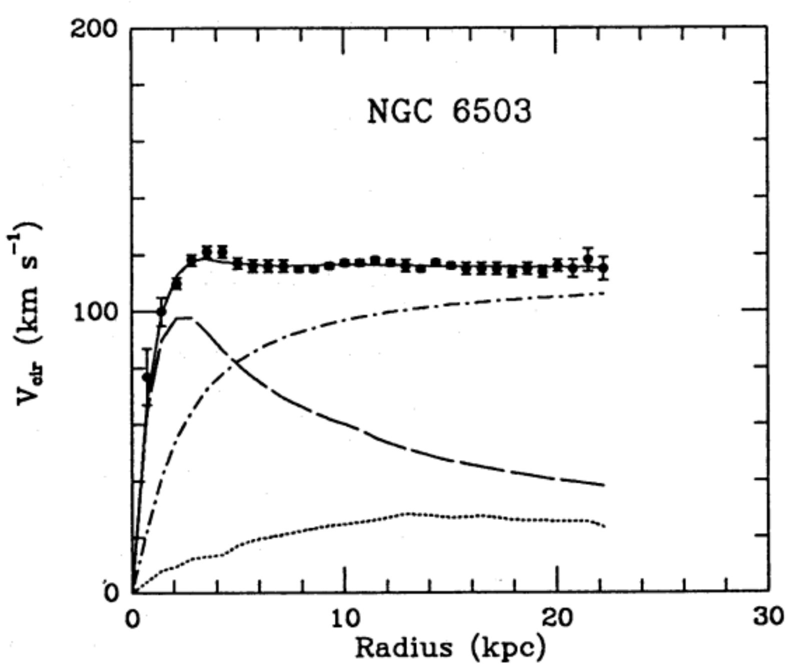

Figure 2.1 Rotation curve fit to NGC 6503 from [7]. Dashed line is the contribution from visible matter. Dotted curves are from gas. Dash-dot curves are from dark matter (DM). Solid line is the composite contribution from all matter and DM sources. Data are indicated with bold dots with error bars. Data agree strongly with a matter + DM composite prediction.

Figure 2.1 features one of many rotation curves plotted from the stellar velocities within galaxies.

The measured rotation curves mostly feature a flattening of velocities at higher radius which is not expected if the gravity was only coming from gas and luminous matter. The extension of the flat velocity region also indicates that the DM is distributed far from the center of the galaxy. Modern velocity measurements include significantly larger objects, galactic clusters, and smaller objects, dwarf galaxies. Yet, measurements along this regime are leveraging the Virial theorem with Newtonian potential energies. We know Newtonian gravity is not a comprehensive description of gravity. New observational techniques have been developed since 1978, and those are discussed in the following sections.

2.3.2 Evidence for Dark Matter: Gravitational Lensing

Modern evidence for dark matter comes from new avenues beyond stellar velocities. Gravitational lensing from DM is a new channel from general relativity. General relativity predicts aberrations in light caused by massive objects. In recent decades we have been able to measure the lensing effects from compact objects and DM halos. Figure 2.2 shows how different massive objects change the final image of a faraway galaxy resulting from gravitational lensing. Gravitational lensing developed our understanding of dark matter in two important ways.

Gravitational lensing provides additional compelling evidence for DM. The observation of two merging galactic clusters in 2006, shown in Figure 2.3, provided a compelling argument for DM outside the Standard Model. These clusters merged recently in astrophysical time scales. Galaxies and star cluster have mostly passed by each other as the likelihood of their collision is low. Therefore, these massive objects will mostly track the highest mass, dark and/or baryonic, density. Yet, the intergalactic gas is responsible for the majority of the baryonic mass in the systems [4]. These gas bodies will not phase through and will heat up as they collide together. The hot gas is located via x-ray emission from the cluster. Two observations of the clusters were performed independently of each other.

The first was the lensing of light around the galaxies due to their gravitational influences. When celestial bodies are large enough, the gravity they exert bends space and time itself. The warped space-time lenses light and will deflect in an analogous way to how glass lenses will bend

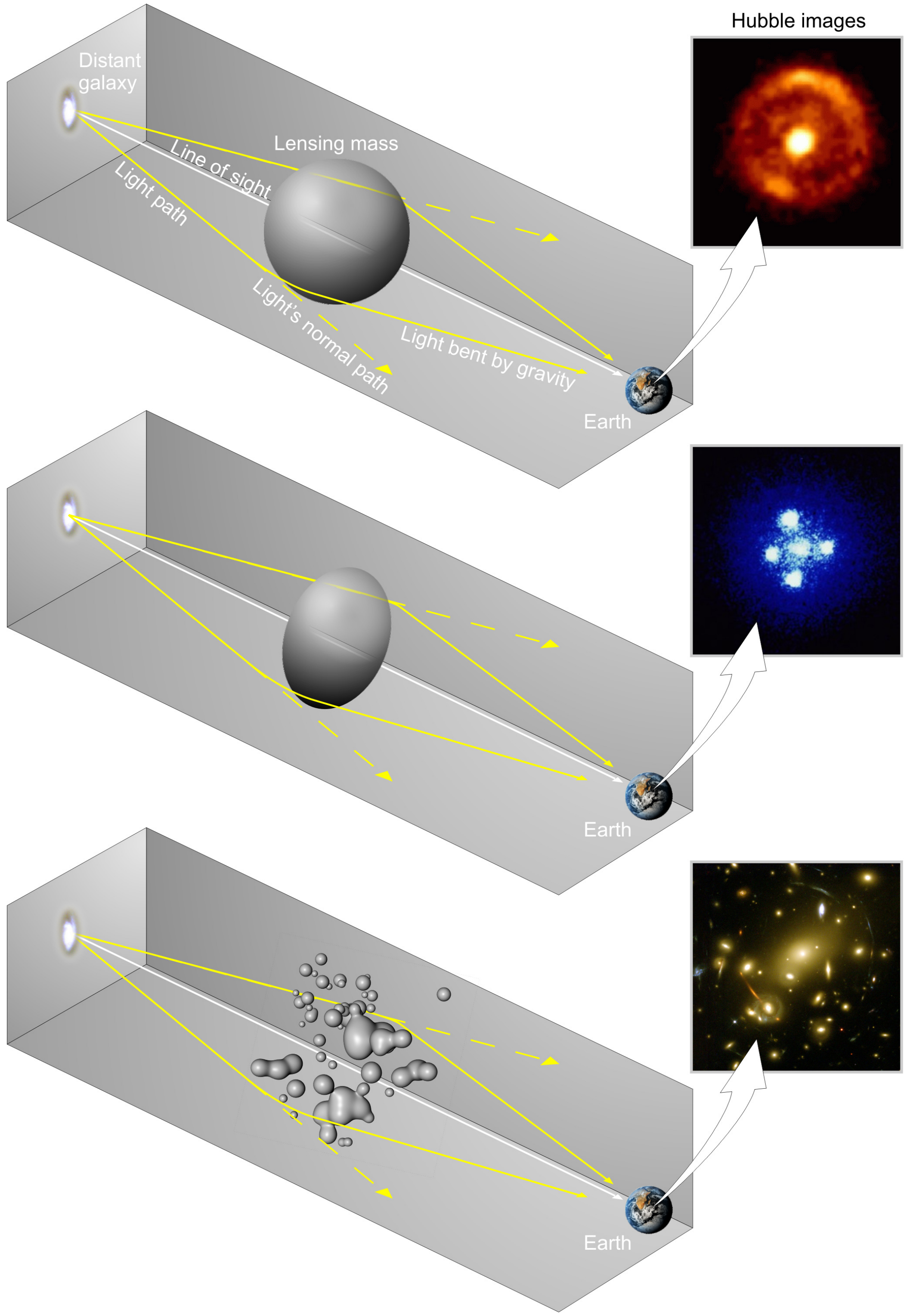

Figure 2.2 Light from distant galaxy is bent in unique ways depending on the distribution of mass between the galaxy and Earth. Yellow dashed lines indicate where the light would have gone if the matter were not present [8].

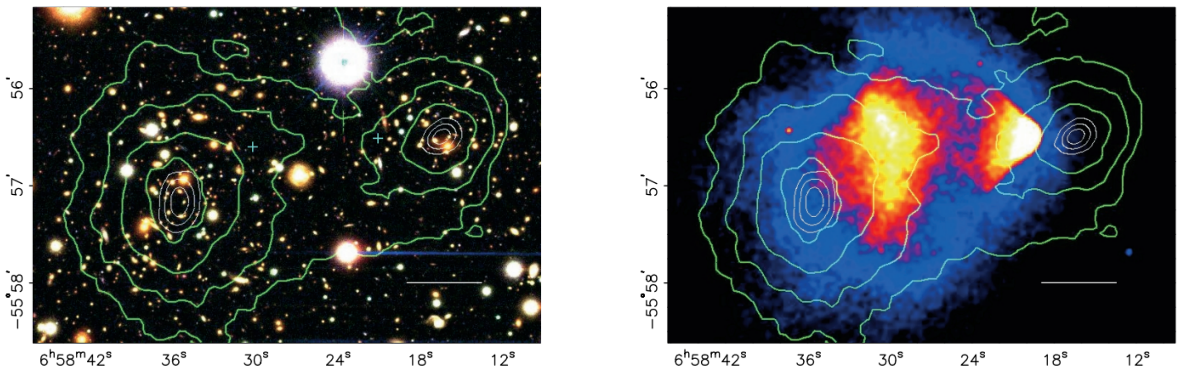

Figure 2.3 (left) Optical image of galactic cluster 1E0657-558. (right) X-ray image of the cluster with redder meaning hotter and higher baryon density. (both) Green contours are reconstruction of gravity contours from weak lensing. White rings are the best fit mass maxima at 68.3%, 95.5%, and 99.7% confidence. The matter maxima of the clusters are clearly separated from x-ray maxima. [9]

light, see Figure 2.2. With a sufficient understanding of light sources behind a massive object, we can reconstruct the contours of the gravitational lenses. The gradient of the contours shown in Figure 2.3 then indicates how dense the matter is and where it is.

The x-ray emission can then be observed from the clusters. Since these galaxies are mostly gas and are merging, then the gas should be getting hotter. If they are merging, the x-ray emissions should be the strongest where the gas is mostly moving through each other. Hence, X-ray emission maps out where the gas is in the merging galaxy cluster.

The lensing and x-ray observations were done on the Bullet cluster featured on Figure 2.3. The x-ray emissions do not align with the gravitational contours from lensing. The incongruence in mass density and baryon density suggests that there is a lot of matter somewhere that does not interact with light. Moreover, this dark matter cannot be baryonic [9]. The Bullet Cluster measurement did not really tell us what DM is exactly, but it did give the clue that DM also does not interact with itself very strongly. If DM did interact strongly with itself, then it would have been more aligned with the x-ray emission [9]. There have been follow-up studies of galaxy clusters with similar results. The Bullet Cluster and others like it provide a persuasive case against something possibly amiss in our gravitational theories.

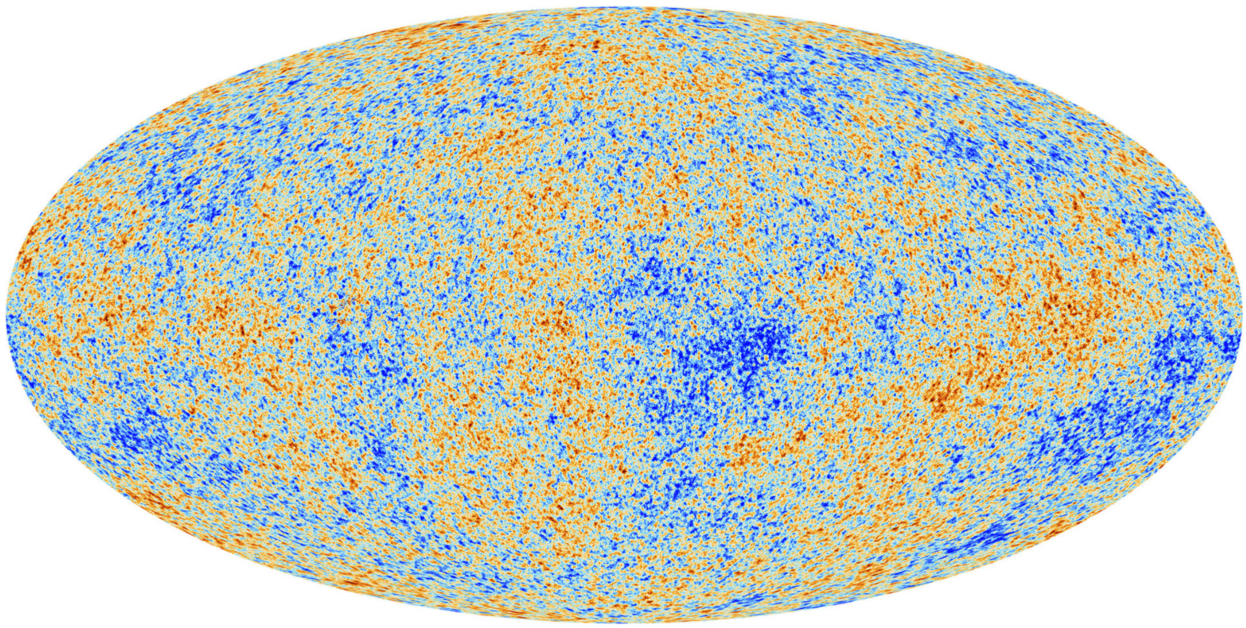

Figure 2.4 Plank CMB sky. Sky map features small variations in temperature in primordial light. These anisotropies are used to make inferences about the universe's energy budget and developmental history. [10]

2.3.3 Evidence for Dark Matter: Cosmic Microwave Background

The Cosmic Microwave Background (CMB) is the primordial light from the early universe when Hydrogen atoms formed from the free electron and proton soup in the early universe. The CMB is the earliest light we can observe; released when the universe was about 380,000 years old. Then we look at how the simulated universes look like compared to what we see. Figure 2.4 is the most recent CMB image from the Plank satellite after subtracting the average value and masking the galactic plane [10]. Redder regions indicate a slightly hotter region in the CMB, and blue indicates colder. The intensity variations are on the order of 1 in 1000 with respect to the average value.

The Cosmic Microwave Background shows that the universe had DM in it from an incredibly early stage. To measure the DM, Dark Energy, and matter fractions of the universe from the CMB, the image is analyzed into a power spectrum, which shows the amplitude of the fluctuations as a function of spherical multipole moments. Λ**CDM** provides the best fit to the power spectra of the CMB as shown in Figure 2.5. The CMB power spectrum is quite sensitive to the fraction of each energy contribution in the early universe. Low l modes are dominated by variations in gravitational potential. Intermediate l emerge from oscillations in photon-baryon fluid from

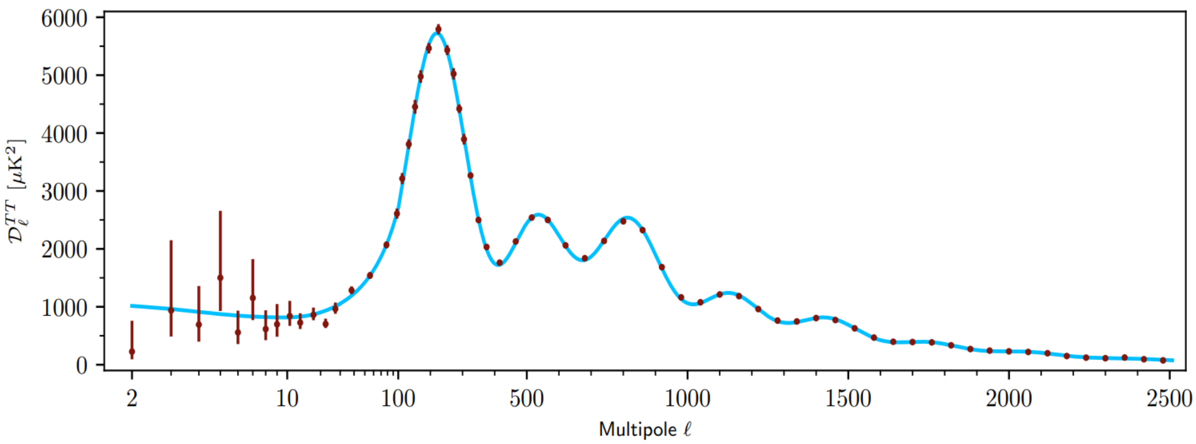

Figure 2.5 Observed Cosmic Microwave Background power spectrum as a function of multipole moment from Plank [10]. Blue line is best fit model from Λ**CDM**. Red points and lines are data and error, respectively.

competing baryon pressures and gravity. High l is a damped region from the diffusion of photons during electron-proton recombination. [1]

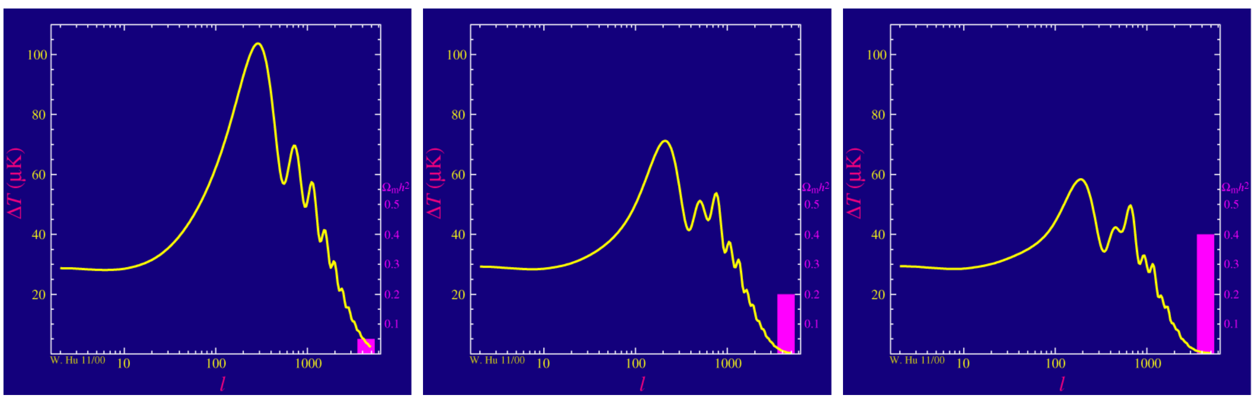

Figure 2.6 Predicted power spectra of CMB for different $\Omega_m h^2$ values for fixed baryon density from [11]. (left) Low $\Omega_m h^2$ increases the prominence of first and second peaks. (middle) $\Omega_m h^2$ is most similar to the observed power spectrum. The second and third peaks are similar in height. (right) $\Omega_m h^2$ is large which suppresses the first peak and raises the prominence of the third peak.

The harmonics would look quite different for a universe with less DM. Figure 2.6 demonstrates the effect $\Omega_m h^2$ has on the expected power spectrum for fixed baryon matter density. [11] Sweeping $\Omega_m h^2$ in this way clearly shows the effect dark matter has on the CMB power spectrum. The observations fit well with the Λ**CDM** model, and the derived fractions are as follows. The matter fraction: $\Omega_m = 0.3153$; and the baryon fraction: $\Omega_b = 0.04936$ [10]. Plank's observations also provide a measure of the Hubble constant, H_0. H_0 especially has seen a growing tension in the past decade that continues to deepened with observations from instruments like the James Webb Telescope [12, 13]. As Hubble tensions deepen, we may find that perhaps Λ**CDM**, despite its successes, is missing some critical physics.

Overall, the Newtonian motion of stars in galaxies, weak lensing from galactic clusters, and power spectra from primordial light form a compelling body of research in favor of dark matter. It takes another leap of theory and experimentation to make observations of DM that are non-gravitational in nature. In Section 2.3, the evidence for DM implies strongly that the DM is matter and not a lost parameter in the gravitational fields between massive objects. Finally, if we take one axiom: that this matter has quantum behavior, such as being described by some Bohr wavelength and abiding by some fermion or boson statistics; then we arrive at particle dark matter. One particle DM hypothesis is the Weakly Interacting Massive Particle (WIMP). This DM candidate theory is discussed further in the next section and is the focus of this thesis.

2.4 Searching for Dark Matter: Particle DM

Section 2.4 shows the Standard Model of particle physics and is currently the most accurate model for the dynamics of fundamental particles like electrons and photons. The current status of the SM does not have a viable DM candidate. When looking at the standard model, we can immediately exclude any charged particle because charged particles interact strongly with light. Specifically, this will rule out the following charged, fundamental particles: $e, \mu, \tau, W, u, d, s, c, t, b$ and their corresponding antiparticles. Recalling from Section 2.2 that DM must be long-lived and stable over the age of the universe which excludes all SM particles with decay half-lives at or shorter than the age of the universe. The lifetime constraint additionally eliminates the Z and H bosons. Finally, the candidate DM needs to be somewhat massive. Recall from Section 2.2 that DM is cold or not relativistic through the universe. This eliminates the remaining SM particles: $\nu_{e,\mu,\tau}, g, \gamma$ as DM candidates. Because there are no DM candidates within the SM, the DM problem strongly hints to physics beyond the SM (BSM).

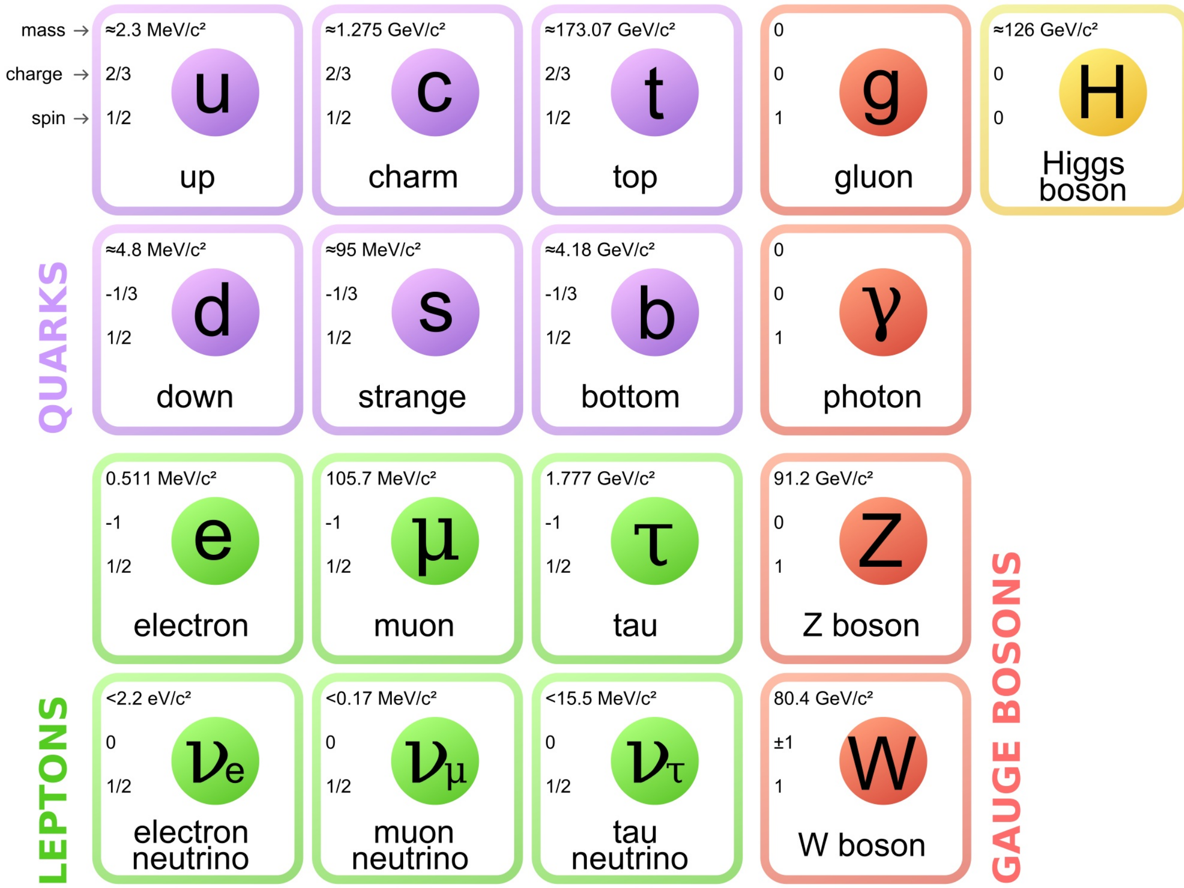

Figure 2.7 The Standard Model (SM) of particle physics. Figure taken from http://www.quantumdiaries.org/2014/03/14/the-standard-model-a-beautiful-but-flawed-theory/

2.4.1 Shake it, Break it, Make it

When considering DM that couples in some way with the SM, the interactions are roughly demonstrated by interaction demonstrated in Figure 2.8. The figure is a simplified Feynman diagram where the arrow of time represents the interaction modes of: **Shake it, Break it, Make it**.

Shake it refers to the direct detection of dark matter. Direct detection interactions start with a free DM particle and an SM particle. The DM and SM interact via elastic or inelastic collision and recoil away from each other. The DM remains in the dark sector and imparts some momentum onto the SM particle. The hope is that the momentum imparted onto the SM particle is sufficiently high enough to pick up with extremely sensitive instruments. Because we cannot create the DM in the lab, a direct detection experiment must wait until DM is incident on the detector. Most direct detection experiments are therefore placed in low-background environments with inert detection

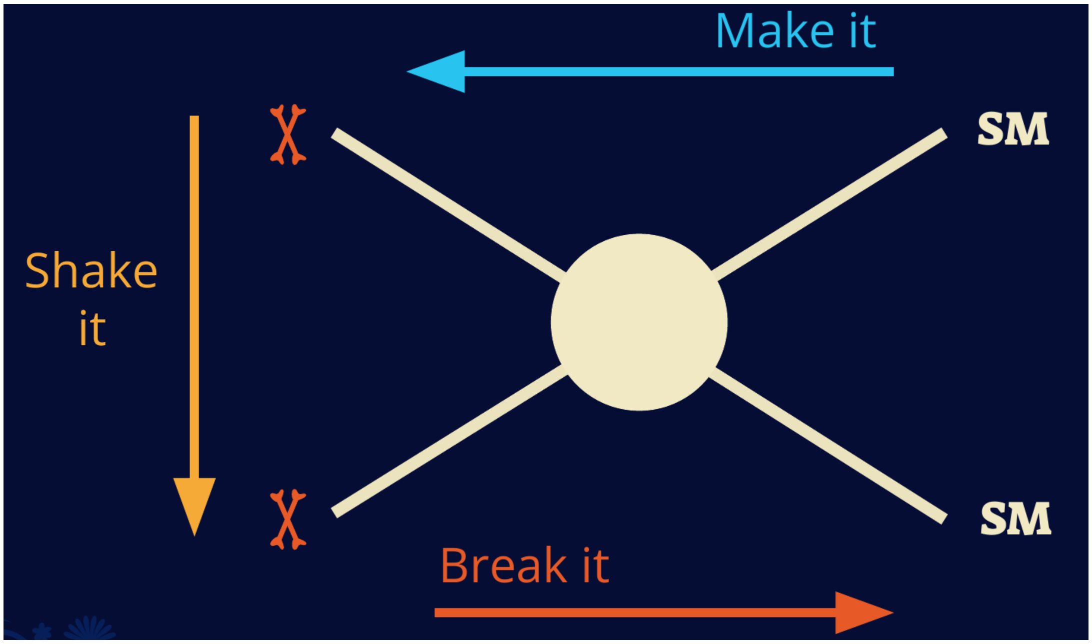

Figure 2.8 Simplified Feynman diagram demonstrating with different ways DM can interact with SM particles. The 'X's refer to the DM particles whereas the SM refer to fundamental particles in the SM. The large circle in the center indicates the vertex of interaction and is purposely left vague. The colored arrows refer to different directions of time as well as their respective labels. The arrows indicate the initial and final state of the DM -SM interaction in time.

media like the noble gas Xenon. [14]

Make it refers to the production of DM from SM initial states. The experiment starts with particles in the SM. These SM particles are accelerated to incredibly high energies and then collide with each other. In the confluence of energy, DM hopefully emerges as a byproduct of the SM annihilation. Often it is the collider experiments that are energetic enough to hypothetically produce DM. These experiments include the world-wide collaborations ATLAS and CMS at CERN where proton collide together at extreme energies. The DM searches, however, are complex. DM likely does not interact with the detectors and lives long enough to escape the detection apparatus of CERN's colliders. This means any DM production experiment searches for an excess of events with missing momentum or energy in the events. An example event with missing transverse momentum is shown in Figure 2.9. The missing momentum with no particle tracks implies a neutral particle carried the energy out of the detector. However, there are other neutral particles in the SM, like neutrons or neutrinos, so any analysis has to account for SM signatures of missing momentum. [15]

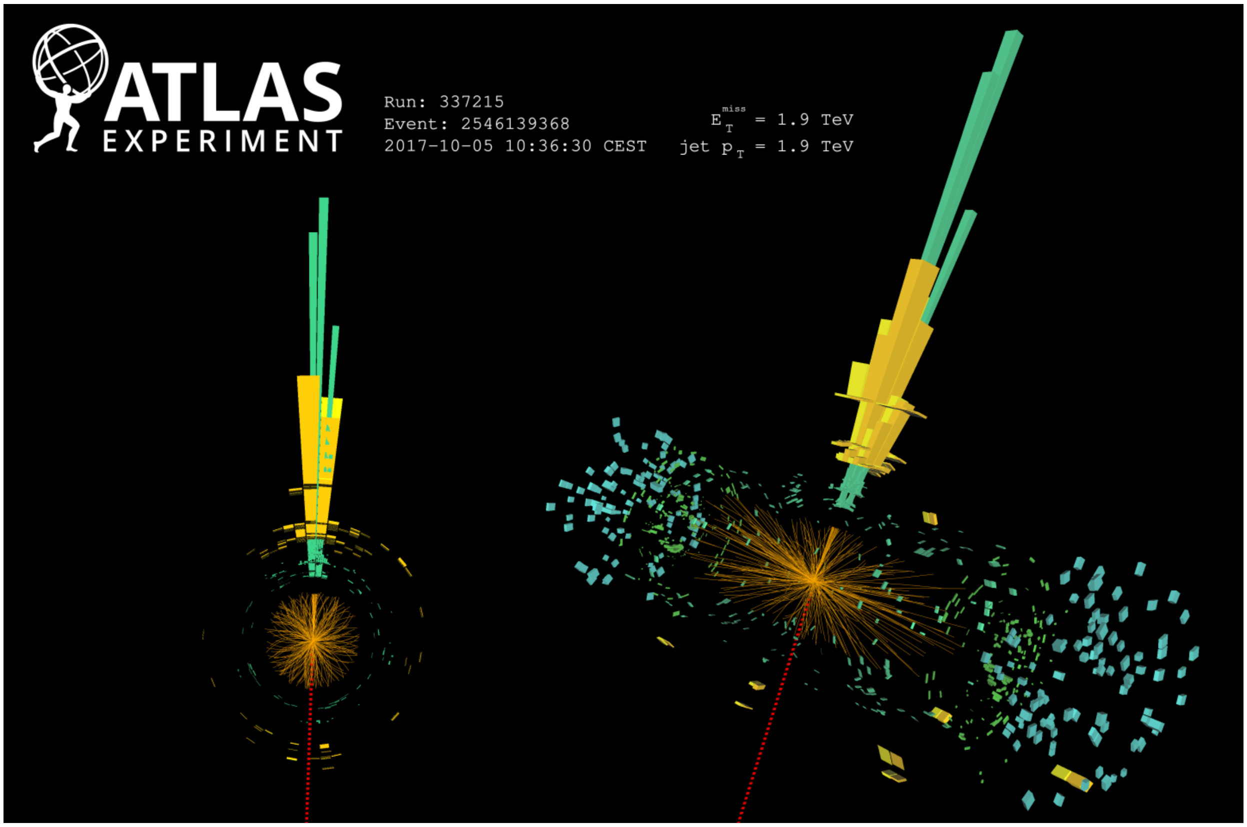

Figure 2.9 A single jet event in ATLAS detector from 2017 [16]. Jet momentum was observed to be 1.9 TeV. Missing transverse momentum was observed to be 1.9 TeV compared to the initial transverse momentum of the event was 0. Implied MET is traced by a red dashed line in event display.

2.4.2 Break it: Standard Model Signatures of Dark Matter through Indirect Searches

Break it refers to the creation of SM particles from the dark sector, and it is the primary focus of this thesis. The interaction begins with DM or in the dark sector. The hypothesis is that this DM will either annihilate with itself or decay and produce an SM byproduct. This method is often referred to as the Indirect Detection of DM because we have no lab to directly control or manipulate the DM. Therefore, most indirect DM searches are performed using observations of known DM densities among the astrophysical sources. The strength is that we have the whole of the universe and its 13.6-billion-year lifespan to use as a detector and particle accelerator. Additionally, locations of dark matter are well cataloged since it was astrophysical observations that presented the problem of DM in the first place.

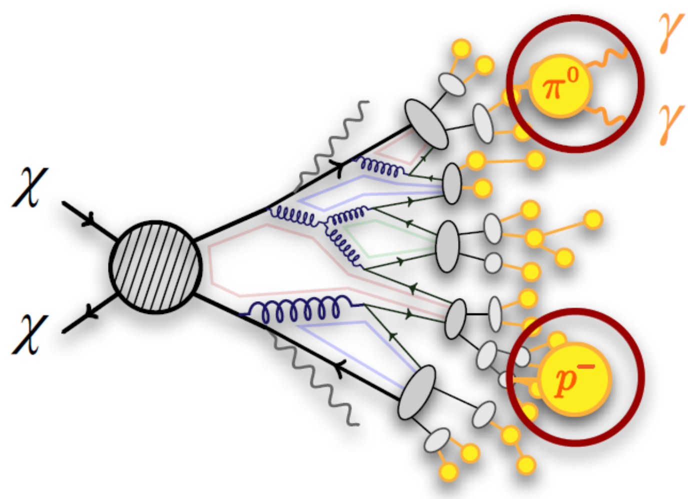

Figure 2.10 More detailed pseudo-Feynman diagram of particle cascade from dark matter annihilation into 2 quarks. The quarks hadronize and down to stable particles like γ or the anti-proton (p^-). Diagram pulled from ICRC 2021 presentation on DM annihilation search [17].

However, anything can happen in the universe. There are many difficult to deconvolve backgrounds when searching for DM. One prominent example is the galactic center. We know the galactic center has a large DM content because of stellar kinematics in our Milky Way and DM halo simulations. Yet, any signal from the galactic center is challenging to parse apart from the extreme environment of our supermassive black hole, unresolved sources, and diffuse emission from the interstellar medium [18]. Despite the challenges, any DM model that yields evidence in the other two observation methods, **Shake it or Make it** must be corroborated with indirect observations of the known DM sources. Without corroborating evidence, DM observation in the lab is hard-pressed to demonstrate that it is the model contributing to the DM seen at the universal scale.

In the case of WIMP DM, signals are described in terms of primary SM particles produced from DM decay or annihilation. The SM initial state particles are then simulated down to stable final states such as the γ, ν, p, or e which can traverse galactic lengths to reach Earth.

Figure 2.10 shows the quagmire of SM particles that emerges from SM initial states that are not stable [17]. There are many SM particles with varying energies that can be produced in such an interaction. For any arbitrary DM source and stable SM particle, the SM flux from DM annihilating to a neutral particle in the SM, ϕ, from a region in the sky is described by the following.

$$\frac{d\Phi_\phi}{dE_\phi} = \frac{\langle\sigma v\rangle}{8\pi m_\chi^2}\frac{dN_\phi}{dE_\phi} \times \int_{\text{source}} d\Omega \int_{l.o.s} \rho_\chi^2 dl(r,\theta') \tag{2.4}$$

n Equation (6.1), $\langle\sigma v\rangle$is the velocity-weighted annihilation cross-section of DM to the SM. m_χ refers to the mass of DM, noted with Greek letter χ. $\frac{dN_\phi}{dE_\phi}$ is the N particle flux weighted by the particle energy. An example is provided in Figure 2.11 for the γ final state. The integrated terms are performed over the solid angle, $d\Omega$, and line of sight, l.o.s. ρ is the density of DM for a location (r,θ') in the sky. The terms left of the '×' are often referred to as the particle physics component. The terms on the right are referred to as the astrophysical component. For decaying DM, the equation changes to...

$$\frac{d\Phi_\phi}{dE_\phi} = \frac{1}{4\pi\tau m_\chi}\frac{dN_\phi}{dE_\phi} \times \int_{\text{source}} d\Omega \int_{l.o.s} \rho_\chi dl(r,\theta') \tag{2.5}$$

n Equation (7.1), τ is the decay lifetime of the DM. Just as in Equation (6.1), the left and right terms are the particle physics and the astrophysical components respectively. The integrated astrophysical component of Equation (6.1) is often called the J-Factor. Whereas the integrated astrophysical component of Equation (7.1) is often called the D-Factor.

Exact DM DM → SM SM branching ratios are not known, so it is usually assumed to go 100% into an SM particle/anti-particle. Additionally, when a DM annihilation or decay produces one of the neutral, long-lived SM particles (ν or γ), the particle is traced back to a DM source. For DM above GeV energies, there are very few SM processes that can produce particles with such a high energy. Seeing such a signal would almost certainly be an indication of the presence of dark matter. Fortunately, the universe provides us with the largest volume and lifetime ever for a particle physics experiment.

2.5 Sources for Indirect Dark Matter Searches

The first detection of DM relied on optical observations. Since then, we have developed new techniques to find DM dense regions. As described in Section 2.3.1, many DM dense regions were through observing galactic rotation curves. Our Milky Way galaxy is among DM dense regions

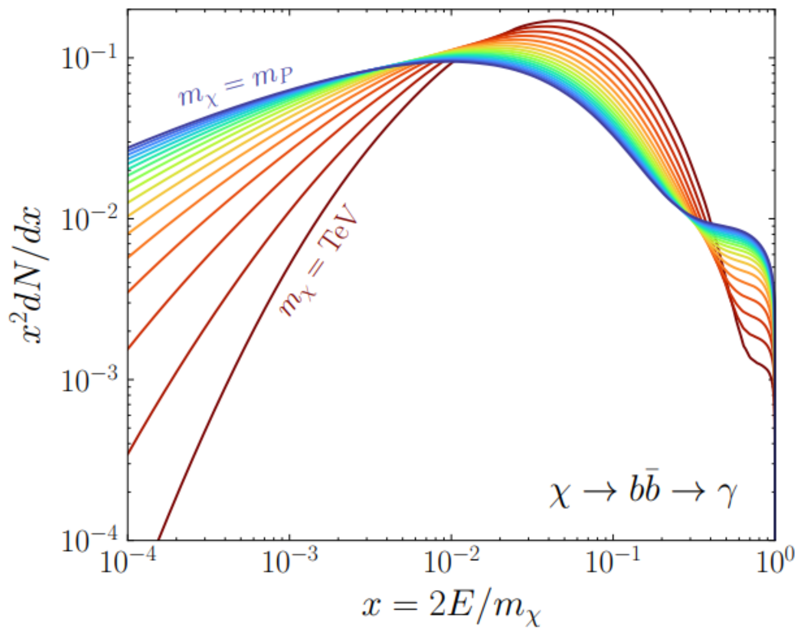

Figure 2.11 Dark Matter (DM) decay spectrum for $b\bar{b}$ initial state and γ final state. Redder spectra are for larger DM masses. Bluer spectra are light DM masses. x is a unitless factor defined as the ratio of the mass of DM, m_χ, and the final state particle energy E_γ. Figure from [19].

discovered, and it is the largest nearby DM dense region to look at. Additionally, the DM halo surrounding the Milky Way is clumpy [18]. There are regions in the DM halo of the Milky Way that have more DM than others that have captured gas over time. These sub-halos were dense enough collapse gas and form stars. These apparent sub galaxies are known as dwarf spheroidal galaxies and are the main sources studied in this thesis. Each source type comes with different trade-offs. Galactic Center studies will be very sensitive to the assumed distribution of DM. The central DM density can vary substantially as demonstrated in Figure 2.12. At distances close to the center of the galaxy, or small r, the differences in DM densities can be 3-4 orders of magnitude. Searches toward the galactic center will therefore be quite sensitive to the assumed DM distribution.

Searches toward Dwarf Spheroidal Galaxies (dSph's) suffer from uncertainties in the DM density less than the galactic center studies. This is mostly from their diminutive size being smaller than the angular resolution of most γ-ray observatories [18]. The DM content dSph's are typically determined with the Virial theorem, Equation (2.1), and are usually majority DM [18] in mass. DSph's tend to be ideal sources to look at for DM searches. Their environments are quiet with little

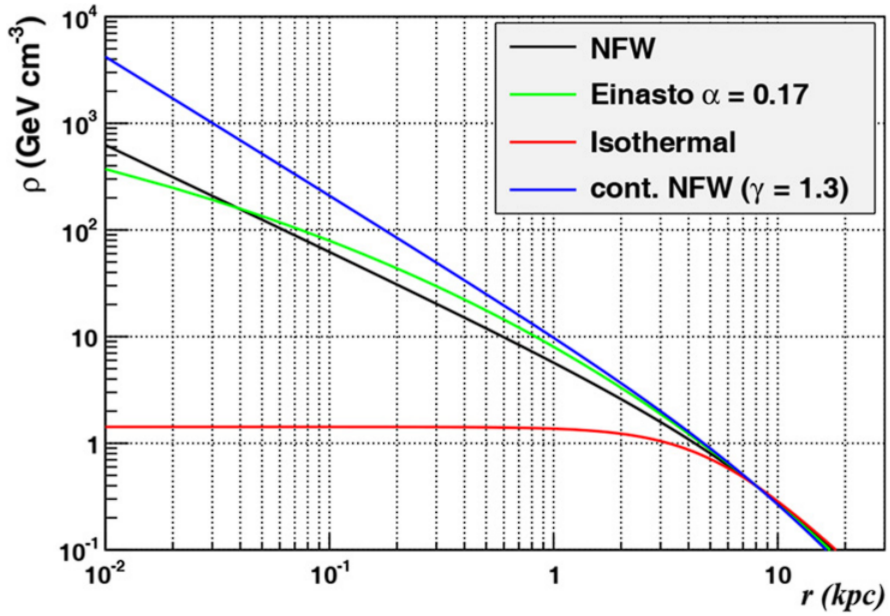

Figure 2.12 Different dark matter density profiles compared. Some models produce exceptionally large densities at small r [20].

astrophysical background. Unlike the galactic center, the most active components of dSph's are the stars within them versus a violent accretion disc around a black hole. All this together means that dSph's are among the best sources to look at for indirect DM searches. dSph's are the targets of focus for this thesis.

2.6 Multi-Messenger Dark Matter

Astrophysics entered a new phase in the past few decades that leverages our increasing sensitivity to SM channels and general relativity (GR). Up until the 21st century, astrophysical observations were performed with photons (γ) only. Astrophysics with this 'messenger' is fairly mature now. Novel observations of the universe have since only adjusted the sensitivity of the wavelength of light that is observed except at MeV energies. Gems like the CMB [10], and more have ultimately been observations of different wavelengths of light. Multi-messenger astrophysics proposes using other SM particles such the $p^{+/-}$, or ν or gravitation waves predicted by general relativity.

The experiment LIGO had a revolutionary discovery in 2016 with the first detection of a binary black hole merger [21]. This opened the collective imagination to observing the universe through gravitational waves. There has also been a surge of interest in the neutrino (ν) sector. IceCube demonstrated that we are sensitive to neutrinos in regions that correlate with significant photon emission like the galactic plane [22]. Neutrinos, like gravitational waves and light, travel mostly unimpeded from their source to our observatories. This makes pointing to the originating source of these messengers much easier than it is for cosmic rays which are deflected from their source by magnetic fields.

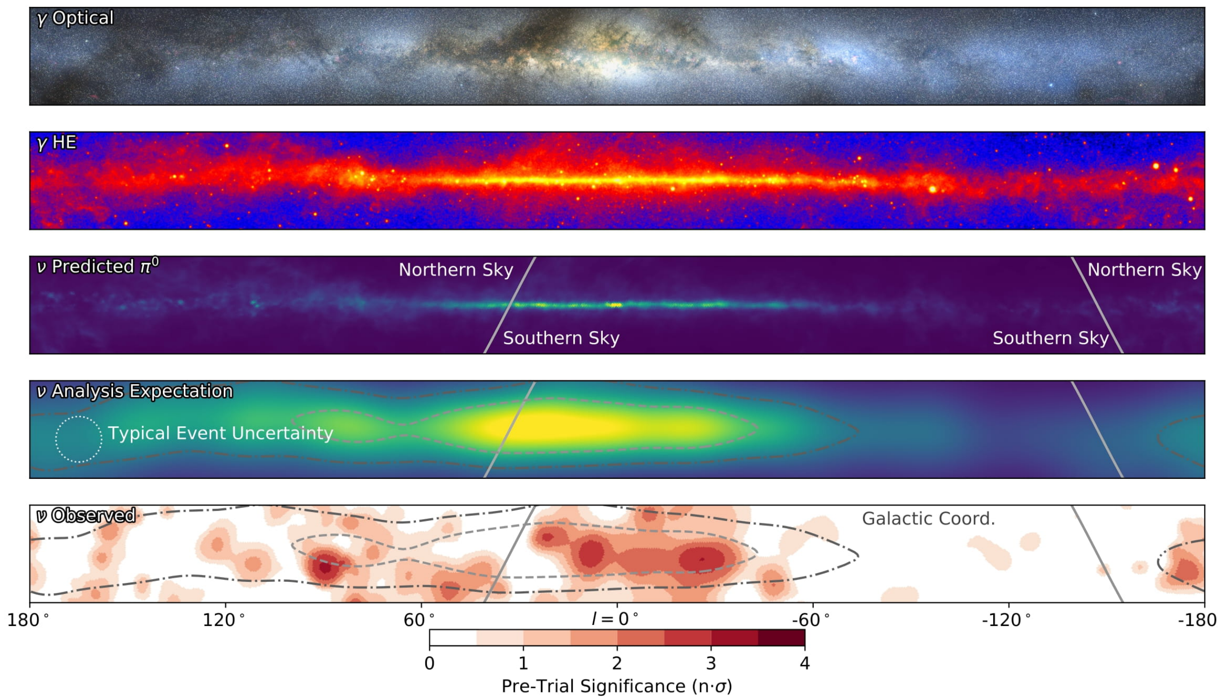

Figure 2.13 The Milky Way Galaxy in photons (γ) and neutrinos (ν) [22]. The Galactic center is at l=0°and is the brightest region in all panels. (top) An Optical color image of the Milky Way galaxy seen from Earth. Clouds of gas and dust obscure some light from stars. (2nd down) Integrated flux of γ-rays observed by the Fermi-LAT telescope [23]. (middle) Expected neutrino emission that corresponds with Fermi-LAT observations. (2nd up) Expected neutrino emission profile after considering detector systematics of IceCube. (bottom) Observed neutrino emission from region of the galactic plane. Substantial neutrino emission was detected.

The IceCube collaboration recently published a groundbreaking result of the Milky Way in neutrinos. The recent result from IceCube, shown in Figure 2.13, proves that we can make observations under different messenger regimes. The top two panels show the appearance of the galactic plane to different wavelengths of light. Some sources are more apparent in some panels, while others are not. This new channel is powerful because neutrinos are readily able to penetrate through gas and dust in the Milky Way. This new image also refines our understanding of how high energy particles are produced. For example, the fit to IceCube data prefers neutrino production from the decay of π^0 [22].

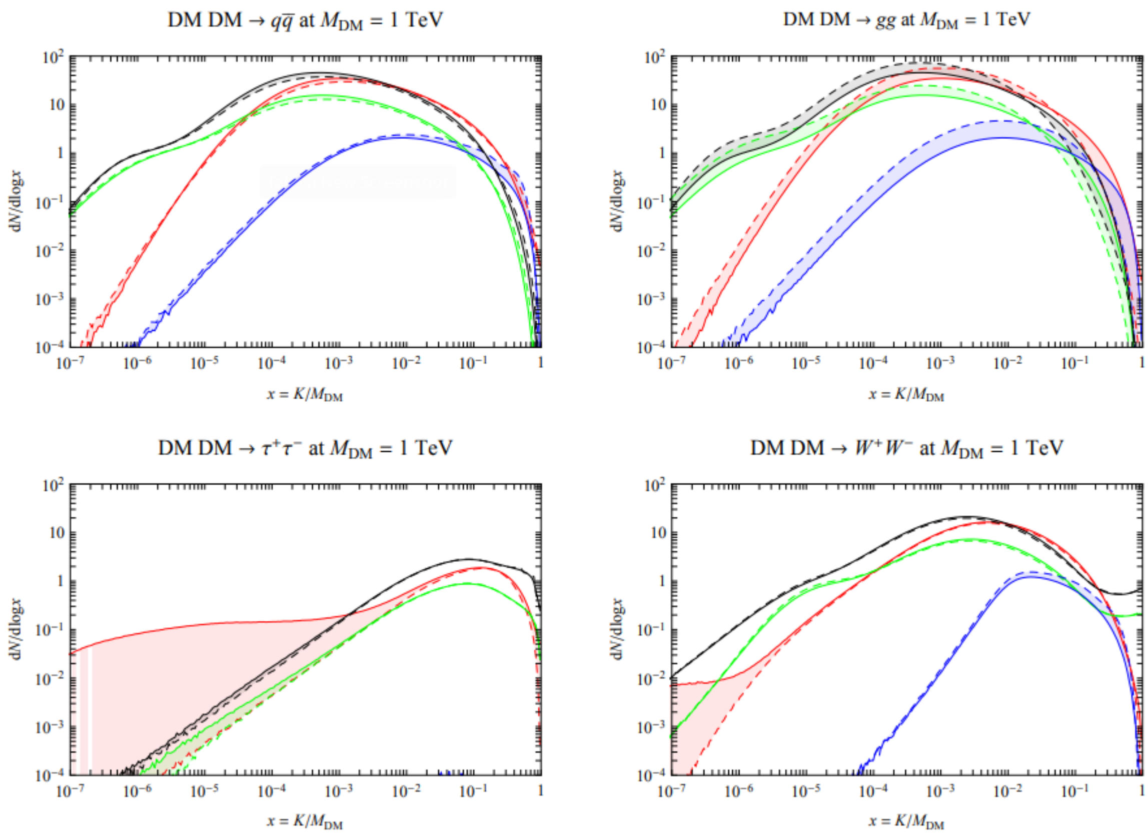

Figure 2.14 Dark Matter annihilation spectra for different final state particle and standard model annihilation channels [24]. Photons (red), $e^{\pm}$ (green), $\bar{p}$ (blue), ν (black).

Exposing our observations to more cosmic messengers greatly increases our sensitivity to rare processes. In the case of DM, Figure 2.14, there are many SM particles produced in DM annihilation. Among the final state fluxes are gammas and neutrinos. Charged particles are also produced however they would not likely make it to Earth since they will be deflected by magnetic fields between the source and Earth. This means observatories that can see the neutral messengers are especially good for DM searches and for combining data for a multi-messenger DM search.

CHAPTER 3

MULTIMESSENGER ASTROPHYSICS: DETECTING HIGH ENERGY NEUTRAL MESSENGERS

3.1 Introduction

Before the 20th century, all asttrophysics observations were optical in nature. We litterally only saw things with highly magnifiied optical observations. Then we discovered cosmic rays. cosmic rays are charged particles, typically naked protons or H+. This was seen by Victor Hess in 19??. Around the same time we discovered neutrinos from beta decay. Sometime around 1950 we started to build neutrino detectors which were mostly sensitive to neutrinos from the sun. Finally, it was theorized that compact objects like black holes and neutron stars would create waves in space-time when they experience mergers or collisions.

In the 21st century, we have developed new observation techniques and detectors that are no only sensitive to these four messengers - photons (TODO: photon), neutrinos (TODO: nu), Cosmic Rays (CR), and Gravitational Wave (WV) - we're collect high energy versions of these events. For the standad model particles, we're now sensitive to all messengers above the MeV eneryg range. Additionally, the GW's were sensitive to are in the stellar mass black hole region and above within our galactic neighborhood. This means were becoming sensitive to the fundamental physics occuring within the universe and we can rely on the universe as a TeV+ particle accelerator. We also have the abaility to correlate high energy events across messengers and gain new insights on the processes that occur in our universe.

This thesis focuses on very high energy (VHE) gamma rays and neutrinos. These can both be observed through the water cherenkov detection technique altho not exclusively. Methods on how to detect and observe these neutral messengers are discussed Section 3.3 and Section 3.4

3.2 Charged Particles in a Medium

For high enery gamma-rays and neutrinos, we can exploit the same effect that charged particles have with water. This effect is known as Cherenkov radiation. Cherenkov Radiation occurs when a charged particle, usually electrons (e) or muons (μ), traverse a medium, like water, faster than the speed of light in that medium. This is similar to sonic boom where an object moves through air faster than the speed of sound in air. Cherenkov radiation can therefor be thought of as an 'optic boom'. Many astro-particle physics experiments will use water as the medium as because water has a unique set of properties ideal for charged particle tracking.

Figure 3.1 TODO: Show a nuclear reactor with cherenkov radiation[NEEDS A SOURCE][FACT CHECK THIS]

The frequency of light emmited due to cherenkov radiation follows the equation:

$$INSERTCherenkovwavelengthcalcHERE. \tag{3.1}$$

The absorption spectra is shown in the following figure:

3.3 Photons (γ)

3.4 Neutrinos (ν)

3.5 Opportunities to Combine for Dark Matter

Figure 3.2 TODO: absorption spectrum of liquid and solid water[NEEDS A SOURCE][FACT CHECK THIS]

CHAPTER 4

HIGH ALTITUDE WATER CHERENKOV (HAWC) OBSERVATORY

4.1 The Detector

4.2 Events Reconstruction and Data Acquisition

4.2.1 G/H Discrimination

4.2.2 Angle

4.2.3 Energy

4.3 Remote Monitoring

4.3.1 ATHENA Database

4.3.2 HOMER

CHAPTER 5

ICECUBE NEUTRINO OBSERVATORY

5.1 The Detector

5.2 Events Reconstruction and Data Acquisition

5.2.1 Angle

5.2.2 Energy

5.3 Northern Test Site

5.3.1 PIgeon remote dark rate testing

5.3.2 Bulkhead Construction

CHAPTER 6

GLORY DUCK: MULTI-WAVELENGTH SEARCH FOR DARK MATTTER ANNIHILATION TOWARDS DWARF SPHEROIDAL GALAXIES

6.1 Introduction

The field of astrophysics now has several instruments and observatories sensitive to high energy gamma-rays. The energy sensitivity for the modern gamma-ray program spans many orders of magnitude. Figure 6.1 demonstrates these similar sensitivities across energies for the five experiments: Fermi-LAT, HAWC, HESS, MAGIC, and VERITAS.

Each of the five experiments featured in Figure 6.1 have independently searched for DM annihilation from dwarf spheroidal galaxies (dSph) and set limits. Intriguingly, there are regions of substantial overlap in their energy sensitivities. This clearly motivates an analysis that combines data from these five. Each experiment has unique gamma-ray detection methods and their weaknesses and strengths can be leveraged with each other. The HAWC gamma-ray observatory is extensively introduced in chapter 4, so it is not introduced here. A brief description of the remaining experiments are in the following paragraphs.

The Large Area Telescope (LAT) is a pair conversion telescope mounted on the NASA Fermi satellite in orbit ~550 km above the Earth [26]. LAT's field of view covers about 20% of the whole sky, and it sweeps the whole sky approximately every 3 hours. LAT's gamma-ray energy sensitivity ranges from 20 MeV up to 1 TeV. Previous DM searches towards dSphs using Fermi-LAT are published in [27] and [28]

The High Energy Spectroscopic System (HESS), Major Atmospheric Gamma Imaging Cherenkov (MAGIC), and Very Energetic Radiation Imaging Telescope Array System (VERITAS) are arrays of Imaging Atmospheric Cherenkov Telescopes (IACT). These telescopes observe the Cherenkov light emitted from gamma-ray showers in the Earth's atmosphere. The field of view for these telescopes is no larger than 5° with energy sensitivities ranging from 30 GeV up to 100 TeV [29, 30, 31]. IACTs are able to make precise observations in selected regions of the sky, however can only be operated in ideal dark conditions. HESS's observations of the dwarves

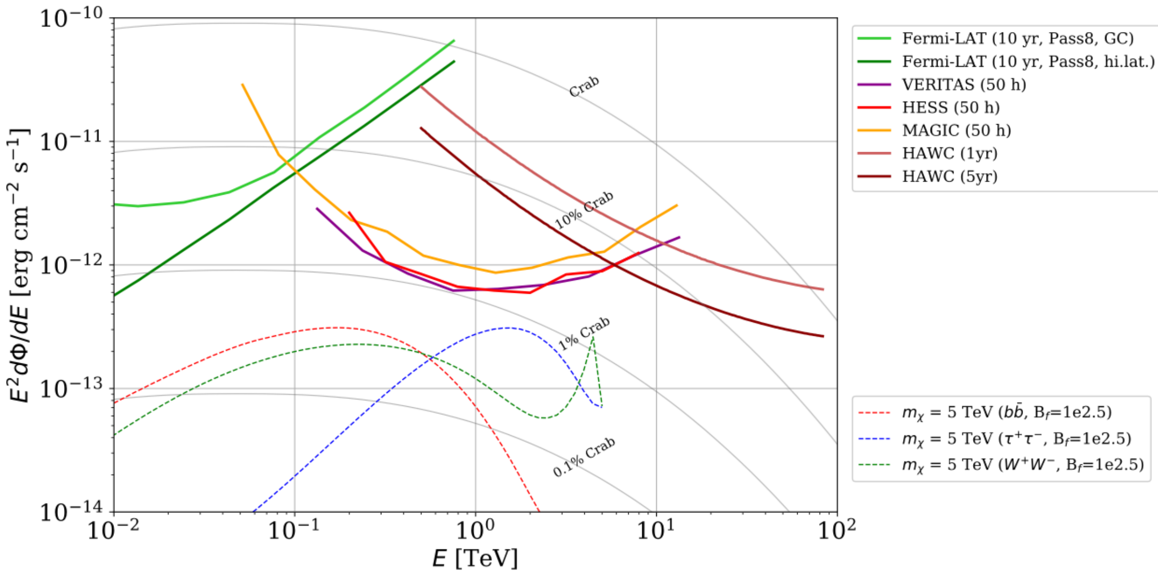

Figure 6.1 Sensitivities of five gamma-ray experiments compared to percentages of the Crab nebula's emission and dark matter annihilation. Solid lines present estimated sensitivities to power law spectra [FACT CHECK THIS]for each experiment. Green lines are Fermi-LAT sensitivities where lighter green is the sensitivity to the galactic center and dark green is its sensitivity to higher declinations. Orange, red, and purple solid lines represent the MAGIC, HESS, and VERITAS 50 hour sensitivities respectively. The maroon and brown lines are the HAWC 1 year and 5 year sensitivities. Across four decades of gamma-ray energy, these experiments have similar sensitivities on the order 10^{-12} erg cm^{-2}s^{-1}. The dotted lines are estimated dark matter fluxes assuming m_χ = 5 TeV DM annihilating to bottom quarks (red), tau leptons (blue), and W bosons (green). Faded gray lines outline percentage flux of the Crab nebula. Figure is an augmented version of [25]

Sculptor and Carina were between January 2008 and December 2009. HESS's observations of Coma Berenices were from 2010 to 2013, and Fornax was observed in 2010 [32, 33, 34]. MAGIC provided deep observations of Segue1 between 2011 and 2013 [35]. MAGIC also provides data for three dwarves: Coma Berenices, Draco, and Ursa Major II where observations were made in: January - June 2019 [36], March - September 2018 [36], and 2014 - 2016 [37] respectively. VERITAS provided data for Boötes I, Draco, Segue 1, and Ursa Minor from 2009 to 2016 [38].

This chapter presents the Glory Duck analysis, the name given for the search for dark matter annihilation from dSph by combining data from the five gamma-ray observatories: Fermi-LAT, HAWC, HESS, MAGIC, and VERITAS. Specifically, the methods in analysis and modeling are presented for the HAWC gamma-ray observatory. This work was published to the Journal of Cosmology and Astroparticle Physics and presented at the International Cosmic Ray Conference in 2019, 2021, and 2023 [39, 40, 41] and others.

6.2 Dataset and Background

This section enumerates the data and background methods used for HAWC's study of dSphs. Section 6.2.1 and Section 6.2.2 are most useful for fellow HAWC collaborators looking to replicate the Glory Duck analysis.

6.2.1 Itemized HAWC files

- Detector Resolution: `response_aerie_svn_27754_systematics_best_mc_test_nobroadpulse\_10pctlogchargesmearing_0.63qe_25kHzNoise_run5481_curvature0_index3.root`
- Data Map: `maps-20180119/liff/maptree_1024.root`
- Spectral Dictionary: `DM_CirrelliSpectrum_dict_gammas.npy`
- Analysis wiki: `https://private.hawc-observatory.org/wiki/index.php/Glory_Duck_Multi-Experiment_Dark_Matter_Search`

6.2.2 Software Tools and Development

This analysis was performed using HAL and 3ML [42, 43] in Python version 2. I built software to implement the *A Poor Particle Physicist Cookbook for Dark Matter Indirect Detection* (PPPC) [44] DM spectral model and dSphs spatial model from [45] for HAWC analysis. A NumPy version of this dictionary was made for both Py2 and Py3. The code base for creating this dictionary is linked on my GitLab sandbox:

- Py2: Dictionary Generator (Deprecated)
- Py3: PPPC2Dict

The analysis was performed using the f_{hit} framework performed in the HAWC Crab paper [42]. The Python2 NumPy dictionary file for gamma-ray final states is `dmCirSpecDict.npy`. The corresponding Python3 file is `DM_CirrelliSpectrum_dict_gammas.npy`. These files can also be used for decay channels and the PPPC describes how [44]. All other software used for data analysis, DM profile generation, and job submission to SLURM are also kept in my sandbox for the Glory Duck project.

6.2.3 Data Set and Background Description

The HAWC data maps used for this analysis contain 1017 days of data between runs 2104 (2014-11-26) and 7476 (2017-12-20). They were generated from pass 4.0 reconstruction. The analysis is performed using the f_{hit} energy binning scheme with bins (1-9) similar to what was done for the Crab and previous HAWC dSph analysis [42, 46]. Bin 0 was excluded as it has substantial hadronic contamination and poor angular resolution.

This analysis was done on dSphs because of their large DM mass content relative to baryonic mass. We consider the following to estimate the background to this study.

- The dSphs are small in HAWC's field of view, so the analysis is not sensitive to large or small scale anisotropies.
- The dSphs used in this analysis are off the galactic plane.
- The dSphs are baryonically faint relative to their expected dark matter content and are not expected to contain high energy gamma-ray sources.

Therefor we make no additional assumptions on the background from our sources and use HAWC's standard direct integration method for background estimation [42]. It is possible for gamma rays from DM annihilation to scatter in transit to HAWC via Inverse Compton Scattering (ICS). This was investigated and its impact on the flux is basically zero. Supporting information on this is in Section 6.7.1

6.3 Analysis

The expected differential photon flux from DM-DM annihilation to standard model particles, $d\Phi_\gamma/dE_\gamma$, over solid angle, Ω is described by the familiar equation.

$$\frac{d\Phi_\gamma}{dE_\gamma} = \frac{\langle\sigma v\rangle}{8\pi m_\chi^2}\frac{dN_\gamma}{dE_\gamma} \times \int_{\text{source}} d\Omega \int_{l.o.s} \rho_\chi^2 dl(r, \theta') \tag{6.1}$$

Where $\langle \sigma v \rangle$ is the velocity weighted annihilation cross-section. $\frac{dN}{dE}$ is the expected differential number of photons produced at each energy per annihilation. m_χ is the rest mass of the supposed DM particle. ρ_χ is the DM density. J is the astrophysical J-factor and is defined as

$$J = \int d\Omega \int_{l.o.s} dl \rho_\chi^2(r, \theta') \tag{6.2}$$

l is the distance to the source from Earth. r is the radial distance from the center of the source. θ' is the half angle defining a cone containing the DM source. How each component is synthesized and considered for HAWC's analysis is presented in the following sections. Section 6.3.1 presents the particle physics model for DM annihilation. Section 6.3.2 presents the spatial distributions built for each dSph.

6.3.1 $\frac{dN_\gamma}{dE_\gamma}$ - Particle Physics Component

For these spectra, we import the PPPC with Electroweak (EW) corrections [44]. The spectrum is implemented as a model script in astromodels for 3ML. The EW corrections were previously not considered for HAWC and are significant for DM annihilating to EW coupled SM particles such as all leptons, and the γ, Z, and W bosons [46]. Figure 6.2 demonstrates the significance of EW corrections for W boson annihilation. Across EW SM channels, the gamma-ray spectra become harder than spectra without EW corrections. Tables from the PPPC were reformatted into Python NumPy dictionaries for collaboration-wide use. A class in astromodels was developed to include the EW correction from the PPPC and is aptly named `PPPCSpectra` within `DM_models.py`.

6.3.2 J- Astrophysical Component

The J-factor profiles for each source are imported from Geringer-Sameth (referred to with $\mathcal{GS}$) [45]. These were pulled from the publication as $J(\theta)$, where θ is the angular separation from the center of the source. HAWC requires maps in terms of $\frac{dJ}{d\Omega}$, so the conversion from the maps was done in the following way...

First, convert the angular distances to solid angles

$$\Omega = 2 \cdot \pi (1 - \cos(\theta)) \tag{6.3}$$

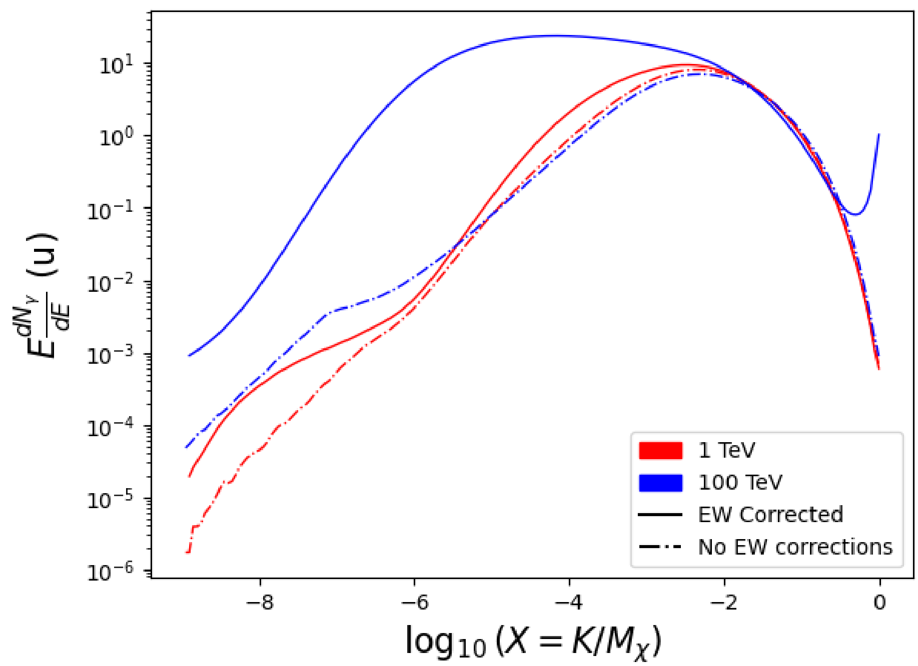

Figure 6.2 Effect of Electroweak (EW) corrections on expected DM annihilation spectrum for $\chi\chi \rightarrow W^-W^+$. Solid lines are spectral models that consider EW corrections. Dash-dot lines are spectral models without EW corrections. Red lines are models for $M_\chi = 1$ TeV. Blue lines represent models for $M_\chi = 100$ TeV. All models are sourced from the PPPC4DMID [44].

which reduces with a small angle approximation to $\pi\theta^2$. Next, the central difference for both the ΔJ and $\Delta\Omega$ value were calculated from the discretized $J(\theta)$ with the central difference stencil:

$$\Delta\phi_i = \phi_{i+1} - \phi_{i-1} \tag{6.4}$$

Where ϕ is either Ω or J. These were done separately in case the grid spacing in θ was not uniform. Finally, these lists are divided so that we are left with an approximation of the $dJ/d\Omega$ profile that is a function of θ. Admittedly, this is an approximation method for the map which introduces small errors compared to the true profile estimate. This was checked as a systematic against the author's profiling of the spatial distribution and is documented in Section 6.8.1.

With $\frac{dJ}{d\Omega}(\theta)$, a map is generated, first by filling in the north-east quadrant of the map. This quadrant is then reflected twice, vertically then horizontally, to fill the full map. Maps are then normalized by dividing the discrete 2D integral of the map. The 2D integral was a simple height of bins, Newton's integral:

$$p^2 \cdot \sum_{i,j=0}^{N,M} \frac{dJ}{d\Omega}(\theta_{i,j}, \phi_{i,j}) \tag{6.5}$$

These maps are HEALpix maps with NSIDE 16384 and saved in the `.fits` format.

Another DM spatial distribution model from Bonnivard ($\mathcal{B}$) [47] was used for the Glory Duck study. However, to save computational time, limits from $\mathcal{GS}$ were scaled to $\mathcal{B}$ instead of each experiment performing a full study a second time. How these models compare is demonstrated for each dSph in Figure 6.16 and Figure 6.17 Plots of these maps are provided for each source in chapter A Examples of the two most impactful dSphs derived from $\mathcal{GS}$, Segue1 and Coma Berenices are featured in Figure 6.3

6.3.3 Source Selection and Annihilation Channels

We use many of the dSphs presented in HAWC's previous dSph DM search [46]. HAWC's sources for Glory Duck include Boötes I, Coma Berenices, Canes Venatici I + II, Draco, Hercules, Leo I, II, + IV, Segue 1, Sextans, and Ursa Major I + II. A full description of all sources used in Glory Duck is found in Table 6.1. Triangulum II was excluded from the Glory Duck analysis because of large uncertainties in its J factor. Ursa Minor was excluded from HAWC's contribution to the combination because the source extension model extended Ursa Minor beyond HAWC's field of view. Ursa Minor was not expected to contribute significantly to the combined limit, so work was not invested in a solution to include Ursa Minor.

This analysis improves on the previous HAWC dSph paper [46] in the following ways. Previously, the dSphs were treated and implemented as point sources. For this analysis, dSphs are modeled and treated as extended source. The impact of this change with respect to the upper limit is source dependent and is explored in Section 6.7.2. Previously, the particle physics model used for gamma-ray spectra from DM annihilation did not have EW corrections where the PPPC includes them. Finally, the gamma-ray ray dataset is much larger. The study performed here analyzes over 1000 days of data compared to 507.

The SM annihilation channels probed for the Glory Duck combination include $b\bar{b}$, $e\bar{e}$, $\mu\bar{\mu}$, $\tau\bar{\tau}$, $t\bar{t}$, $W^{+}W^{-}$, and ZZ. A summary of all sources, with a description of each experiments' sensitivity

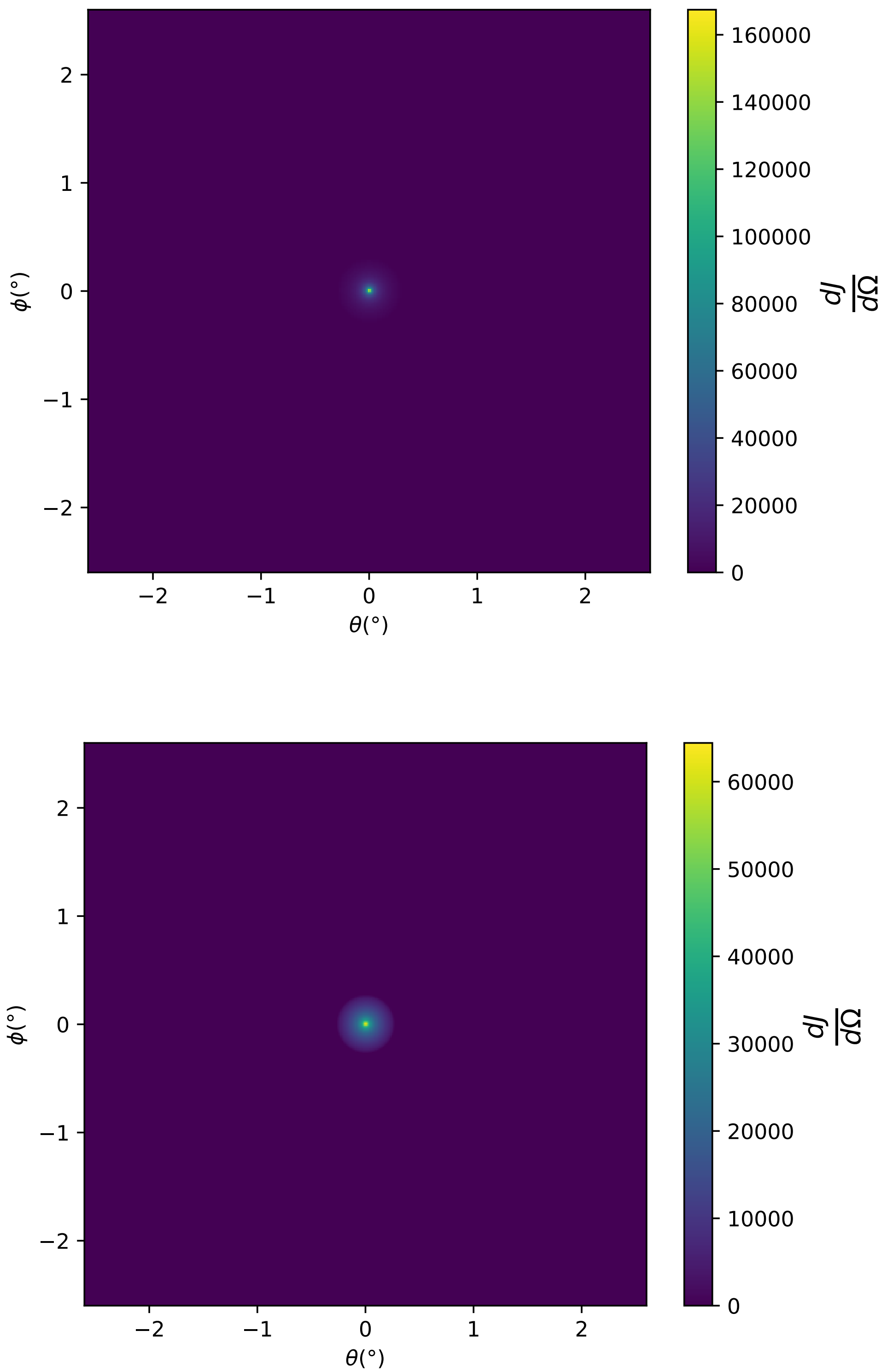

Figure 6.3 $\frac{dJ}{d\Omega}$ maps for Segue1 (top) and Coma Berenices (bottom). Origin is centered on the specific dwarf spheroidal galaxies (dSph). X and Y axes are the angular separation from the center of the dwarf. Plots of the remaining 11 dSph HAWC studied are linked in Fig. A.1.

Table 6.1 Summary of the relevant properties of the dSphs used in the present work. Column 1 lists the dSphs. Columns 2 and 3 present their heliocentric distance and galactic coordinates, respectively. Columns 4 and 5 report the J-factors of each source given from the $\mathcal{GS}$ and $\mathcal{B}$ independent studies and their estimated $\pm 1\sigma$ uncertainties. The values $\log_{10} J$ ($\mathcal{GS}$ set) [45] correspond to the mean J-factor values for a source extension truncated at the outermost observed star. The values $\log_{10} J$ ($\mathcal{B}$ set) [47] are provided for a source extension at the tidal radius of each dSph. **Bolded sources are within HAWC's field of view and provided to the Glory Duck analysis.**

Name	Distance (kpc)	l, b (°)	$\log_{10} J$ ($\mathcal{GS}$ set) $\log_{10}(\mathrm{GeV^2 cm^{-5} sr})$	$\log_{10} J$ ($\mathcal{B}$ set) $\log_{10}(\mathrm{GeV^2 cm^{-5} sr})$
Boötes I	66	358.08, 69.62	$18.24^{+0.40}_{-0.37}$	$18.85^{+1.10}_{-0.61}$
Canes Venatici I	218	74.31, 79.82	$17.44^{+0.37}_{-0.28}$	$17.63^{+0.50}_{-0.20}$
Canes Venatici II	160	113.58, 82.70	$17.65^{+0.45}_{-0.43}$	$18.67^{+1.54}_{-0.97}$
Carina	105	260.11, −22.22	$17.92^{+0.19}_{-0.11}$	$18.02^{+0.36}_{-0.15}$
Coma Berenices	44	241.89, 83.61	$19.02^{+0.37}_{-0.41}$	$20.13^{+1.56}_{-1.08}$
Draco	76	86.37, 34.72	$19.05^{+0.22}_{-0.21}$	$19.42^{+0.92}_{-0.47}$
Fornax	147	237.10, −65.65	$17.84^{+0.11}_{-0.06}$	$17.85^{+0.11}_{-0.08}$
Hercules	132	28.73, 36.87	$16.86^{+0.74}_{-0.68}$	$17.70^{+1.08}_{-0.73}$
Leo I	254	225.99, 49.11	$17.84^{+0.20}_{-0.16}$	$17.93^{+0.65}_{-0.25}$
Leo II	233	220.17, 67.23	$17.97^{+0.20}_{-0.18}$	$18.11^{+0.71}_{-0.25}$
Leo IV	154	265.44, 56.51	$16.32^{+1.06}_{-1.70}$	$16.36^{+1.44}_{-1.65}$
Leo V	178	261.86, 58.54	$16.37^{+0.94}_{-0.87}$	$16.30^{+1.33}_{-1.16}$
Leo T	417	214.85, 43.66	$17.11^{+0.44}_{-0.39}$	$17.67^{+1.01}_{-0.56}$
Sculptor	86	287.53, −83.16	$18.57^{+0.07}_{-0.05}$	$18.63^{+0.14}_{-0.08}$
Segue I	23	220.48, 50.43	$19.36^{+0.32}_{-0.35}$	$17.52^{+2.54}_{-2.65}$
Segue II	35	149.43, −38.14	$16.21^{+1.06}_{-0.98}$	$19.50^{+1.82}_{-1.48}$
Sextans	86	243.50, 42.27	$17.92^{+0.35}_{-0.29}$	$18.04^{+0.50}_{-0.28}$
Ursa Major I	97	159.43, 54.41	$17.87^{+0.56}_{-0.33}$	$18.84^{+0.97}_{-0.43}$
Ursa Major II	32	152.46, 37.44	$19.42^{+0.44}_{-0.42}$	$20.60^{+1.46}_{-0.95}$
Ursa Minor	76	104.97, 44.80	$18.95^{+0.26}_{-0.18}$	$19.08^{+0.21}_{-0.13}$

to the source, is provided in Table 6.2.

6.4 Likelihood Methods

6.4.1 HAWC Likelihoods

For every analysis bin in energy, f_{hit} bins (1-9), and location, we can expect N signal events and B background events. The expected number of excess signal events from dark matter annihilation,

Table 6.2 Summary of dSph observations by each experiment used in this work. A '-' indicates the experiment did not observe the dSph for this study. For Fermi-LAT, the exposure at 1 GeV is given. For HAWC, $|\Delta\theta|$ is the absolute difference between the source declination and HAWC latitude. HAWC is more sensitive to sources with smaller $|\Delta\theta|$. For IACTs, we show the zenith angle range, the total exposure, the energy range, the angular radius θ of the signal or ON region, the ratio of exposures between the background-control (OFF) and signal (ON) regions (τ), and the significance of gamma-ray excess in standard deviations, σ.

	Fermi-LAT	HAWC	H.E.S.S, MAGIC, VERITAS						
Source name	Exposure (10^{11} s m^2)	$\|\Delta\theta\|$ (°)	IACT	Zenith (°)	Exposure (h)	Energy range (GeV)	θ (°)	τ	S (σ)
Boötes I	2.6	4.5	VERITAS	15 – 30	14.0	100-41000	0.10	8.6	−1.0
Canes Venatici I	2.9	14.6	–	–	–	–	–	–	–
Canes Venatici II	2.9	15.3	–	–	–	–	–	–	–
Carina	3.1	–	H.E.S.S.	27 – 46	23.7	310 – 70000	0.10	18.0	−0.3
Coma Berenices	2.7	4.9	H.E.S.S.	47 – 49	11.4	550 – 70000	0.10	14.4	−0.4
			MAGIC	5 – 37	49.5	60 – 10000	0.17	1.0	–
Draco	3.8	38.1	MAGIC	29 – 45	52.1	70 – 10000	0.22	1.0	–
			VERITAS	25 – 40	49.8	120 – 70000	0.10	9.0	−1.0
Fornax	2.7	–	H.E.S.S.	11 – 25	6.8	230 – 70000	0.10	45.5	−1.5
Hercules	2.8	6.3	–	–	–	–	–	–	–
Leo I	2.5	6.7	–	–	–	–	–	–	–
Leo II	2.6	3.1	–	–	–	–	–	–	–
Leo IV	2.4	19.5	–	–	–	–	–	–	–
Leo V	2.4	–	–	–	–	–	–	–	–
Leo T	2.6	–	–	–	–	–	–	–	–
Sculptor	2.7	–	H.E.S.S.	10 – 46	11.8	200 – 70000	0.10	19.8	−2.2
Segue I	2.5	2.9	MAGIC	13 – 37	158.0	60 – 10000	0.12	1.0	−0.5
			VERITAS	15 – 35	92.0	80 – 50000	0.10	7.6	0.7
Segue II	2.7	–	–	–	–	–	–	–	–
Sextans	2.4	20.6	–	–	–	–	–	–	–
Ursa Major I	3.4	32.9	–	–	–	–	–	–	–
Ursa Major II	4.0	44.1	MAGIC	35 – 45	94.8	120 – 10000	0.30	1.0	−2.1
Ursa Minor	4.1	–	VERITAS	35 – 45	60.4	160 – 93000	0.10	8.4	−0.1

S, is estimated by convolving Equation (6.1) with HAWC's energy response and pixel point spread functions. I then compute the test statistic (TS) with the log-likelihood ratio test,

$$\mathrm{TS} = -2\ln\left(\frac{\mathcal{L}_0}{\mathcal{L}^{\max}}\right) \tag{6.6}$$

where $\mathcal{L}_0$ is the null hypothesis, or no DM emission, likelihood. $\mathcal{L}^{\max}$ is the best fit signal hypothesis where $\langle\sigma v\rangle$ maximizes the likelihood. We calculate the likelihood of each source and model, assuming events are Poisson distributed, with

$$\mathcal{L} = \prod_i \frac{(B_i + S_i)^{N_i} e^{-(B_i+S_i)}}{N_i!} \tag{6.7}$$

where S_i is the sum of expected number of signal counts. B_i is the number of background counts observed. N_i is the total number of counts.

I also calculate an upper limit on $\langle\sigma v\rangle$ by calculating the 95% confidence level (CL). For the CL, we define a parameter, TS_{95}, as

$$\mathrm{TS}_{95} \equiv \sum_{\mathrm{bins}} \left[2N\ln\left(1 + \frac{\epsilon S_{\mathrm{ref}}}{B}\right) - 2\epsilon S_{\mathrm{ref}}\right] \tag{6.8}$$

where the expected signal counts from a dSph is scaled by ϵ. S_{ref} is the expected number of excess counts in a bin from DM emission from a dSph with a corresponding annihilation cross-section, $\langle\sigma v\rangle$. We scan ϵ such that

$$2.71 = \mathrm{TS}_{\max} - \mathrm{TS}_{95} \tag{6.9}$$

6.4.2 Glory Duck Joint Likelihood

The joint likelihood for the 5-experiment combination was done similarly as Section 6.4.1. We calculate upper limits on $\langle\sigma v\rangle$ from the TS, Eq. (6.6), and define the likelihood ratio more generally

$$\lambda\left(\langle\sigma v\rangle \mid \mathcal{D}_{\mathrm{dSphs}}\right) = \frac{\mathcal{L}\left(\langle\sigma v\rangle; \hat{\hat{\boldsymbol{\nu}}} \mid \mathcal{D}_{\mathrm{dSphs}}\right)}{\mathcal{L}\left(\widehat{\langle\sigma v\rangle}; \hat{\boldsymbol{\nu}} \mid \mathcal{D}_{\mathrm{dSphs}}\right)} \tag{6.10}$$

$\boldsymbol{\mathcal{D}}_{\mathbf{dSphs}}$ is the totality of observations across experiments and dSphs. $\boldsymbol{\nu}$ are the nuisance parameters which are the J factors in this study. $\widehat{\langle\sigma v\rangle}$ and $\hat{\boldsymbol{\nu}}$ are the respective estimate that maximize $\mathcal{L}$ globally. Finally, $\hat{\hat{\boldsymbol{\nu}}}$ is the set of nuisance parameters that maximize $\mathcal{L}$ for a fixed value of $\langle\sigma v\rangle$.

The *complete* joint likelihood, $\mathcal{L}$ that encompasses all observations from all instruments and dSphs can be factorized into *partial* functions for each dSph l (with $\mathcal{L}_{\mathrm{dSph},l}$) and its J factor ($\mathcal{J}_l$):

$$\mathcal{L}\left(\langle\sigma v\rangle;\boldsymbol{\nu}\mid\boldsymbol{\mathcal{D}}_{\mathbf{dSphs}}\right)=\prod_{l=1}^{N_{\mathrm{dSphs}}}\mathcal{L}_{\mathrm{dSph},l}\left(\langle\sigma v\rangle;J_l,\boldsymbol{\nu_l}\mid\boldsymbol{\mathcal{D}_l}\right)\times\mathcal{J}_l\left(J_l\mid J_{l,\mathrm{obs}},\sigma_{\log J_l}\right). \tag{6.11}$$

For this study, $N_{\mathrm{dSphs}}=20$ is the number of dSphs studied. $\boldsymbol{\mathcal{D}_l}$ are the gamma-ray observations of dSph, l. $\boldsymbol{\nu_l}$ are the nuisance parameters modifying the gamma-ray observations of dSph, l, but excludes $\mathcal{J}_l$. $\mathcal{J}_l$ is the J factor for dSph, l, as defined in Equation (6.2), and it is a nuisance parameter whose value is unknown. $\log_{10}J_{l,\mathrm{obs}}$ and $\sigma_{\log J_l}$ are obtained from fitting a log-normal function of $J_{l,\mathrm{obs}}$ to the posterior distribution of J_l [48]. $\log_{10}J_{l,\mathrm{obs}}$ and $\sigma_{\log J_l}$ values are provided in Table 6.1. The term $\mathcal{J}_l$ constraining J_l is written as:

$$\mathcal{J}_l\left(J_l\mid J_{l,\mathrm{obs}},\sigma_{\log J_l}\right)=\frac{1}{\ln(10)J_{l,\mathrm{obs}}\sqrt{2\pi}\sigma_{\log J_l}}\exp\left(-\frac{\left(\log_{10}J_l-\log_{10}J_{l,\mathrm{obs}}\right)^2}{2\sigma^2_{\log J_l}}\right). \tag{6.12}$$

Both the $\mathcal{GS}$ and $\mathcal{B}$, displayed in Table 6.1, sets of J factors are used in this analysis. Equation (6.12) is also normalized, so it can also be interpreted as a probability density function (PDF) for $J_{l,\mathrm{obs}}$. From Equation (6.1), we can also see that $\langle\sigma v\rangle$ and J_l are degenerate when computing $\mathcal{L}_{\mathrm{dSph},l}$. Therefore, as noted in [49], it is sufficient to compute $\mathcal{L}_{\mathrm{dSph},l}$ versus $\langle\sigma v\rangle$ for a fixed value of J_l. We used $J_{l,\mathrm{obs}}(\mathcal{GS})$ reported in Tab. 6.1, in order to perform the profile of $\mathcal{L}$ with respect to J_l. The degeneracy implies that for any $J'_l\neq J_{l,\mathrm{obs}}$ (in practice in our case we used $J'_l=J_{l,\mathrm{obs}}(\mathcal{B})$ to compute results from a different set of J factors):

$$\mathcal{L}_{\mathrm{dSph},l}\left(\langle\sigma v\rangle;J'_l,\boldsymbol{\nu_l}\mid\boldsymbol{\mathcal{D}_l}\right)=\mathcal{L}_{\mathrm{dSph},l}\left(\frac{J'_l}{J_{l,\mathrm{obs}}}\langle\sigma v\rangle;J_{l,\mathrm{obs}},\boldsymbol{\nu_l}\mid\boldsymbol{\mathcal{D}_l}\right), \tag{6.13}$$

which is a straightforward rescaling operation that reduces the computational needs of the profiling operation since:

$$\mathcal{L}\left(\langle\sigma v\rangle;\hat{\boldsymbol{\nu}}\mid\boldsymbol{\mathcal{D}}_{\mathbf{dSphs}}\right)=\prod_{l=1}^{N_{\mathrm{dSphs}}}\max_{J_l}\left[\mathcal{L}_{\mathrm{dSph},l}\left(\langle\sigma v\rangle;J_l,\hat{\boldsymbol{\nu}}_{\boldsymbol{l}}\mid\boldsymbol{\mathcal{D}_l}\right)\times\mathcal{J}_l\left(J_l\mid J_{l,\mathrm{obs}},\sigma_{\log_{J_l}}\right)\right]. \tag{6.14}$$

In addition, Eq. (6.13) enables the combination of data from different gamma-ray instruments and observed dSphs via tabulated values of $\mathcal{L}_{\mathrm{dSph},l}$, or equivalently of λ from Eq. (6.10) as was done in

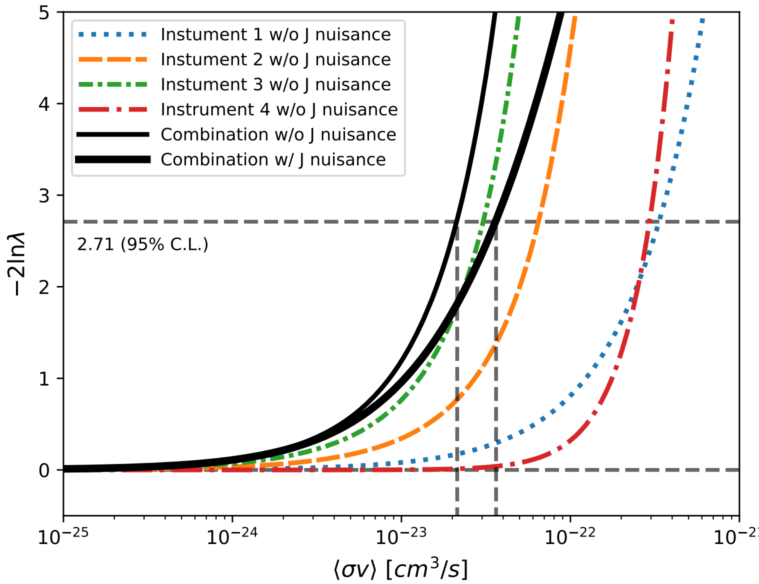

Figure 6.4 Illustration of the combination technique showing a comparison between $-2\ln\lambda$ provided by four instruments (colored lines) from the observation of the same dSph without any J nuisance and their sum, *i.e*. the resulting combined likelihood (thin black line). According to the test statistics of Equation (6.6), the intersection of the likelihood profiles with the line $-2\ln\lambda = 2.71$ indicates the 95% C.L. upper limit on $\langle\sigma v\rangle$. The combined likelihood (thin black line) shows a smaller value of upper limit on $\langle\sigma v\rangle$than those derived by individual instruments. We also show how the uncertainties on the J factor effects the combined likelihood and degrade the upper limit on $\langle\sigma v\rangle$(thick black line). All likelihood profiles are normalized so that the global minimum $\widehat{\langle\sigma v\rangle}$ is 0. We note that each profile depends on the observational conditions in which a target object was observed. The sensitivity of a given instrument can be degraded and the upper limits less constraining if the observations are performed in non-optimal conditions such as a high zenith angle or a short exposure time.

this work, versus $\langle\sigma v\rangle$. $\mathcal{L}_{\mathrm{dSph},l}$ is computed for a fixed value of J_l and profiled with respect to all instrumental nuisance parameters $\boldsymbol{\nu}_l$, these nuisance parameters are discussed in more detail below. These values are produced by each detector independently and therefore there is no need to share sensitive low-level information used to produce them, such as event lists. Figure 6.4 illustrates the multi-instrument combination technique used in this study with a comparison of the upper limit on $\langle\sigma v\rangle$ obtained from the combination of the observations of four experiments towards one dSph versus the upper limit from individual instruments. It also shows graphically the effect of the J-factor uncertainty on the combined observations.

The *partial* joint likelihood function for gamma-ray observations of each dSph ($\mathcal{L}_{\mathrm{dSph},l}$) is written as the product of the likelihood terms describing the $N_{\mathrm{exp},l}$ observations performed with any of our observatories:

$$\mathcal{L}_{\mathrm{dSph},l}\left(\langle\sigma v\rangle; J_l, \boldsymbol{\nu_l} \mid \boldsymbol{\mathcal{D}_l}\right) = \prod_{k=1}^{N_{\mathrm{exp},l}} \mathcal{L}_{lk}\left(\langle\sigma v\rangle; J_l, \boldsymbol{\nu_{lk}} \mid \boldsymbol{\mathcal{D}_{lk}}\right), \tag{6.15}$$

where each $\mathcal{L}_{lk}$ term refers to an observation of the l-th dSph with associated k-th instrument responses. $N_{\mathrm{exp},l}$ varies from dSph to dSph and can be inferred from Table 6.2.

Each collaboration separately analyzes their data for $\boldsymbol{\mathcal{D}_{lk}}$ corresponding to dSph l and gamma-ray detector k, using as many common assumptions as possible in the analysis. HAWC's treatment was described earlier in Section 6.4.1 whereas the specifics of the remaining experiments is left to the publication. We compute the values for the likelihood functions $\mathcal{L}_{lk}$ (see Eq. (6.15)) for a fixed value of J_l and profile over the rest of the nuisance parameters $\boldsymbol{\nu_{lk}}$. Then, values of λ from Eq. (6.10) are computed as a function of $\langle\sigma v\rangle$, and shared using a common format. Results are computed for seven annihilation channels, W^+W^-, ZZ, $b\bar{b}$, $t\bar{t}$, e^+e^-, $\mu^+\mu^-$, and $\tau^+\tau^-$ over 62 m_χ values between 5 GeV and 100 TeV provided in [44]. The $\langle\sigma v\rangle$range is defined between 10^{-28} and $10^{-18}\mathrm{cm}^3 \cdot \mathrm{s}^{-1}$, with 1001 logarithmically spaced values. The likelihood combination, i.e. Equation (6.11), and profile over the J-factor to compute the profile likelihood ratio λ, Equation (6.10), are carried out with two different public analysis software packages, namely `gLike` [50] and `LklCom` [51], that provide the same results [52].

As mentioned previously, each experiment computes the $\mathcal{L}_{lk}$ from Equation (6.10) differently. The remainder of this section highlights the differences in this calculation across the experiments. Four experiments, namely *Fermi*-LAT, H.E.S.S., HAWC and MAGIC, use a binned likelihood to compute the $\mathcal{L}_{lk}$. For these experiments, for each observation $\boldsymbol{\mathcal{D}_{lk}}$ of a given dSph l carried out using a given gamma-ray detector k, the binned likelihood function is:

$$\mathcal{L}_{lk}\left(\langle\sigma v\rangle; J_l, \boldsymbol{\nu_{lk}} \mid \boldsymbol{\mathcal{D}_{lk}}\right) = \prod_{i=1}^{N_{\mathrm{E}'}} \prod_{j=1}^{N_{\mathrm{P}'}} \left[\mathcal{P}\left(s_{lk,ij}(\langle\sigma v\rangle, J_l, \boldsymbol{\nu_{lk}}) + b_{lk,ij}(\boldsymbol{\nu_{lk}}) \mid N_{lk,ij}\right)\right] \times \mathcal{L}_{lk,\nu}\left(\boldsymbol{\nu_{lk}} \mid \boldsymbol{\mathcal{D}_{\nu_{lk}}}\right) \tag{6.16}$$

where $N_{\mathrm{E}'}$ and $N_{\mathrm{P}'}$ are the number of considered bins in reconstructed energy and arrival direction, respectively; $\mathcal{P}$ represents a Poisson PDF for the number of gamma-ray candidate events $N_{lk,ij}$

observed in the i-th bin in energy and j-th bin in arrival direction, when the expected number is the sum of the expected mean number of signal events s_{ij} (produced by DM annihilation) and of background events b_{ij}; $\mathcal{L}_{lk,\boldsymbol{\nu}}$ is the likelihood term for the extra $\boldsymbol{\nu_{lk}}$ nuisance parameters that vary from one instrument k to another. The expected counts for signal events s_{ij} for a given dSph l and detector k is given by:

$$s_{ij}(\langle\sigma v\rangle, J) = \int_{E'_{\mathrm{min},i}}^{E'_{\mathrm{max},i}} \mathrm{d}E' \int_{P'_{\mathrm{min},j}}^{P'_{\mathrm{max},j}} \mathrm{d}\Omega' \int_{0}^{\infty} \mathrm{d}E \int_{\Delta\Omega_{tot}} \mathrm{d}\Omega \int_{0}^{T_{\mathrm{obs}}} \mathrm{d}t \frac{\mathrm{d}^2\Phi(\langle\sigma v\rangle, J)}{\mathrm{d}E\mathrm{d}\Omega} \mathrm{IRF}\,(E', P' \mid E, P, t) \tag{6.17}$$

where E' and E are the reconstructed and true energies, P' and P the reconstructed and true arrival directions; $E'_{\mathrm{min},i}$, $P'_{\mathrm{min},j}$, $E'_{\mathrm{max},i}$, and $P'_{\mathrm{max},j}$ are their lower and upper limits of the i-th energy bin and the j-th arrival direction bin; T_{obs} is the (dead-time corrected) total observation time; t is the time along the observations; $\mathrm{d}^2\Phi/\mathrm{d}E\mathrm{d}\Omega$ is the DM flux in the source region (see Equation (6.1)); and $\mathrm{IRF}\,(E', P' \mid E, P, t)$ is the IRF, which can be factorized as the product of the effective collection area of the detector $A_{\mathrm{eff}}(E, P, t)$, the PDFs for the energy estimator $f_E(E' \mid E, t)$, and arrival direction $f_P(P' \mid E, P, t)$ estimators. Note that for Fermi-LAT, HAWC, MAGIC, and VERITAS the effect of the finite angular resolution is taken into account through the convolution of $d\Phi/dEd\Omega$ with f_P in Equation (6.17), whereas in the cases of H.E.S.S. f_P is approximated by a delta function. This approximation has been made in order to maintain compatibility of the result with what has been previously published. The difference introduced by this approximation is $< 5\%$ for all considered dSphs. A more comprehensive review of the differences between the analyses of different instruments can be found in [25].

6.5 HAWC Results

13 of the 20 dSphs considered for the Glory Duck analysis are within HAWC's field of view. These dSph are analyzed for emission from DM annihilation according to the likelihood method described in Section 6.4. The 13 likelihood profiles are then stacked to synthesize a combined limit on the dark matter cross-section, $\langle\sigma v\rangle$. This combination is done for the 7 SM annihilation channels used in the Glory Duck analysis. Figure 6.5 shows the combined limit for all annihilation channels with HAWC only observations. We also perform 300 studies of Poisson trials on the

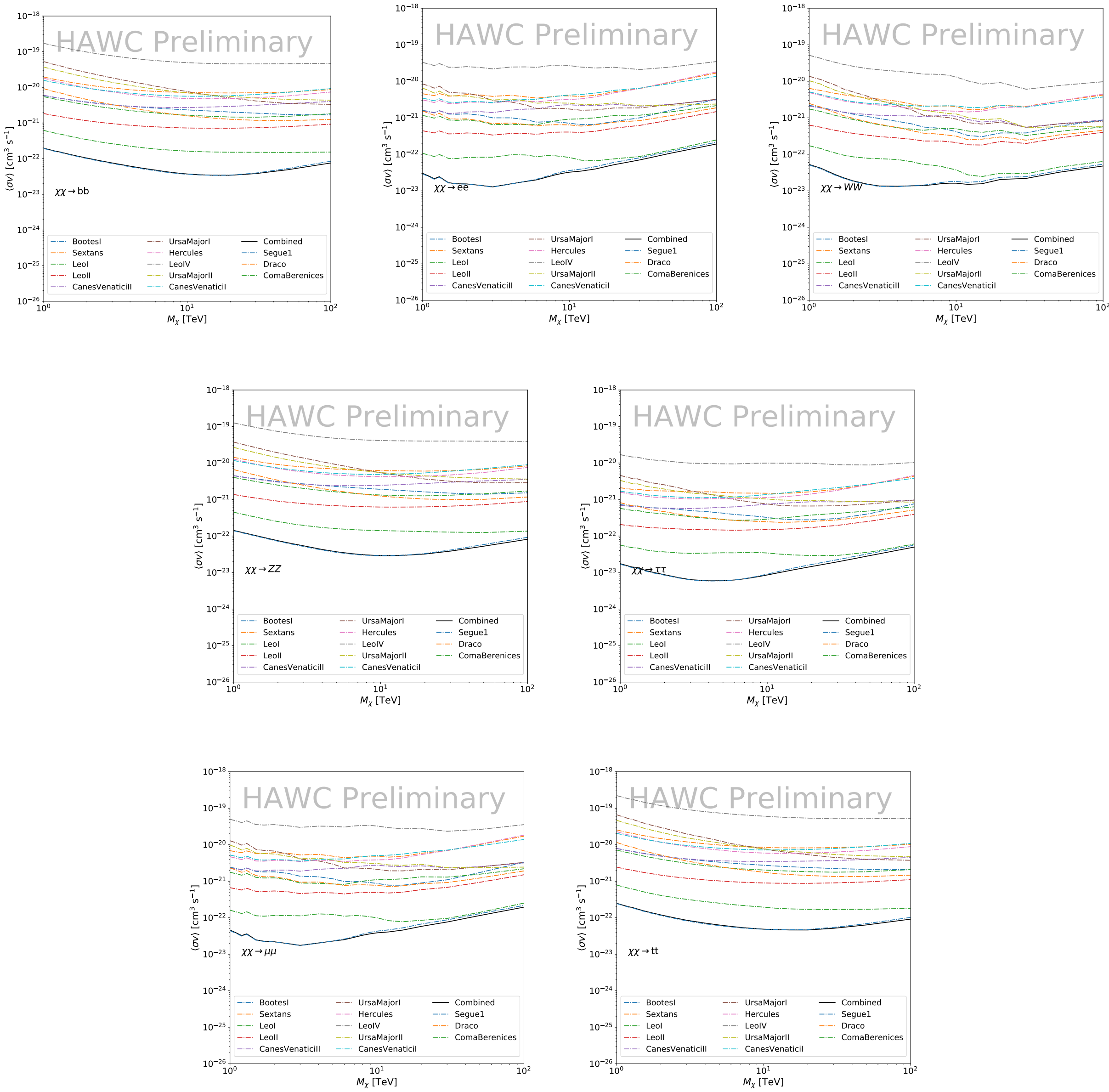

Figure 6.5 HAWC upper limits at 95% confidence level on $\langle\sigma v\rangle$versus DM mass for seven annihilation channels, using the set of J-factors from Ref. [53] The solid line represents the observed combined limit. Dashed lines represent limits from individual dSphs.

background. These trials are used to produce HAWC Brazil bands which were shared with the other collaborators for combined Brazil Bands. The results on fitting to HAWC's Poisson trials of the DM hypothesis is shown in Figure 6.7 for all the DM annihilation channels studied for Glory Duck.

No DM was found in HAWC observations. HAWC's limits are dominated by the dSphs Segue1

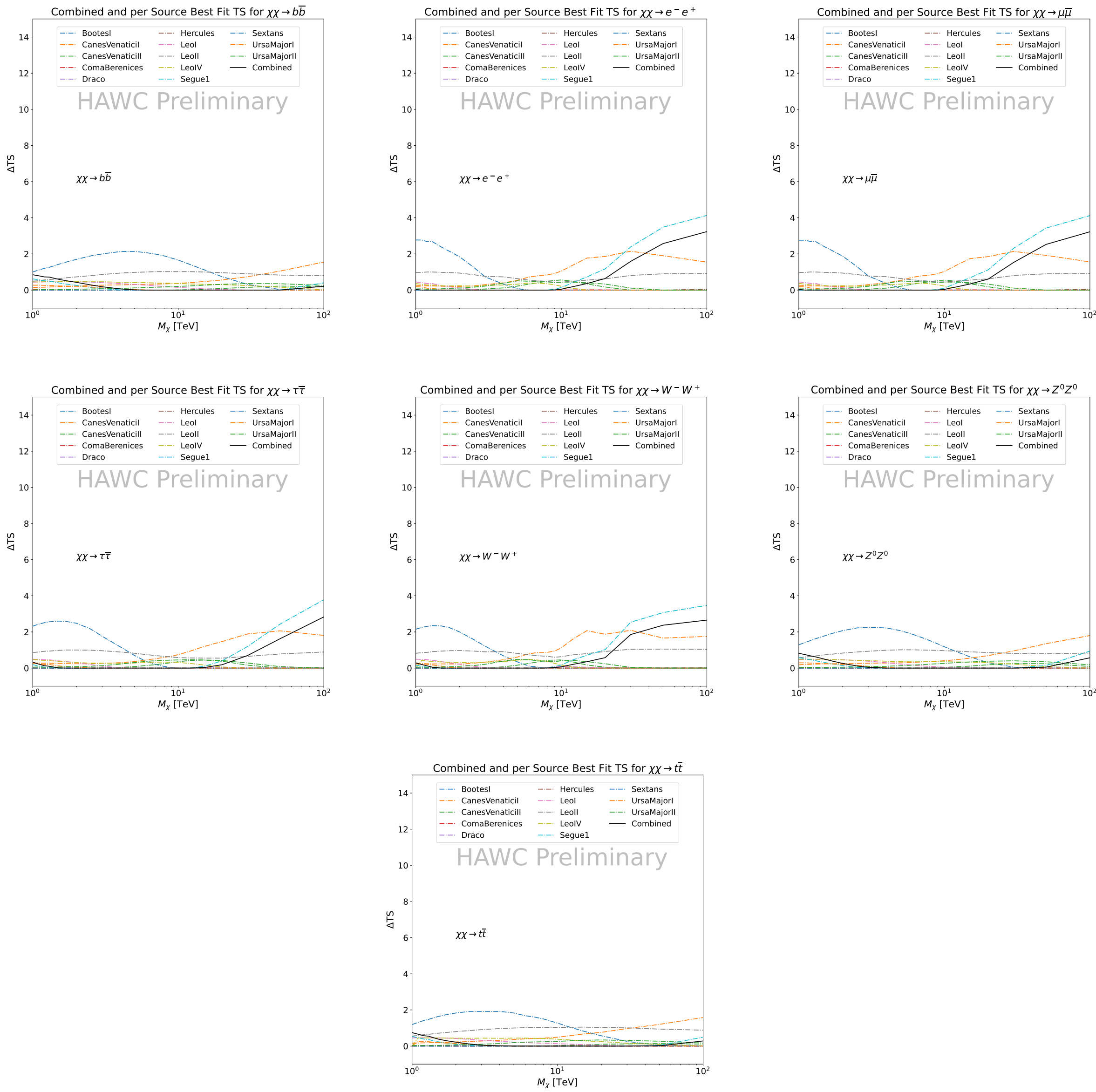

Figure 6.6 HAWC TS values for best fit $\langle \sigma v \rangle$ versus m_χ for seven SM annihilation channels with J factors from $\mathcal{GS}$. The solid black line shows the combined best fit TS values. The colored, dashed lines are the TS values for each of the 13 sources HAWC studied.

and Coma Berenices. The remaining 11 dSphs do not contribute significantly to the limit because they are at high zenith and/or have much smaller J factors. Even though some remaining dSphs have large J factors, they are towards the edge of HAWC's field of view where HAWC analysis is less sensitive.

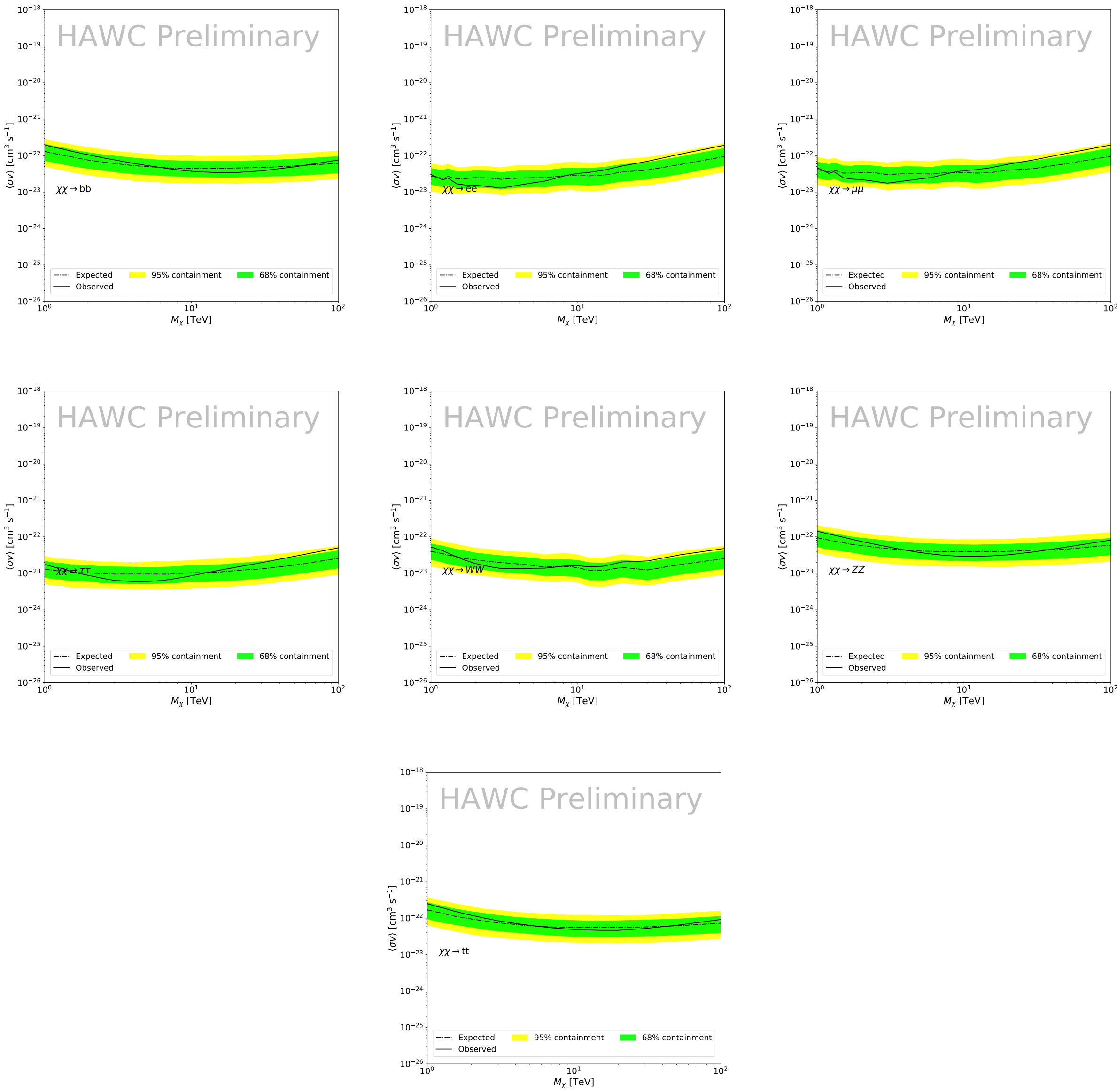

Figure 6.7 HAWC Brazil bands at 95% confidence level on $\langle\sigma v\rangle$versus DM mass for seven annihilation channels with J-factors from $\mathcal{GS}$ [53]. The solid line represents the combined limit from 13 dSphs. The dashed line is the expected limit. The green band is the 68% containment. The yellow band is the 95% containment.

6.6 Glory Duck Combined Results

The crux of this analysis is that HAWC's results are combined with 4 other gamma-ray observatories: Fermi-LAT, H.E.S.S., MAGIC, and VERITAS. No significant DM emission was observed by any of the five instruments. We present the upper limits on $\langle\sigma v\rangle$assuming seven independent DM self annihilation channels, namely W^+W^-, Z^+Z^-, $b\bar{b}$, $t\bar{t}$, e^+e^-, $\mu^+\mu^-$, and $\tau^+\tau^-$. The 68%

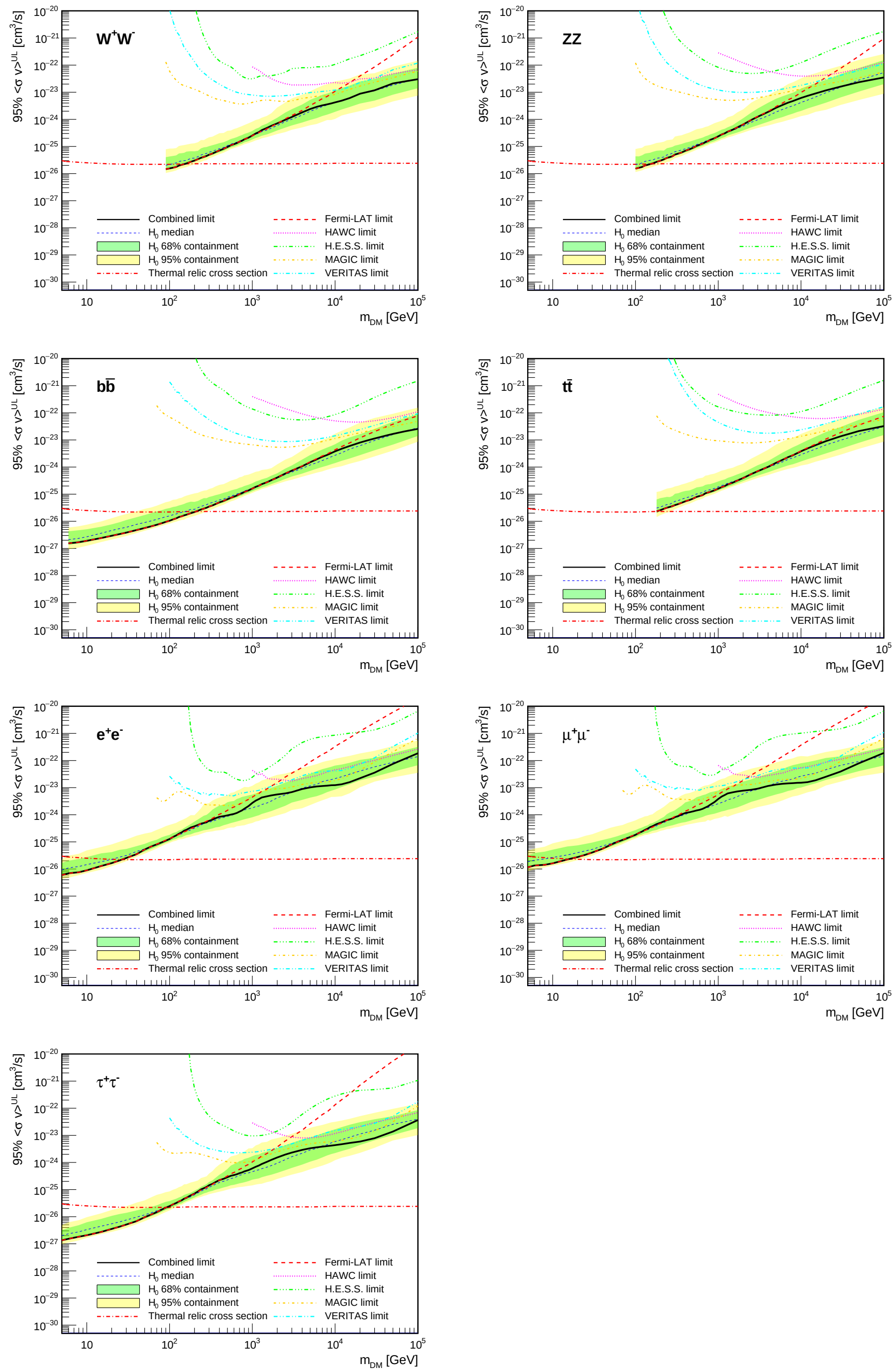

Figure 6.8 Upper limits at 95% confidence level on $\langle\sigma v\rangle$in function of the DM mass for eight annihilation channels, using the set of J factors from Ref. [53] ($\mathcal{GS}$ set in Table 6.1). The black solid line represents the observed combined limit, the black dashed line is the median of the null hypothesis corresponding to the expected limit, while the green and yellow bands show the 68% and 95% containment bands. Combined upper limits for each individual detector are also indicated as solid, colored lines. The value of the thermal relic cross-section in function of the DM mass is given as the red dotted-dashed line [54].

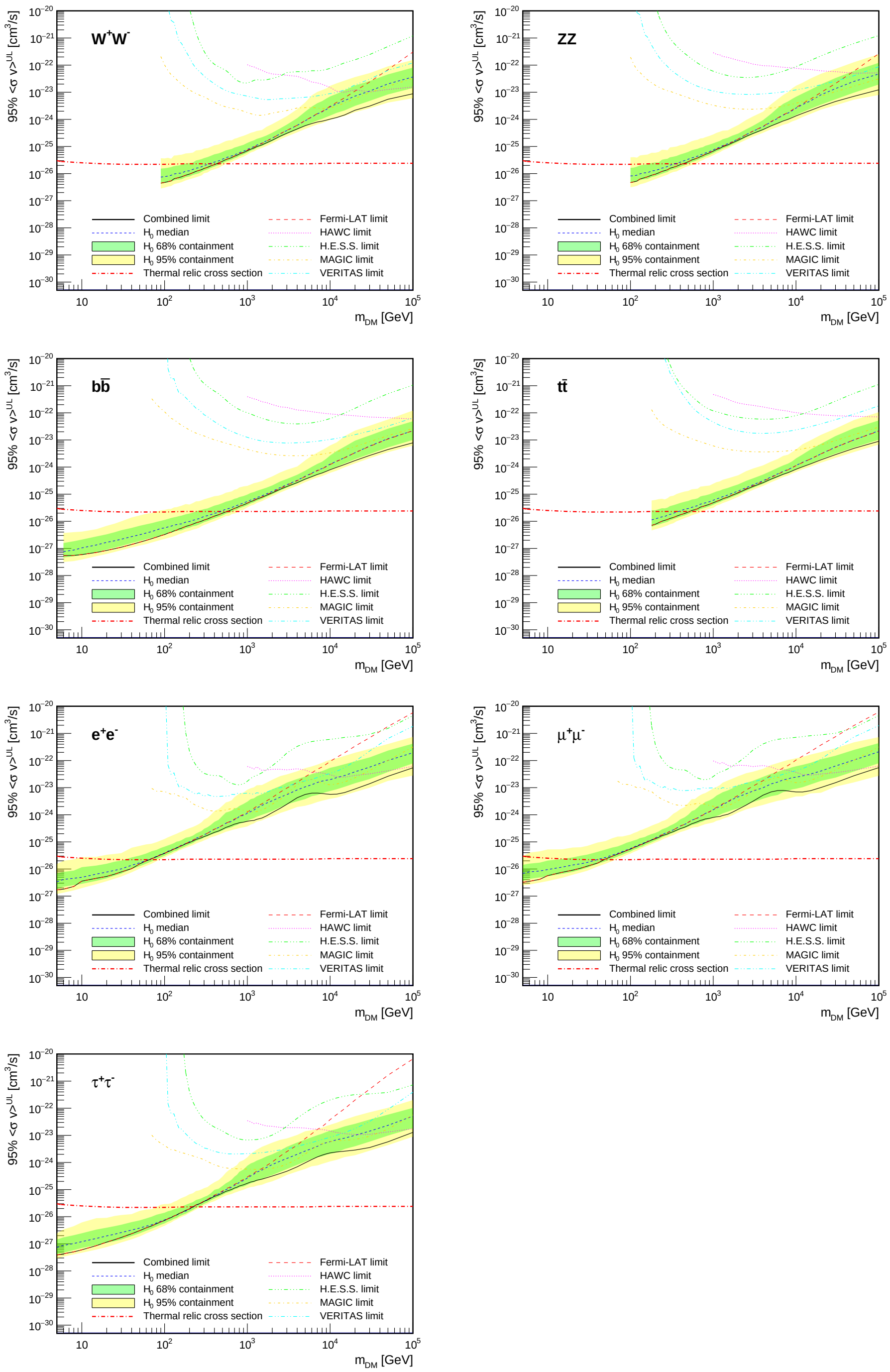

Figure 6.9 Same as Fig. 6.8, using the set of J factors from Ref. [47, 55] ($\mathcal{B}$ set in Table 6.1).

and 95% containment bands are produced from 300 Poisson realizations of the null hypothesis corresponding to each of the combined datasets. These 300 realizations are combined identically to dSph observations. The containment bands and the median are extracted from the distribution of resulting limits on the null hypothesis. These 300 realizations are obtained either by fast simulations of the OFF observations, for H.E.S.S., MAGIC, VERITAS, and HAWC, or taken from real observations of empty fields of view in the case of Fermi-LAT [48, 56, 57].

The obtained limits are shown in Figure 6.8 for the $\mathcal{GS}$ set of J-factors [53] and in Figure 6.9 for the $\mathcal{B}$ set of J-factors [47, 55]. The combined limits are presented with their 68% and 95% containment bands, and are expected to be close to the median limit when no signal is present. We observe agreement with the null hypothesis for all channels, within 2σ standard deviations, between the observed limits and the expectations given by the median limits. Limits obtained from each detector are also indicated in the figures, where limits for all dSphs observed by the specific instrument have been combined.

Below ~300 GeV, the $Fermi$-LAT dominates the DM limits for all annihilation channels. From ~300 GeV to ~2 TeV, $Fermi$-LAT continues to dominate for the hadronic and bosonic DM channels, yet the IACTs (H.E.S.S., MAGIC, and VERITAS) and $Fermi$-LAT all contribute to the limit for leptonic DM channels. For DM masses between ~2 TeV to ~10 TeV, the IACTs dominate leptonic DM annihilation channels, whereas both the $Fermi$-LAT and the IACTs dominate bosonic and hadronic DM annihilation channels. From ~10 TeV to ~100 TeV, both the IACTs and HAWC contribute significantly to the leptonic DM limit. For hadronic and bosonic DM, the IACTs and $Fermi$-LAT both contribute strongly.

We notice that the limits computed using the $\mathcal{B}$ set of J-factor are always better compared to the ones calculated with the $\mathcal{GS}$ set. For the W^+W^-, Z^+Z^-, $b\bar{b}$, and $t\bar{t}$ channels, the ratio between the limits computed with the two sets of J-factor is varying between a factor of ~3 and ~5 depending on the energy, with the largest ratio around 10 TeV. For the channels e^+e^-, $\mu^+\mu^-$, and $\tau^+\tau^-$, the ratio lies between ~2 to ~6, being maximum around 1 TeV. Examining Figure 6.16 and Figure 6.17 in Section 6.8, these differences are explained by the fact that the $\mathcal{B}$ set provides higher J-factors for the majority of the studied dSphs, with the notable exception of Segue I. The variation on the ratio of the limits for the two sets is due to different dSph dominating the limits depending on the energy. This pushes the range of thermal cross-section which can be excluded to higher mass. This comparison demonstrates the magnitude of systematic uncertainties associated with the choice of

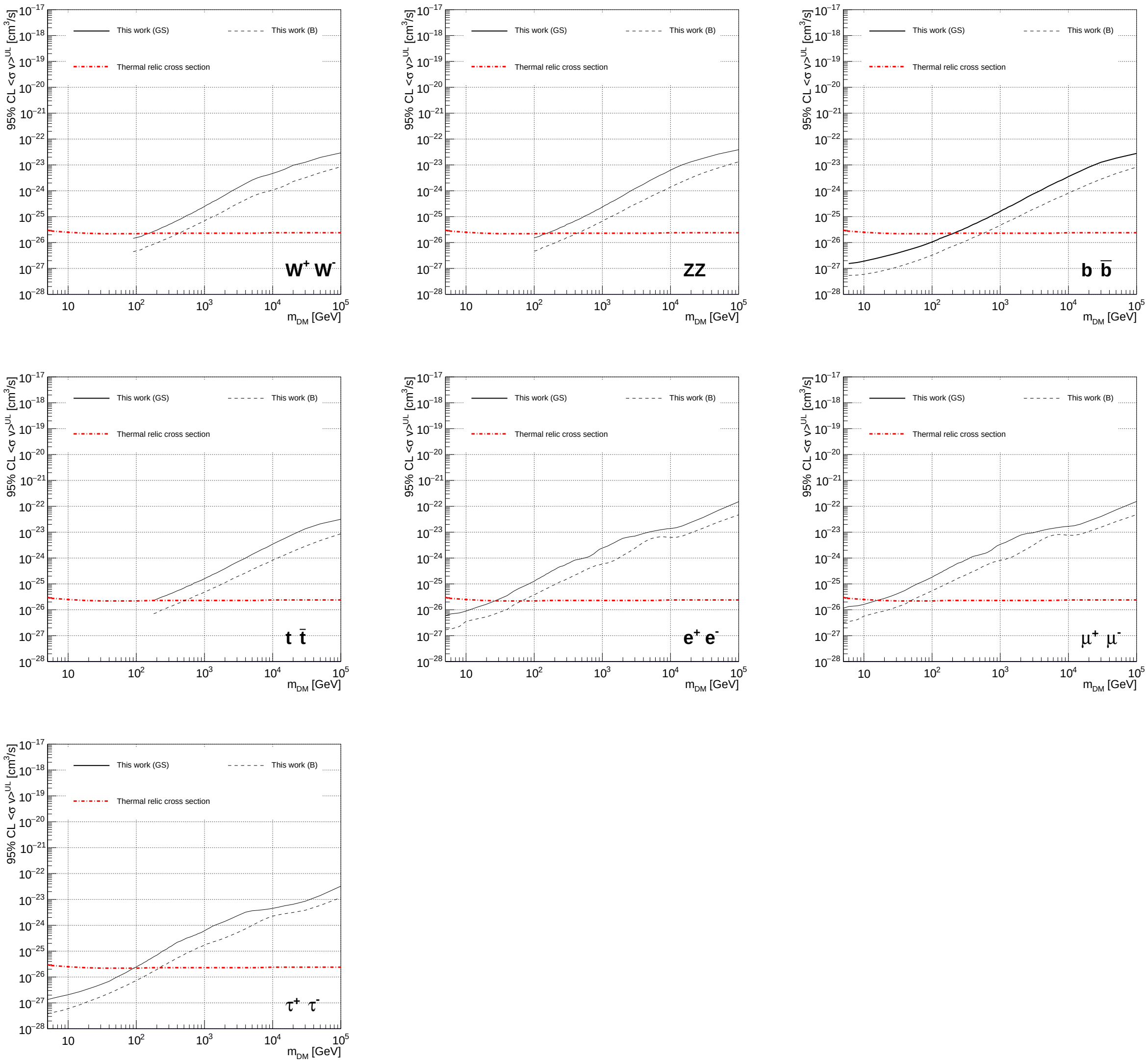

Figure 6.10 Comparisons of the combined limits at 95% confidence level for each of the eight annihilation channels when using the J factors from Ref. [53] ($\mathcal{GS}$ set in Table 6.1), plain lines, and the J factor from Ref. [47, 55] ($\mathcal{B}$ set in Table 6.1), dashed lines. The cross-section given by the thermal relic is also indicated [54].

the J-factor

This comparison demonstrates the magnitude of systematic uncertainties associated with the choice of the J-factor calculation. The $\mathcal{GS}$ and $\mathcal{B}$ sets present a difference in the limits for all channels of about This difference is explained, see Figure 6.16 and Figure 6.17 in Appendix, by the fact that the $\mathcal{B}$ set provides higher J factors for all dSph except for Segue I. This pushes the range of thermal cross-section which can be excluded to higher mass.

6.7 HAWC Systematics

6.7.1 Inverse Compton Scattering

The DM-DM annihilation channels produce many high energy electrons regardless of the primary annihilation channel. These high energy electrons can produce high energy gamma-rays through Inverse Compton Scattering (ICS). If this effect is strong, it would change the morphology of the source and increase the total expected gamma-ray counts from any source. The PPPC [44] provides tools in Mathematica for calculating the impact of ICS for an arbitrary location in the sky for a specified annihilation channel. We calculated the change in gamma-ray counts for DM annihilation to primary $e\bar{e}$ for RA and Dec corresponding to Segue1 and Coma Berenices. These dSphs were chosen because they are the strongest contributors to the limit. $e\bar{e}$ was selected because it would have the largest number of high energy electrons. The effect was found to be on the order of 10^{-7} on the gamma-ray spectrum. As a result, this systematic is not considered in our analysis.

6.7.2 Point Source Versus Extended Source Limits

The previous DM search toward dSph approximated the dSphs as point sources [46]. In this analysis, the dSphs are implemented as extended with J-factor distributions following those produced by [53]. The resolution of the cited map is much finer than HAWC's angular resolution. The vast majority of the J-factor distribution is represented on the central HAWC pixel of the dSph spatial map. However, the neighboring 8 pixels are not negligible and contribute to our limit.

Figure 6.11 shows a substantial improvement to the limit for Segue1. Fig. 6.12 however showed identical limits. These disparities are best explained by the relative difference in their J-Factors. Both dSphs pass almost overhead the HAWC detector, however Segue1 has the larger J-Factor between the two. Adjacent pixels to the central pixel will therefor contribute to the limits. This is the case for other dSph that are closer to overhead the HAWC detector.

Comparison plots for all sources and the combined limit can be found in the sandbox for the Glory Duck project.

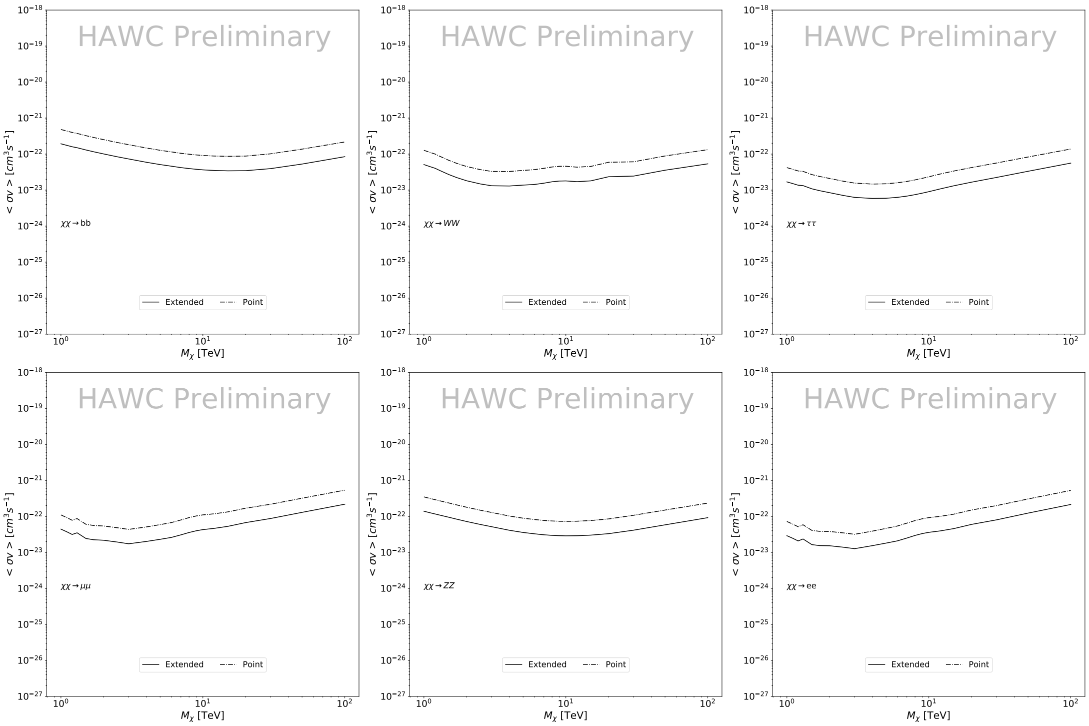

Figure 6.11 Comparisons of the combined limits at 95% confidence level for a point source analysis and extended source using [53] $\mathcal{GS}$ J-factor distributions and PPPC [44] annihilation spectra. Shown are the limits for Segue1 which will have the most significant impact on the combined limit. 6 of the 7 DM annihilation channels are shown. Solid lines are extended source studies. Dashed lines are point source studies. Overall, the extended source analysis improves the limit by a factor of 2.

6.7.3 Impact of Pointing Systematic

During the analysis it was discovered that reconstruction of gamma-rays. Slides describing this systematic can be found here. Shown on the presentation is dependence on the pointing systematic on declination. New spatial profiles were generated for every dSph and limits were computed for the adjusted declination.

Section 6.7.3 demonstrates the impact of this systematic for all DM annihilation channels studied by HAWC. The impact is a tiny improvement, yet mostly identical, to the combined limits.

6.8 J-factor distributions

6.8.1 Numerical integration of $\mathcal{GS}$ maps

It was discovered well after the HAWC analysis was completed that the published tables from $\mathcal{GS}$ [45] quoted median J-factors were computed in a non-trivial manner. The assumption myself

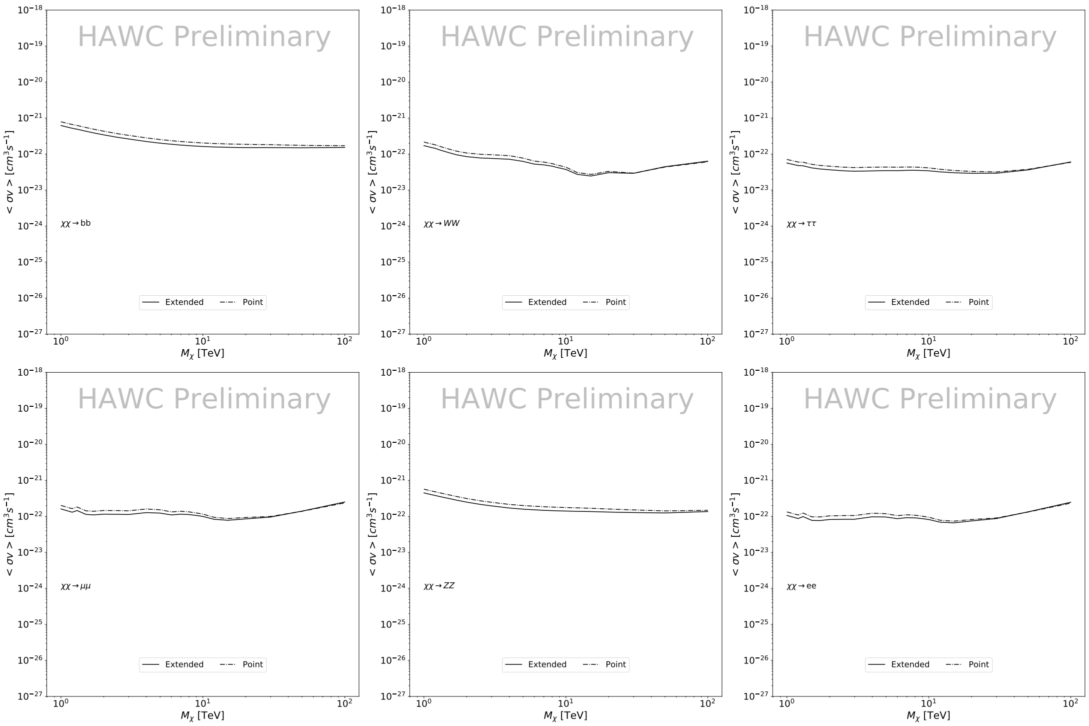

Figure 6.12 Same as Fig. 6.11 on Coma Berenices. This dSph also contributes significantly to the limit. The limits are identical in this case.

and collaborators had been that the published tables represented the J-factor as a function of θ for the best global fit model on a per-source basis. However, this is not the case. Instead, what is published are the best fit model for each dwarf that only considers stars up to the angular separation θ. Therefore, the model is changing for each value of θ for each dwarf. Yet, the introduced features from unique models at each θ are much smaller than the angular resolution of HAWC. It is not expected for these effects to impact the limits and TS greatly as a result.

Median J-factor model profiles were provided by the authors. New maps were generated and analyzed for Segue1 and Coma Berenices. Figure 6.14 shows the differential between maps generated with the method from Section 6.8.1 and from the authors of [45]. These maps were reanalyzed for all SM DM annihilation channels. Upper limits for these channels are shown in Figure 6.15

From Figure 6.15, we can see that the impact of these model difference was no substantial. The observed impact was a fractional effect which is much smaller than the impact from selecting another DM spatial distribution model as was shown in Figure 6.10.

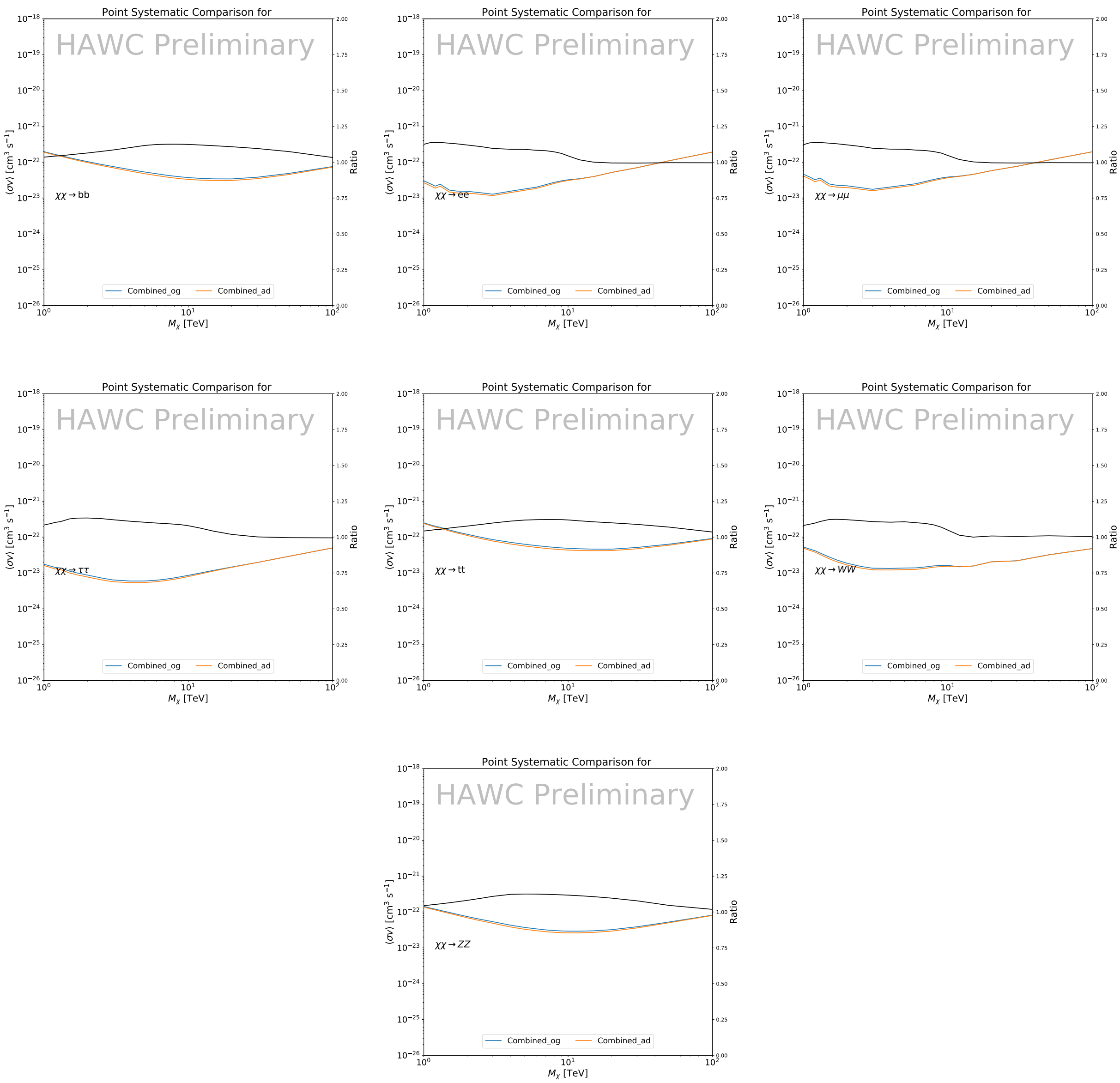

Figure 6.13 Comparison of combined limits when correcting for HAWC's pointing systematic. All DM annihilation channels are shown. The solid black line is the ratio between published limit to the declination corrected limit. The blue solid line or "Combined_og" represented the limits computed for Glory Duck. The solid orange line or "Combined_ad" represented the limits computed after correcting for the pointing systematic.

6.8.2 $\mathcal{GS}$ Versus $\mathcal{B}$ spatial models

We show in this appendix a comparison between the J-factors computed by Geringer-Sameth *et al.* [53] (the $\mathcal{GS}$ set) and the ones computed by Bonnivard *et al.* [47, 55] (the $\mathcal{B}$ set). The $\mathcal{GS}$ J-factors are computed through a Jeans analysis of the kinematic stellar data of the selected

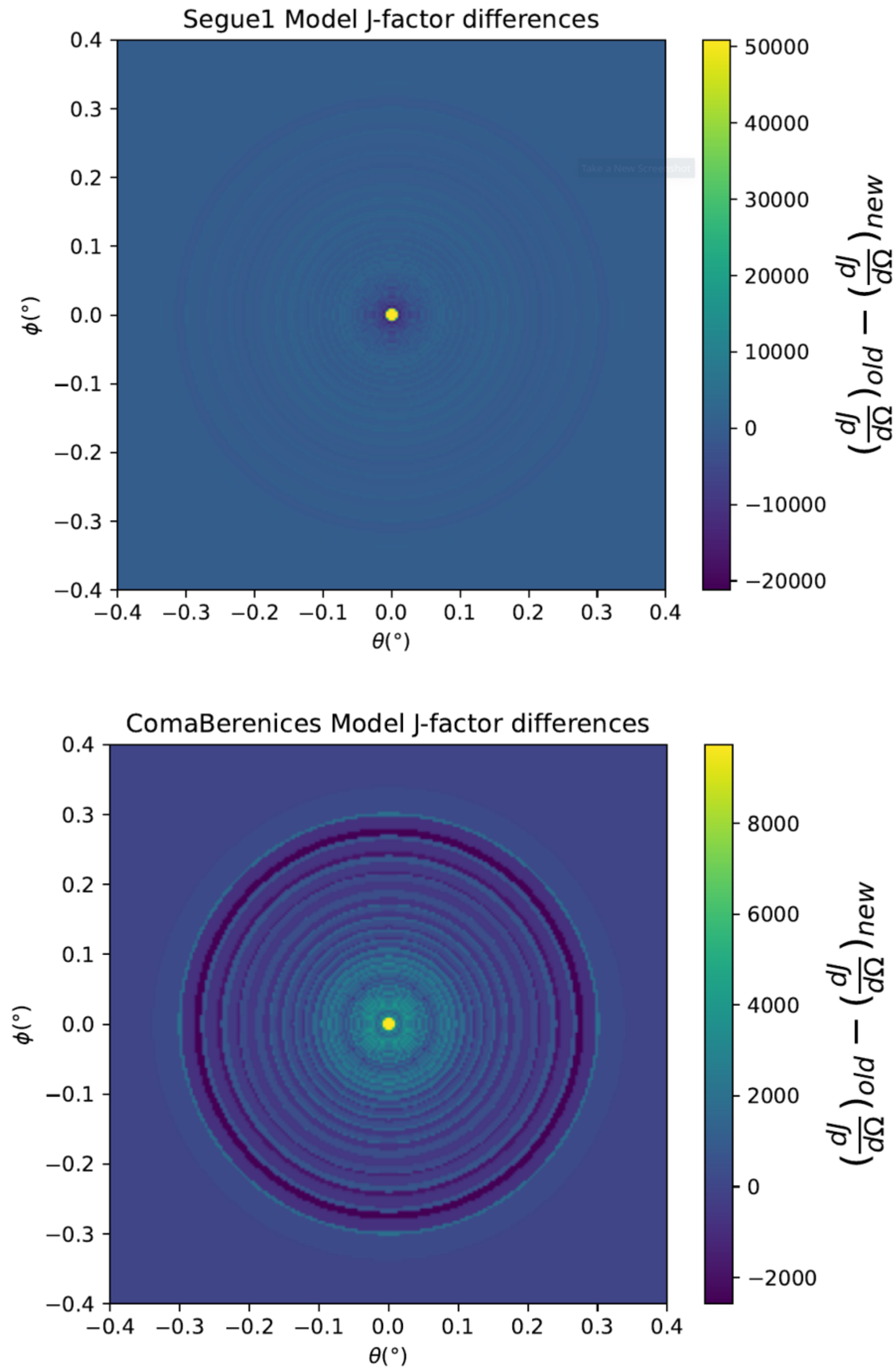

Figure 6.14 Differential map of dJ/Ω from model built in Section 6.8.1 and profiles provided directly from authors. (Top) Differential from Segue1. (bottom) Differential from Coma Berenices. Note that their scales are not the same. Segue1 shows the deepest discrepancies which is congruent with its large uncertainties. Both models show anuli where unique models become apparent.

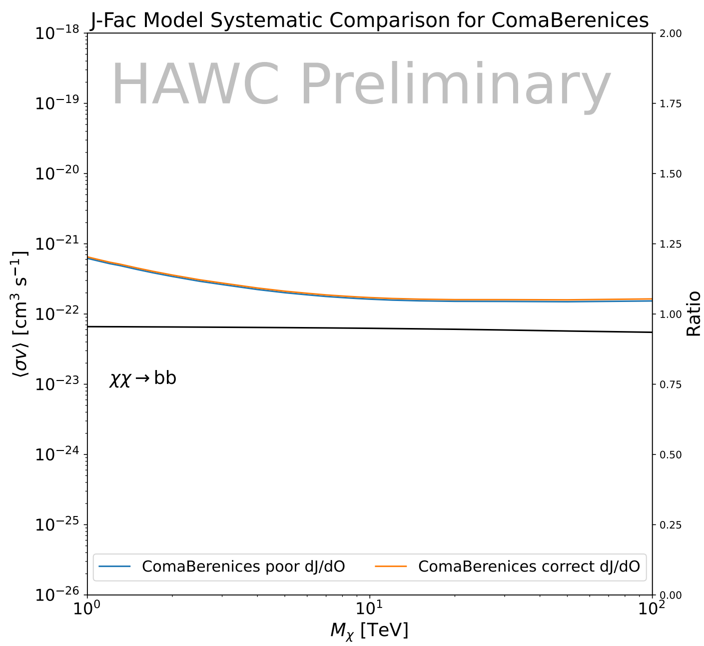

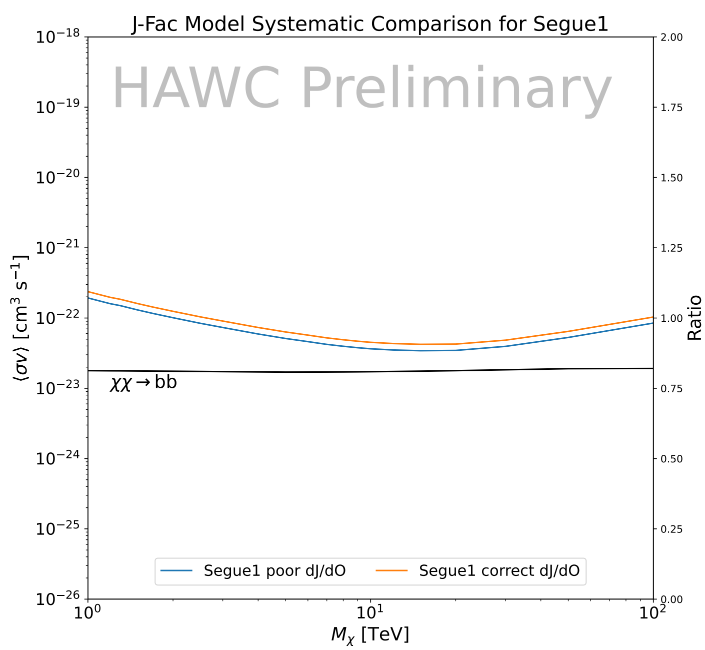

Figure 6.15 HAWC limits for Coma Berenices (top) and Segue1 (bottom) for two different map sets. Blue lines are limits calculated on maps with poor model representation. Orange lines are limits calculated on spatial profiles provided by the authors of [45]. Black line is the ratio of the poor spatial model limits to the corrected spatial models. The left y-axis measures $\langle \sigma v \rangle$for the blue and orange lines. The right y-axis measures the ratio and is unitless.

dSphs, assuming a dynamic equilibrium and a spherical symmetry for the dSphs. They adopted the generalized DM density distribution, known as Zhao-Hernquist, introduced by [58], carrying three additional index parameters to describe the inner and outer slopes, and the break of the density profile. Such a profile parametrization allows the reduction of the theoretical bias from the choice of a specific radial dependency on the kinematic data. In other words, the increase of free parameters with the use of the Zhao-Hernquist profile allows a better description of the mass density distribution of dark matter.

In addition, a constant velocity anisotropy profile and a Plummer light profile [59] for the stellar distribution were assumed. The velocity anisotropy profile depends on the radial and tangential velocity dispersion. However, its determination remains challenging since only the line-of-sight velocity dispersion can be derived from velocity measurements. Therefore, the parametrization of the anisotropy profile is obtained from simulated halos (see [60] for more details). They provide the values of the J-factors of regions extending to various angular radius up to the outermost member star.

The $\mathcal{B}$ J-factors were computed through a Jeans analysis taking into account the systematic uncertainties induced by the DM profile parametrization, the radial velocity anisotropy profile, and the triaxiality of the halo of the dwarf galaxies. They performed a more complete study of the dSph kinematics and dynamics than $\mathcal{GS}$ for the determination of the J-factor. Conservative values of the J-factors where obtained using an Einasto DM density profile [61], a realistic anisotropy profile known as the Baes & Van Hese profile [62] which takes into account that the inner regions can be significantly non-isotropic, and a Zhao-Hernquist light profile [58].

For both sets, J-factor values are provided for all dSphs as a function of the radius of the integration region [53, 47, 55]. Table 6.1 shows the heliocentric distance and Galactic coordinates of the twenty dSphs, together with the two sets of J-factor values integrated up to the outermost observed star for $\mathcal{GS}$ and the tidal radius for $\mathcal{B}$. Both J-factor sets were derived through a Jeans analysis based on the same kinematic data, except for Draco where the measurements of [63] have been adopted in the computation of the $\mathcal{B}$ value. The computations for producing the $\mathcal{GS}$ and $\mathcal{B}$

samples differ in the choice of the DM density, velocity anisotropy, and light profiles, for which the set $\mathcal{B}$ takes into account some sources of systematic uncertainties.

Figure 6.16 and Figure 6.17 show the comparisons for the J-factor versus the angular radius for each of the 20 dSphs used in this study. The uncertainties provided by the authors are also indicated in the figures. For the $\mathcal{GS}$ set, the computation stops at the angular radius corresponding to the outermost observed star, while for the $\mathcal{B}$ set, the computation stops at the angular radius corresponding to the tidal radius.

6.9 Discussion and Conclusions

In this multi-instrument analysis, we have used observations of 20 dSphs from the gamma-ray telescopes Fermi-LAT, H.E.S.S., MAGIC, VERITAS, and HAWC to perform a collective DM search annihilation signals. The data were combined across sources and detectors to significantly increase the sensitivity of the search. We have observed no significant deviation from the null, no DM, hypothesis, and so present our results in terms of upper limits on the annihilation cross-section for seven potential DM annihilation channels.

Fermi-LAT brings the most stringent constraints for continuum channels below approximately 1 TeV. The remaining detectors dominate at higher energies. Overall, for multi-TeV DM mass, the combined DM constraints from all five telescopes are 2-3 times stronger than any individual telescope for multi-TeV DM.

Derived from observations of many dSphs, our results produce robust limits given the DM content of the dSphs is relatively well constrained. The obtained limits span the largest mass range of any WIMP DM search. Our combined analysis improves the sensitivity over previously published results from each detector which produces the most stringent limits on DM annihilation from dSphs. These results are based on deep exposures of the most promising known dSphs with the currently most sensitive gamma-ray instruments. Therefore, our results constitute a legacy of a generation of gamma-ray instruments on WIMP DM searches towards dSphs. Our results will remain the reference in the field until a new generation of more sensitive gamma-ray instruments begin operations, or until new dSphs with higher J-factors are discovered.

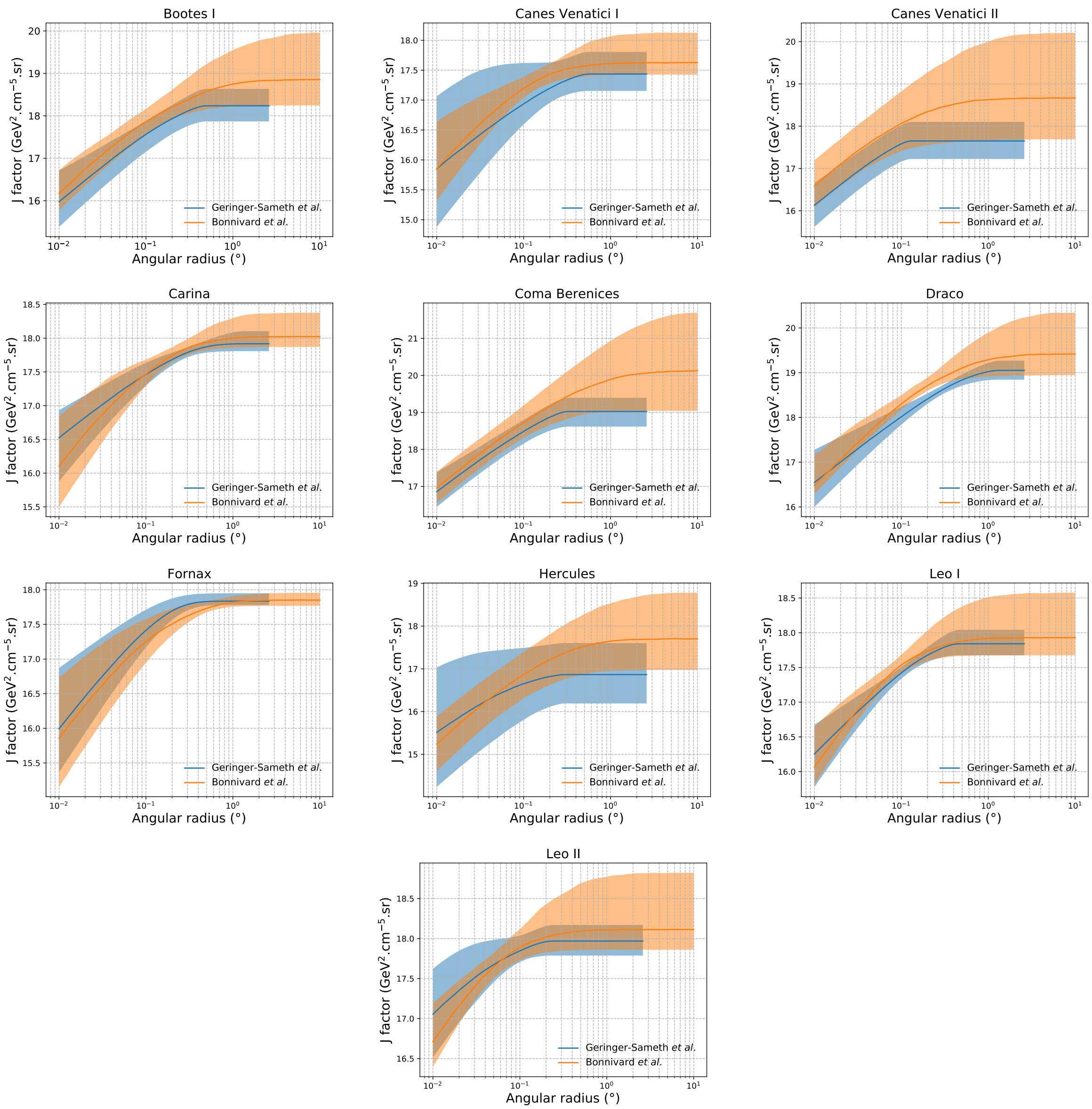

Figure 6.16 Comparisons between the J-factors versus the angular radius for the computation of J factors from Ref. [53] ($\mathcal{GS}$ set in Table 6.1) in blue and for the computation from Ref. [47, 55] ($\mathcal{B}$ set in Tab. 6.1) in orange. The solid lines represent the central value of the J-factors while the shaded regions correspond to the 1σ standard deviation.

This analysis serves as a proof of concept for future multi-instrument and multi-messenger combination analyses. With this collaborative effort, we have managed to sample over four orders in magnitude in gamma-ray energies with distinct observational techniques. Determining the nature of DM continues to be an elusive and difficult problem. Larger datasets with diverse measurement techniques could be essential to tackling the DM problem. A future collaboration using similar

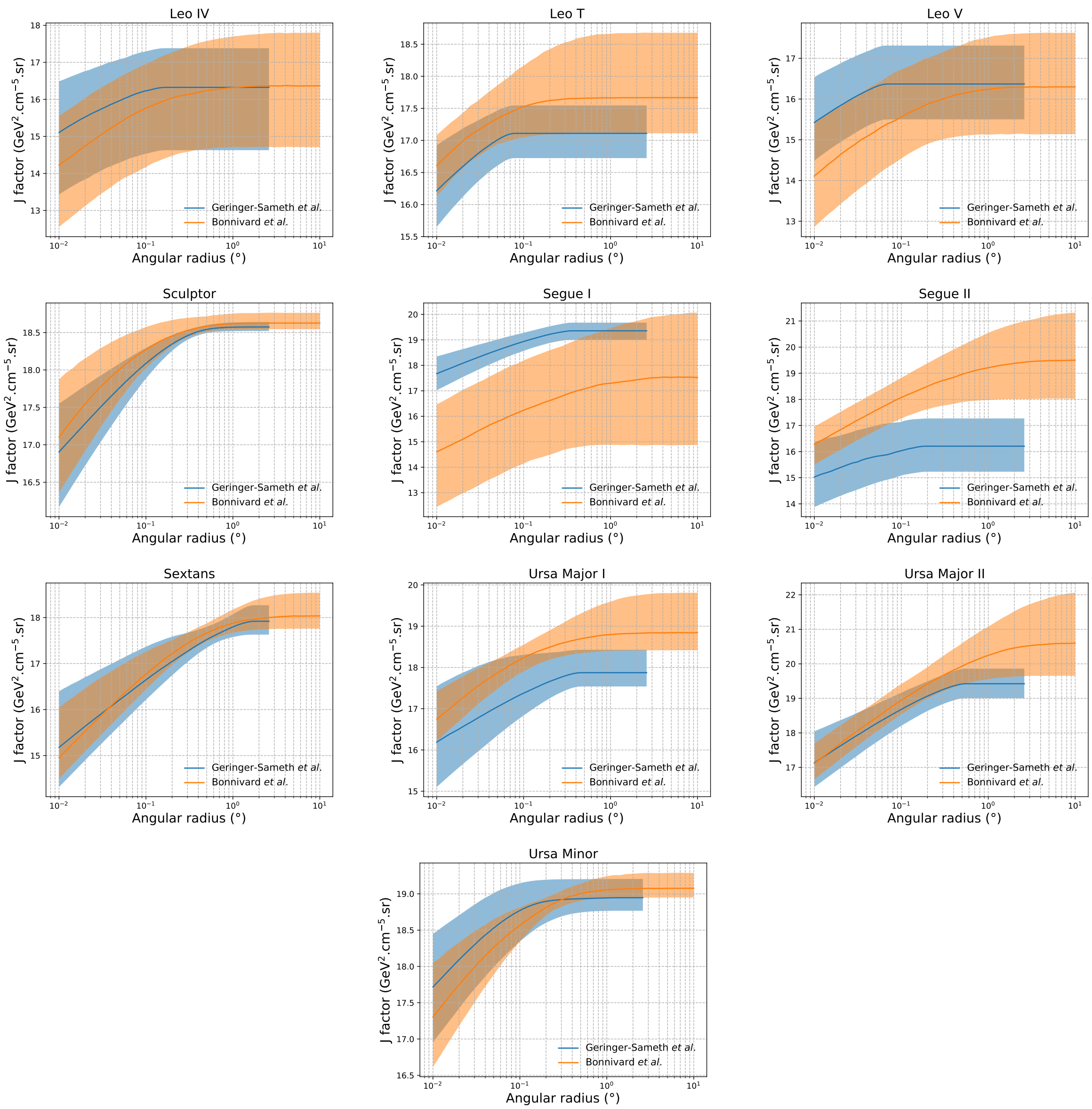

Figure 6.17 Comparisons between the J-factors versus the angular radius for the computation of J factors from Ref. [53] ($\mathcal{GS}$ set in Tab. 6.1) in blue and for the computation from Ref. [47, 55] ($\mathcal{B}$ set in Tab. 6.1) in orange. The solid lines represent the central value of the J-factors while the shaded regions correspond to the 1σ standard deviation.

techniques as the ones described in this paper could grow even beyond gamma rays. The models we used for this study include annihilation channels with neutrinos in the final state. Advanced studies could aim to merge our results with those from neutrino observatories with large data sets. Efforts are already underway to add data from the IceCube, ANTARES, and KM3NeT observatories to these gamma-ray results.

From this work, a selection of the best candidates for observations, according to the latest knowledge on stellar dynamics and modelling techniques for the derivation of the J-factors on the potential dSphs targets, is highly desirable at the time that new experiments are starting their dark matter programs using dSphs. Given the systematic uncertainty inherent to the derivation of the J-factors, an informed observational strategy would be to select both objects with the highest J-factors that could lead to DM signal detection, and objects with robust J-factor predictions, i.e. with kinematic measurements on many bright stars, which would strengthen the DM interpretation reliability of the observation outcome.

This analysis combines data from multiple telescopes to produce strong constraints on astrophysical objects. From this perspective, these methods can be applied beyond just DM searches. Almost every astrophysical study can benefit from multi-telescope, multi-wavelength gamma-ray studies. We have enabled these telescopes to study the cosmos with greater precision and detail. Many astrophysical searches can benefit from multi-instrument gamma-ray studies, for which our analysis lays the foundation.

CHAPTER 7

MULTITHREADING HAWC ANALYSES FOR DARK MATTER SEARCHES

7.1 Introduction

HAWC's current software suite, plugins to 3ML, does not fully utilize computational advancements of recent decades. Said advancements include the proliferation of Graphical Processing Units (GPUs), and multithreading on multi-core processors. The analysis described in chapter 6 took up to 3 months of human time waiting for the full gambit of data analysis and simulation of background to run. Additionaly, with the addition of a 2D binning scheme, f_{hit} and NN, the compute time is expected to grow. Although excessive computing time was, in part, from an intense use of a shared computing cluster, it was evident that there was room for improvement. In HAWC's next generation dSph DM search, I decided to develop codes that would utilize the multi-core processors on modern high performance computing clusters. The results of this work are featured in this chapter and brought a human timing improvement to computation that scales as $1/N$ where N is the number of threads.

7.2 Dataset and Background

This section enumerates the data and background methods used for HAWC's multi-threaded study of dSphs. Section 7.2.1 and Section 7.2.2 are most useful for fellow HAWC collaborators looking to replicate a multithreaded dSph DM search.

7.2.1 Itemized HAWC files

- Detector Resolution: `refit-Pass5-Final-NN-detRes-zenith-dependent.root`
- Data Map: `Pass5-Final-NN-maptree-ch103-ch1349-zenith-dependent.root`
- Spectral Dictionary: `HDMSpectra_dict_gamma.npy`

7.2.2 Software Tools and Development

This analysis was performed using HAL and 3ML [42, 43] in Python version 3. I built software in collaboration with Michael Martin and Letrell Harris to implement the *Dark Matter Spectra from* *the Electroweak to the Planck Scale* (HDM) [64] and dSphs spatial model from [65] for HAWC analysis. A NumPy dictionary of HDM was made for Py3. The corresponding Python3 file is `HDMSpectra_dict_gamma.npy`. These files can also be used for decay channels and tools are provided in HDM's git repository [64]. The analysis was performed using the Neural Network energy estimator for Pass 5.F. A description of this estimator was provided in chapter 4. TODO: define a subsection when it's writtenAll other software used for data analysis, DM profile generation, and job submission to SLURM are also kept in my sandbox in the Dark Matter HAWC project. The above repository also incorporates the model inputs used previously in Glory Duck, described in chapter 6

7.2.3 Data Set and Background Description

The HAWC data maps used for this analysis contain 2565 days of data between runs 2104 (TODO: Day start) and 7476 (TODO: day end). They were generated from pass 4.0 reconstruction. The analysis is performed using the NN energy estimator with bin list:

`B1C0Ea`, `B1C0Eb`, `B1C0Ec`, `B1C0Ed`, `B1C0Ee`, `B2C0Ea`, `B2C0Eb`, `B2C0Ec`, `B2C0Ed`, `B2C0Ee`, `B3C0Ea`, `B3C0Eb`, `B3C0Ec`, `B3C0Ed`, `B3C0Ee`, `B3C0Ef`, `B4C0Eb`, `B4C0Ec`, `B4C0Ed`, `B4C0Ee`, `B4C0Ef`, `B5C0Ec`, `B5C0Ed`, `B5C0Ee`, `B5C0Ef`, `B5C0Eg`, `B6C0Ed`, `B6C0Ee`, `B6C0Ef`, `B6C0Eg`, `B6C0Eh`, `B7C0Ee`, `B7C0Ef`, `B7C0Eg`, `B7C0Eh`, `B7C0Ei`, `B8C0Ee`, `B8C0Ef`, `B8C0Eg`, `B8C0Eh`, `B8C0Ei`, `B8C0Ej`, `B9C0Ef`, `B9C0Eg`, `B9C0Eh`, `B9C0Ei`, `B9C0Ej`, `B10C0Eg`, `B10C0Eh`, `B10C0Ei`, `B10C0Ej`, `B10C0Ek`, `B10C0El`

Bin 0 was excluded as it has substantial hadronic contamination and poor angular resolution.

Background considerations and source selection was identical to Section 6.2, and no additional arguements are provided here. Many of the HAWC systematics explored in Section 6.7 also apply for this DM search and are not added upon here.

7.3 Analysis

The analysis and its systematics are almost identical to Section 6.3. Importantly, we use the same Equation (6.1) and Equation (6.2) for estimating the gamma-ray flux at HAWC from our sources. We add on to the previous study with a search for DM decay. The flux equations for DM decay are

$$\frac{d\Phi_\gamma}{dE_\gamma} = \frac{1}{4\pi\tau m_\chi}\frac{dN_\gamma}{dE_\gamma} \times \int_{\text{source}} d\Omega \int_{l.o.s} \rho_\chi dl(r,\theta') \tag{7.1}$$

with a new quantity, the D factor, defined as

$$D = \int d\Omega \int_{l.o.s} dl\rho_\chi(r,\theta') \tag{7.2}$$

Software was written to accomodate DM decay from dSphs, however decay profiles were not received from $\mathcal{LS}$ by the time of writing this tehsis.

7.3.1 $\frac{dN_\gamma}{dE_\gamma}$ - Particle Physics Component

For these spectra, we import HDM with Electroweak (EW) corrections and additional corrections for neutrinos above the EW scale [64]. The spectrum is implemented as a model script in astromodels for 3ML. A comprehensive description of EW corrections and neutrino considerations are provided later in TODO: refeance MM nu duck.

Figure 7.1 demonstrates the impact of changes from HDM on DM annihilation to W bosons. A class in astromodels was developed to include HDM and is aptly named `HDMSpectra` within `DM_models.py`. The SM DM annihilation channels studied here are $\chi\chi \rightarrow$:

$$e^+e^-,\ \mu^+\mu^-,\ \tau^+\tau^-, b\bar{b},\ t\bar{t},\ gg,\ W^+W^-,\ ZZ,\ c\bar{c},\ u\bar{u},\ d\bar{d},\ s\bar{s},\ \nu_e\overline{\nu_e},\ \nu_\mu\overline{\nu_\mu},\ \nu_\tau\overline{\nu_\tau},\ \gamma\gamma,\ hh.$$

For $\gamma\gamma$ and ZZ, a substantial fraction of the signal photons are expected to have total energy equal m_χ [64]. This introduces a δ-function that is much narrower than the energy resolution of the HAWC detector. To ensure that this feature is not lost in the likelihood fits, the 'line' feature is convolved with a gausian kernel with a 1σ width of $0.05 \cdot m_\chi$ and total kernel window of $\pm 4\sigma$. This difers from HAWC's previous line study where 30% of HAWC's energy resolution was used for the kernel [66]. The NN energy estimator's strength compared to f_{hit} at low gamma-ray energy enables smaller resolutions in addition to low energy tails in the spectral models [64]. $\chi\chi \rightarrow \gamma\gamma$ and ZZ spectral hypotheses are shown in Figure 7.2. Spectral models for the remaining annihilation channels are plotted for each m_χ in Figure B.1.

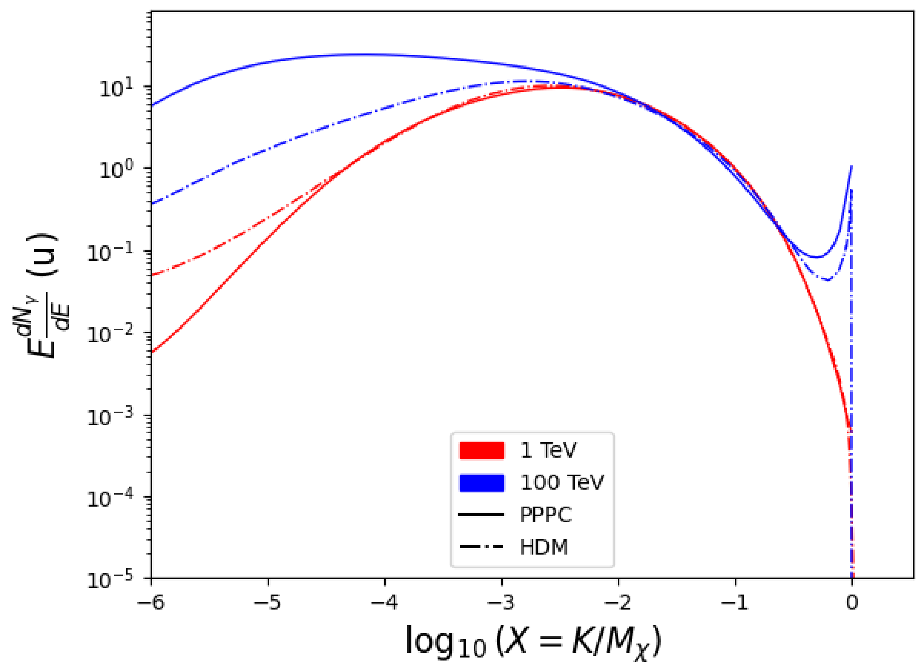

Figure 7.1 Difference between spectral hypotheses from PPPC [44] and HDM [64]. Shown is the expected DM annihilation spectrum for $\chi\chi \to W^-W^+$. Solid lines are spectral models with EW corrections from the PPPC. Dash-dot lines are spectral models from HDM. Red lines are models for $M_\chi = 1$ TeV. Blue lines represent models for $M_\chi = 100$ TeV.

7.3.2 J and D- Astrophysical Components

The J-factor profiles for each source are imported from Louis Strigari et al. (referred to with $\mathcal{LS}$) [65]. Profiles in $\frac{dJ}{d\Omega}(\theta)$ up to $\theta = 0.5°$ were provided directly from the authors. Map generation from these profiles were almost identical to Section 6.3.2 except that a higher order trapezoidal integral was used for the normalization of the square, uniformly-spaced map:

$$p^2 \cdot \sum_{i=0}^{N} \sum_{j=0}^{M} w_{i,j} \frac{d\mathcal{K}}{d\Omega}(\theta_{i,j}, \phi_{i,j}) \tag{7.3}$$

$\mathcal{K}$ is either J or D for the spatial distributions of annihilation or decay respectively. p is the angular side of one pixel in the map. $w_{i,j}$ is a weight assigned the following ways:

$w_{i,j} = 1$ if $(\theta_{i,j}, \phi_{i,j})$ is fully within the region of integration

$w_{i,j} = 1/2$ if $(\theta_{i,j}, \phi_{i,j})$ is on an edge of the region of integration

$w_{i,j} = 1/4$ if $(\theta_{i,j}, \phi_{i,j})$ is on a corner of the region of integration

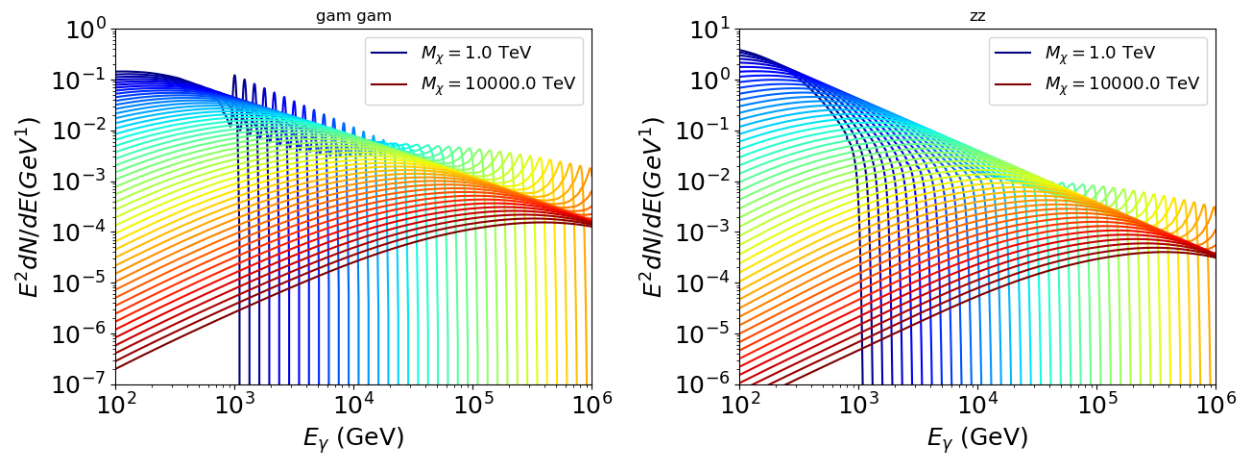

Figure 7.2 Photon spectra for $\chi\chi \to \gamma\gamma$ (left) and $\chi\chi \to ZZ$ (right) after gaussian convolution of line features. Both spectra have δ-features at photon energies equal to the DM mass. Bluer lines are annihilation spectra with lower DM mass. Redder lines are spectra from larger DM mass. All Spectral models are sourced from the Heavy Dark Matter models [64]. Axes are drawn roughly according to the energy sensitivity of HAWC.

Figure 7.3 shows the median and $\pm 1\sigma$ maps used as input for DM annihilation studied by $\mathcal{LS}$.

7.3.3 Source Selection and Annihilation Channels

HAWC's sources for this multithreaded analysis include Coma Berenices, Draco, Segue 1, and Sextans $\mathcal{LS}$ observes up to 43 sources in its publication, however only 4 of the best fit profiles were provided at the time this thesis was written. A full description of each source used in this analysis is found in Table 7.1.

This analysis improves on chapter 6 in the following ways. Previously, the particle physics

Name	Distance (kpc)	l, b (°)	$\log_{10} J$ ($\mathcal{LS}$ set) $\log_{10}(\mathrm{GeV}^2\mathrm{cm}^{-5}\mathrm{sr})$
Coma Berenices	44	241.89, 83.61	$19.00^{+0.36}_{-0.35}$
Draco	76	86.37, 34.72	$18.83^{+0.12}_{-0.12}$
Segue I	23	220.48, 50.43	$19.12^{+0.49}_{-0.58}$
Sextans	86	243.50, 42.27	$17.73^{+0.13}_{-0.12}$

Table 7.1 Summary of the relevant properties of the dSphs used in the present work. Column 1 lists the dSphs. Columns 2 and 3 present their heliocentric distance and galactic coordinates, respectively. Column 4 reports the J-factors of each source given from the $\mathcal{LS}$ studies and estimated $\pm 1\sigma$ uncertainties. The values $\log_{10} J$ ($\mathcal{LS}$ set) [65] correspond to the mean J-factor values for a source extension truncated at 0.5°.

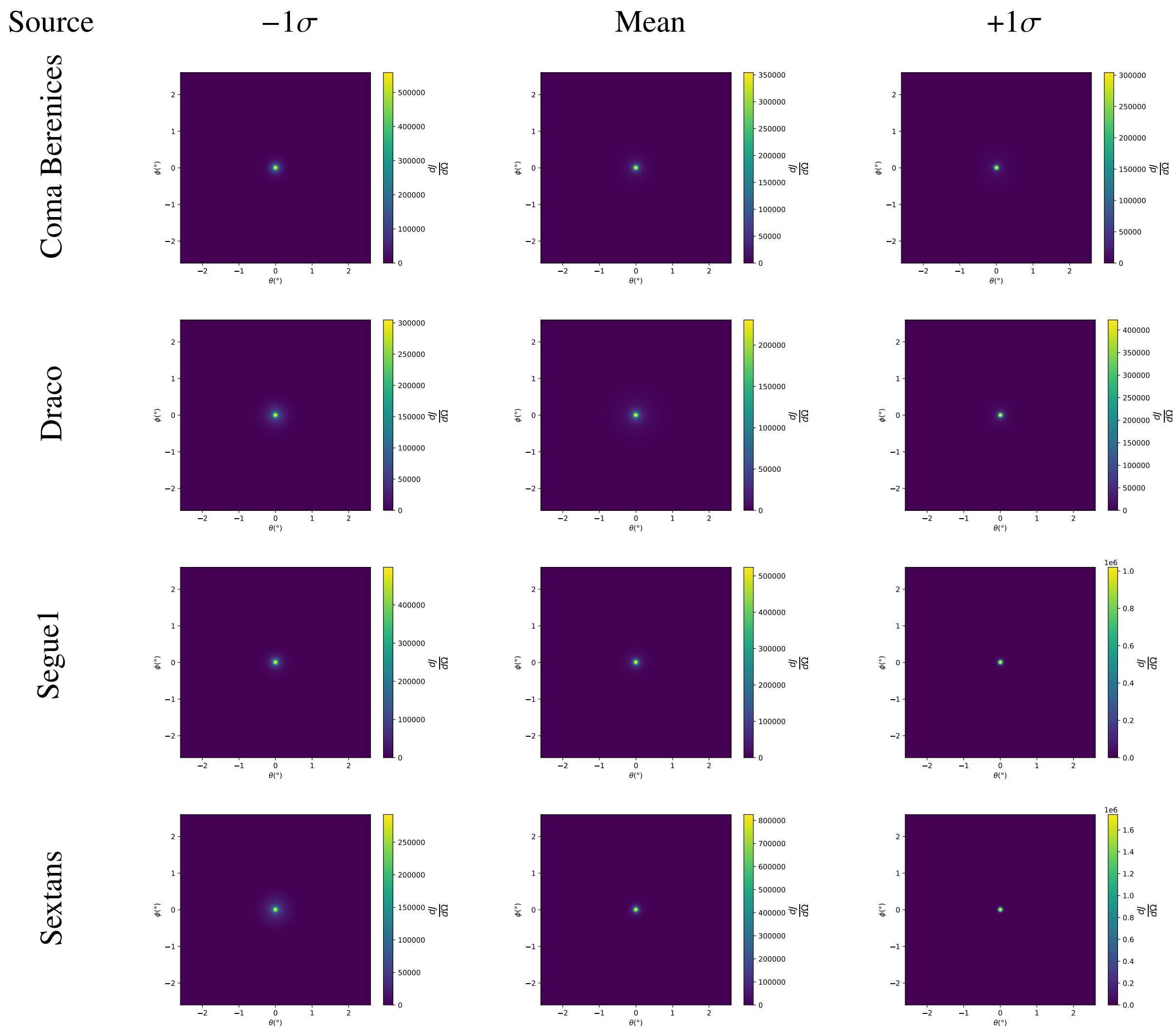

Figure 7.3 $\frac{dJ}{d\Omega}$ maps for Coma Berenices, Draco, Segue1, and Sextans. Columns are divided for the $\pm 1\sigma$ uncertainties in $dJ/d\Omega$ around the mean value from $\mathcal{LS}$ [65]. Origin is centered on the specific dwarf spheroidal galaxies (dSph). θ and ϕ axes are the angular separation from the center of the dwarf

model used for gamma-ray spectra from DM annihilation was from the PPPC [44] which missed important considerations relevant for the neutrino sector. HDM is used to account for this shortfall [64]. HDM also models DM to the Planck scale which permits HAWC to probe PeV scale DM. For this study, we sample DM masses: 1 TeV - 10 PeV with 6 mass bins per decade in DM mass. In the case of line spectra ($\chi\chi \rightarrow \gamma\gamma$, or ZZ), we double the mass binning to 12 DM mass bins per decade in DM mass. A larger source catalog is used that uses a Navarro–Frenk–White (NFW) spatial DM distribution from $\mathcal{LS}$ [65]. Because NFW has fewer parameters than what is used for $\mathcal{GS}$, $\mathcal{LS}$ is able to fit ultra-faint dwarves, expanding the number of sources available for DM searches. Finally, the gamma-ray ray dataset is much larger. The study performed here analyzes 2565 days of data compared to 1017 days analyzed in chapter 6.

7.4 Likelihood Methods

These are identical to Section 6.4.1 and not additional changes are made to the likelihood. Bins in this analysis are expanded to include HAWC's NN energy estimator.

7.5 Computational Methods: Multithreading

Previously, as in Section 6.3, the likelihood was minimized for one model at a time. One model in this case representing a DM annihilation channel, DM mass, and dSph. In an effort to conserve human and CPU time, jobs submitted for high performance computing contained a list of DM masses to iterate over for likelihood fitting. Jobs were then trivially parallelized for each permutation of the two lists: `CHANS` (SM annihilation channel) and `SOURCES` (dSph spatial templates). The lists for `CHANS` and `SOURCES` are found in Section 7.3.1 and Table 7.1, respectively. Initially, 11 DM mass bins were serially sampled for one job defined by a [SM channel, dSph] set. Computing the likelihoods would take between 1.5 to 2 hrs, stocastically, for a job. We expect to compute likelihoods for data and 300 Poisson background trials. The estimated CPU time based on the above for all SM annihilation channels (17) and 25 sources (all $\mathcal{LS}$ sources withing HAWC's field of view) amounted to $127,925$ jobs. In total, $1,407,175$ likelihood fits and profiles would be computed for the 11 mass bins we wished to study. The estimated CPU time ranged between 10k CPU days - 8k CPU days. Human time is more challenging to estimate as job allocation is stocastic and highly dependant on what other users are submitting, yet it is unlikely that all jobs would run simultaneously. Therefore we can expect human time to be about as long as was seen in chapter 6 which was on the order of months to fully compute on a smaller analysis. A visual aid to describe how jobs were organized is provided in Figure 7.4.

The computational needs for this next generation DM analysis are extreme and is unlike other analyses performed on HAWC. It became clear that there was a lot to gain from optimzing how the likelihoods are computed. This section discusses how multi-threading was applied to solve and

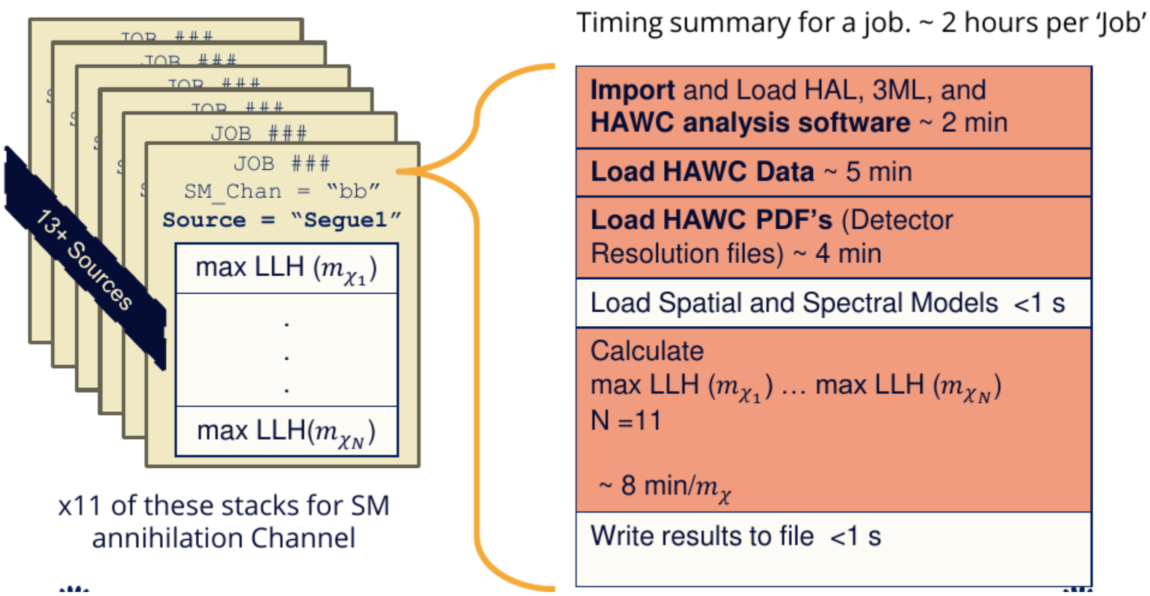

Figure 7.4 Infographic on how jobs and DM computation was organized in Section 6.3. Jobs were built for each permutation of `CHANS` and `SOURCES` shown by the left block in the figure. Each job, which took on the order 2 hrs to compute, had the following work flow: 1. Import HAWC analysis software, 2 min to run. 2. Load HAWC count maps, 5 min to run. 3. Load HAWC energy and spatial resolutions, 4 min. 5. Load DM spatial source templates and spectral models, less than 1 s. 6. Perform likelihood fit on data and model, about 8 min per DM mass. 7. Write results to file, less than 1s.

reduce HAWC's computing of likelihoods for large parameter spaces like in DM searches.

7.5.1 Relevant Foundational Information

The profiling of the likelihood for HAWC is done via gradient descent where the nomarlization of Equation (6.1) (linearly correlated with $\langle \sigma v \rangle$) is rescaled in the descent. Additionaly, we sample the likelihood space for a defined list of $\langle \sigma v \rangle$'s described in Section 6.4.2. The time to compute these values is not predictable or consistent because many variables can change across the full model-space. comprehensively, these variables are:

- m_χ : DM rest mass
- `CHAN` : DM SM annihilation channel.
- `SOURCE` : dSph within HAWC's field of view. This involves a spatial template AND coordinate in HAWC data.

- $\langle \sigma v \rangle$: Effectevly the flux normalization and free parameter in the likelihood fit.

Therefore, we develop an asyncronous, functional-parallel coding pattern. Asyncronous meaning that the instructions and computing within a function are independent and permitted to be out of sync with sibling computations. Functional-parallel meaning that instructions are the subject of parrallelization rather than threading the likelihood computation. This is close to trivial parametrization seen in Figure 7.4 except that we seek to consolidate the loading stages (software, data, and detector resolution loading). Reducing the total instances of loading stages and distributing access to the reduced loads across multiple asyncronous threads is expected to reduce serial processing time and the overhead implicit to each job in addition to saving human time.

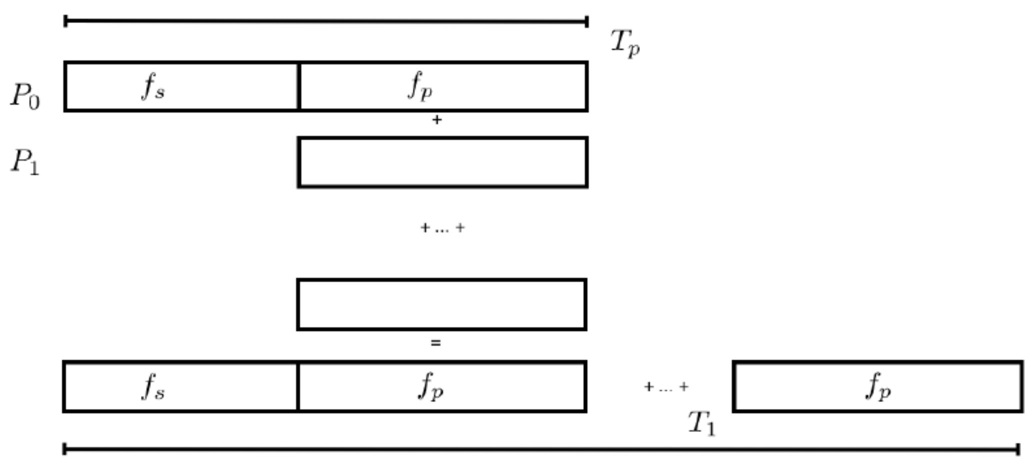

Figure 7.5 Graphic of Gustafson parallel coding pattern. f_s is the fraction of a program, in time, spent on serial computation. f_p is the fraction of computing time that is parallelizable. T_p is the total time for a parallel program to run. T_1 is the total time for a parallel program to run if only 1 processor is allocated. P_N is the N-th processor where it's row is the computation the processor performs. The Gustafson pattern is most similar to what is implemented for this analysis. Figure is pulled from [67].

We need a way to measure and compare the expected speedup and efficiency gain for this asyncronous coding pattern. I pull inspiration for timing measurement from [67] and use *Amdahl's law with hybrid programming*. Hybrid programming meaning that the computation is a mix of distributed and shared memory programming. If we assume the code is fully parallelizable over p processors and c threads, the ideal speedup is simply pc and ideal run-time is $T_1/(pc)$. T_1 is the total time for a parallel program to run if only 1 processor is allocated. However, the coding pattern contains some amount of unavoidable serial computation, as shown in Figure 7.5. In our case, the run time is estimated to be

$$T_{p,c} = \frac{T_1}{pc}\left(1 + F_s(c-1)\right). \tag{7.4}$$

F_s is the fraction of CPU time dedicated to serial computation. The expected speedup is

$$S_{p,c} \equiv \frac{T_1}{T_{p,c}} = \frac{pc}{1 + F_s(c-1)}. \tag{7.5}$$

From Equation (7.5), we can see that the speed up scales with p/F_s. We are free to minimize F_s asymptotically by enlarging the total models that are submitted to the thread pool, thereby shrinking the CPU fraction dedicated to serial operation. We are also free to define exactly how many threads and processors we utilize, yet eventually hit a hard cap at the hardware available on our computing cluster. HAWC uses Intel Xeon processors with 48 cores and 96 threads. This means when N-threads (c) are defined, N mod 2 cores (p) are needed. We see that a successful code scales well as the expected speedup is inversely correlated with F_s. As the total number of models sampled grows, the speedup will also.

7.5.2 Implementation

The multithreaded code was written in Python3 and is documented in the `dark_matter_hawc` repository within the script named `mpu_analysis.py`. A version of the script as of April 25 TODO: make sure to update on this dateis also provided in Section B.1 It has many dependancies including the HAWC analysis software. Figure 7.6 displays the workflow of a job with 3 threads. Within a job, `SOURCE` is kept fixedh . `CHAN(S)` remains 17 elements long. More m_χ are sampled from 11 bins up to 49 (for $\gamma\gamma$ and ZZ) and 25 (for remaining `CHANS`) which amounts to 12 or 6 mass bins per decade. The DM mass, m_χ, and SM annihilation channels, `CHANS`, are permuted into a 473 element list which is split evenly across N threads where N ranges between 5 - 16. Within a thread, for each m_χ-`CHAN` tuple, 1001 $\langle\sigma v\rangle$ values are sampled in the likelihood, and the value of $\langle\sigma v\rangle$ that maximizes the likelihood is found. Although rare, fits that failed are handled on a case by case basis.

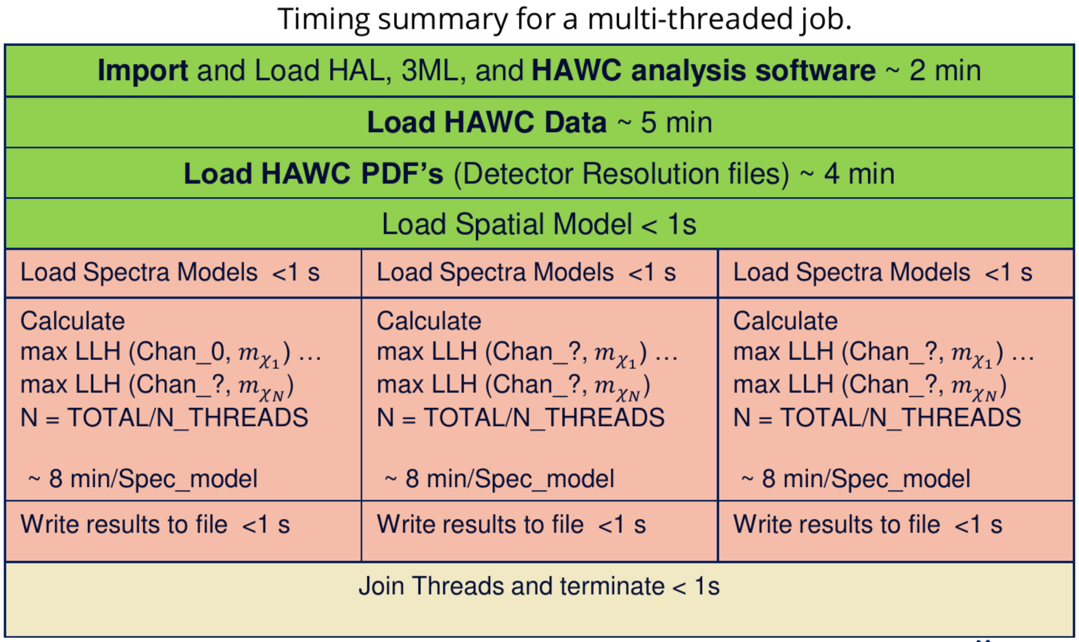

Figure 7.6 Task chart for one multi-threaded job developed for this project. Green blocks indicate a shared resource across the threads AND computation performed serially. Red blocks indicate functional parallel processing within each thread. 3 threads are represented here, yet many more can be employed during the full analysis. Jobs are defined by the `SOURCE` as these require unique maps to be loaded into the likelihood estimator. The m_χ, `CHAN`, and $\langle\sigma v\rangle$ variables are entered into the thread pool and allocated as evenly as possible across the threads.

7.5.3 Performance

	$T_{p,c}$ (hr:min:s)			
M Tasks	$T_{1,1}$	$T_{1,2}$	$T_{1,8}$	$T_{1,16}$
50	1:40:37.5	0:52:43.7	0:19:13.8	0:13:44.0
74	2:22:30.0	1:15::00.6	0:25:21.3	0:15:49.8
100	(3:07:51.9)			0:20:01.4
200	(6:02:20.6)	-		
473	(13:58:40.3)	-		1:09:42.9

Table 7.2 Timing summaries for analyses for serial and multithreaded processes. M tasks is the number of functional-parallel tasks ran for the computation. $T_{p,c}$ is a single run time in hours:minutes:seconds for runs utilizing p nodes and c threads. Runs are run interactively on the same computer to maximize consistency. Empty entries are indicated with '-'. $(\cdot)$ entries are estimated entries extrapolated from data earlier in the column.

We see a tremendous reduction to human time waiting for our dSph analyses to run. Table 7.2 shows the timing summaries for analyses of different sizes and thread counts. Additionaly, the efficiency gained when consolidating the serial loading of data is also apparent in our ability to study many more tasks in about the same amount of wall time as a smaller serial computation. Trials represented in the table were run on an AMD Opteron® processor 6344 with 48 cores, 2 threads per core; 2.6 GHz clock. This is not the same architecture used for analysis on the computing cluster however they are similar enough that results shown here are reasonably representative of computing on the HAWC computing cluster. I use the Tab. 7.2 for the inferences and conclusions in the following paragraphs.

First, we want to find T_s, the time of serial computation. From Fig. 7.5, the timing for our coding pattern can be written as

$$T_s + Mt_p = T_{1,1}^{M}. \tag{7.6}$$

M is the number of functional-parallel tasks (represented as column 1 of Tab. 7.2), and t_p is the average time to complete a single parallel task. $T_{1,1}^{M}$ is the total time for a parallel program to run if only 1 processor is allocated for M parallel task. With two runs of different M ($M1$ and $M2$), we can use a system of equations to derive

$$T_s = T_{1,1}^{M1} - M1\left(\frac{T_{1,1}^{M1} - T_{1,1}^{M2}}{M1 - M2}\right). \tag{7.7}$$

We also extract t_p using the same methods:

$$t_p = \frac{T_{1,1}^{M1} - T_{1,1}^{M2}}{M1 - M2}. \tag{7.8}$$

From Tab. 7.2, we set $M1 = 50$ and $M2 = 74$ and take their corresponding $T_{1,1}$ from the table to calculate T_s and t_p.

$$T_s = 803.1\text{s and } t_p = 104.6\text{s} \tag{7.9}$$

Now, we have specific estimation for the fraction of serial computing time, F_s:

$$F_s = \frac{803.1}{803.1 + 104.6 \cdot M}. \tag{7.10}$$

The maximum M for this study is 473 which evaluates Eq. (7.10): $F_s = 0.016$ or 1.6% of computing time. Table 7.3 shows the resulting speedups.

We see a speedup that exceeds expectations from Eq. (7.5) for real trail runs. TODO: reflect on results when the tables are totally filled in.We also see that there are diminishing returns as

	$S_{p,c}$		
M Tasks	$S_{1,2}$	$S_{1,8}$	$T_{1,16}$
50	1.90 [1.76]	5.23 [4.14]	6.35 [5.34]
74	1.90 [1.83]	5.62 [4.82]	9.00 [6.64]
100			
200	-		
473	-		1:09:42.9

Table 7.3 Speed up summaries for analyses for serial and multithreaded processes. M tasks is the number of functional-parallel tasks ran for the computation. $S_{p,c}$ is a single speedup comparison for runs utilizing p nodes and c threads. $[\cdot]$ are the estimated speedups calculated from Tab. 7.2, Eq. (7.10), and Eq. (7.5). Empty entries are indicated with '-'.

the number of threads increases. For small jobs with large c, both the expected and observed speedup are significantly smaller than c. One thing not considered in Eq. (7.5) is the time incurred via communication latency. Communication latency increases with the number of threads and contributes to diminishing returns. Therefor, these results are not conclusive. Each entry in Tab. 7.2 represent only one run of the script and therefore the data are not precise and lacks the full scope of timing costs. Yet, they do give us a good idea of what HAWC gains in multithreading analysis software. We see very clearly that there is a lot to gain, and this new coding pattern will expand HAWC's analysis capabilities.

7.6 Analysis Results

Figure 7.7 TODO: combined 95 results of new duck. See if we can include Draco[NEEDS A SOURCE][FACT CHECK THIS]

Figure 7.8 TODO: combined 95 results. There will definitely be 2[NEEDS A SOURCE][FACT CHECK THIS]

Figure 7.9 TODO: TS of analysis of results. See if we can include Draco[NEEDS A SOURCE][FACT CHECK THIS]

Figure 7.10 TODO: TS of analysis of results. There will definitely be 2[NEEDS A SOURCE][FACT CHECK THIS]

CHAPTER 8

HEAVY DARK MATTER ANNIHILATION SEARCH WITH ICECUBE'S NORTH SKY TRACK DATA

CHAPTER 9

1313 **NU DUCK**

APPENDIX A

MULTI-EXPERIMENT SUPPLEMENTARY FIGURES

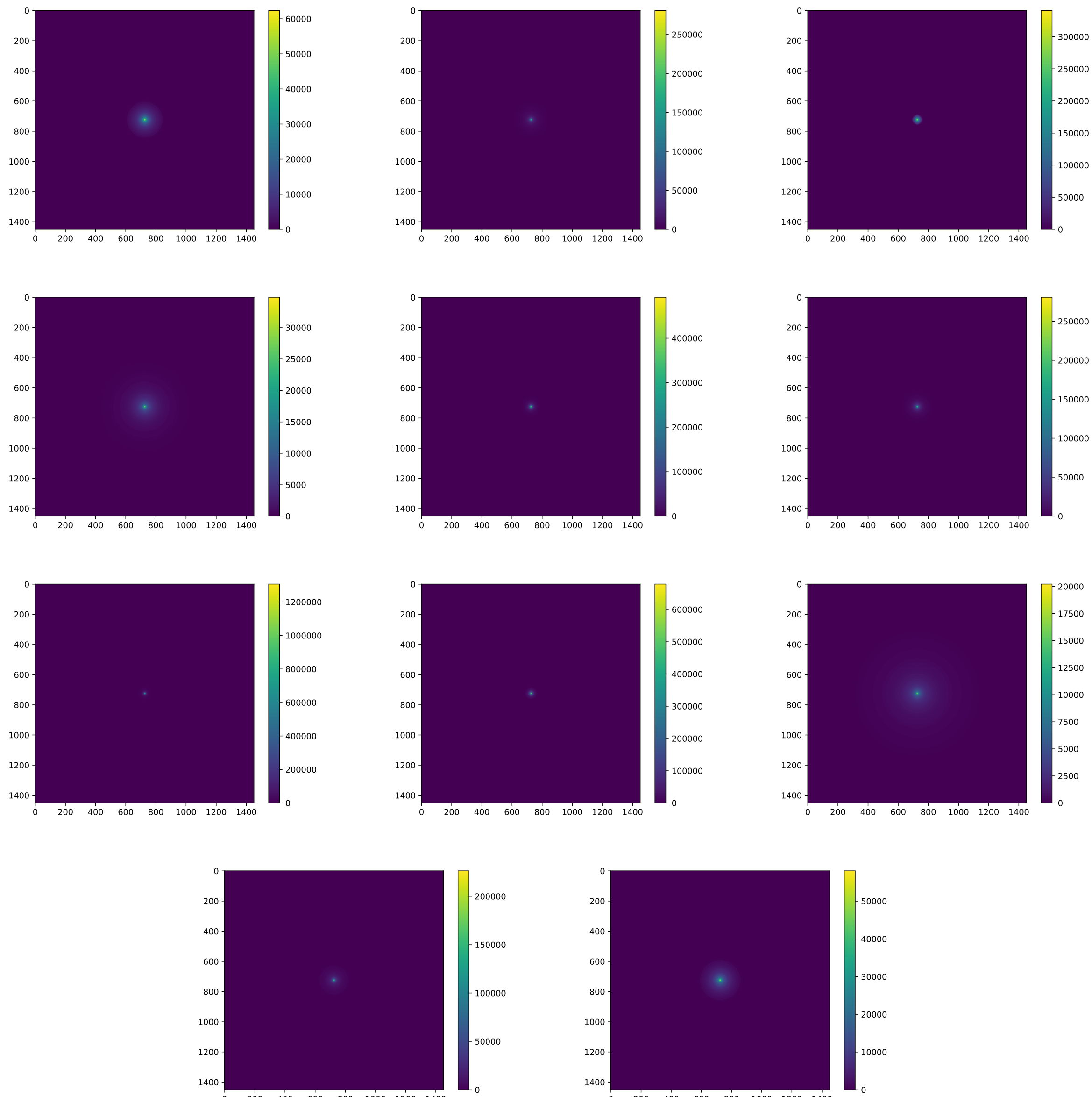

Figure A.1 Sister figure to Figure 6.3. Sources in the first row from left to right: Bootes I, Canes Venatici I, II. In second row: Draco, Hercules, Leo I. In the first row: Leo II, Leo IV, Sextans. In the final row: Ursa Major I, Ursa Major II.

APPENDIX B

MULTITHREADING SUPPLEMENTARY FIGURES

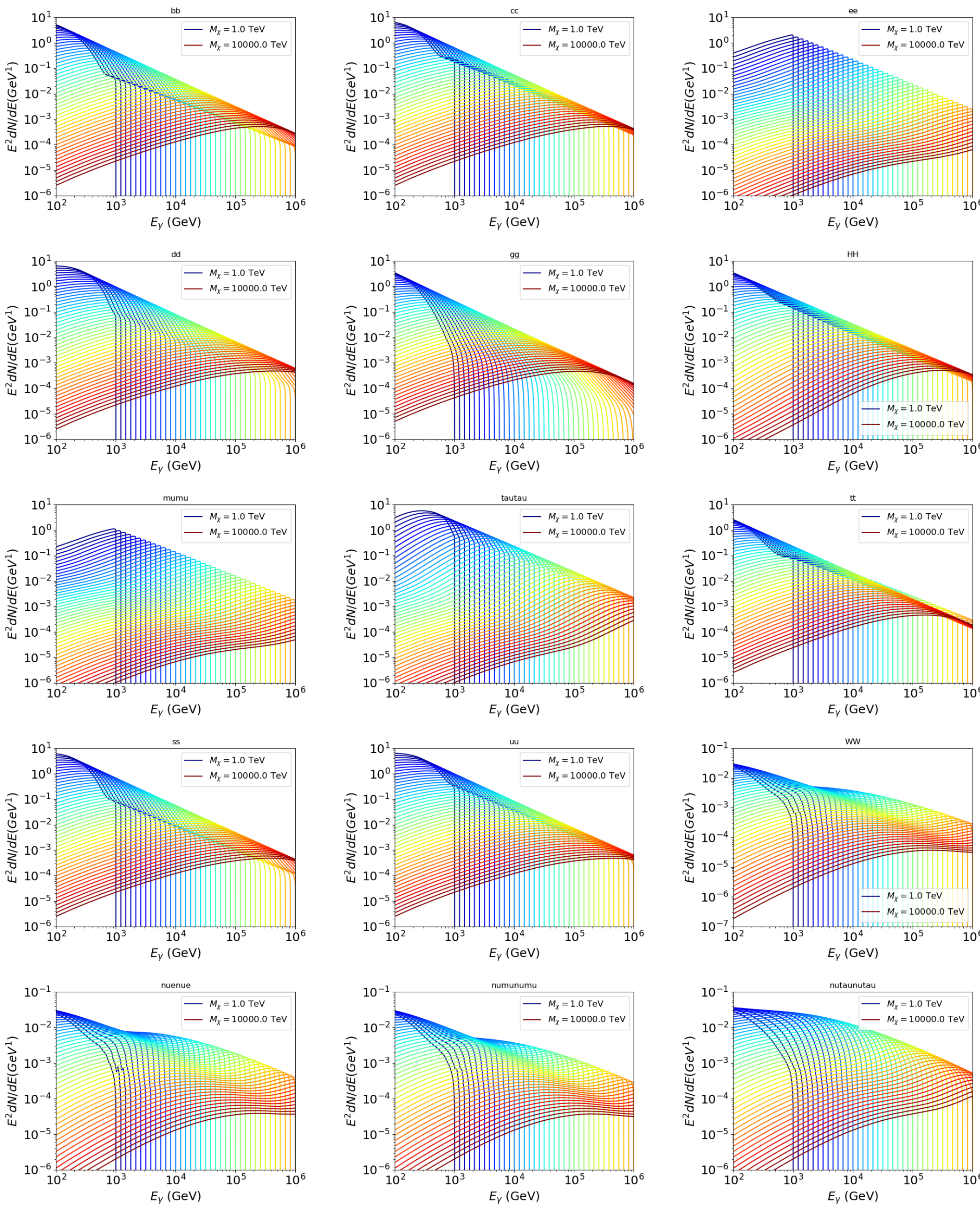

Figure B.1 Sister figure to Figure 7.2 for remaining SM primary annihilation channels studied for this thesis. These did not require any post generation smoothing and so are directly pulled from [64] with a binning scheme most helpful for a HAWC analysis.

B.1 mpu_analysis.py

```python
import warnings
with warnings.catch_warnings():
    warnings.simplefilter("ignore")
# Python base libraries
import os
import sys
import time
# Import general libraries with namespace
import matplotlib
# Necessary for computing on cluster
matplotlib.use("agg")
import numpy as np
import multiprocessing as mp
# Import HAWC software
sys.path.insert(1, os.path.join(os.environ['HOME'], 'hawc_software', 'threeml-analysis-scripts', 'fitModel'))
from analysis_modules import *
from threeML import *
from hawc_hal import HAL, HealpixConeROI
from threeML.minimizer.minimization import FitFailed
# Import Dark  Matter HAWC Libraries
import analysis_utils as au
import spectra as spec
import sources as srcs

#* READ ONLY PATHS This block will change eventually
MASS_LIST = './plotting/studies/nd/masses.txt'
CHAN_LIST = './plotting/studies/nd/chans.txt'

#* WRITE PATHS, default location is to scratch
OUT_PATH = os.path.join(os.environ["SCRATCH"], os.environ["USER"], 'New_duck')
```

```
print('Our out path is going to be {}'.format(OUT_PATH))

# Define parallel Function. Can also be run serially
def some_mass_fit(sigVs, datalist, shape, dSph, jfactor, mass_chan,
                  progress=None, log_file='', queue=None, i_job=0):

    if progress is None:
        progress = [0]
    else: # Create log files for each thread
        log_file = log_file.replace('.log', '_ThreadNo_')
        log_file = log_file + str(i_job) + ".log"
        sys.stdout = open(log_file, "w")

    fits = []

    try:
        for m_c in mass_chan:
            print(f'Mass chan tuple: {m_c}')
            mass = int(m_c[0])
            ch = m_c[1]
            # Build path to output files
            outPath = os.path.join(OUT_PATH, ch, dSph)
            au.ut.ensure_dir(outPath)

            if progress[i_job] < 0:
            # If the master gets a Keyboard interrupt, commit suicide.
                break

            ### Start Model Building for DM mass and SM channel ####
            spectrum = spec.DM_models.HDMSpectra()
            spectrum.set_channel(ch)

            myDwarf = ExtendedSource(dSph,spatial_shape=shape,
```

```
                                 spectral_shape=spectrum)

        spectrum.J = jfactor * u.GeV**2 / u.cm**5
        spectrum.sigmav = 1e-24 * u.cm**3 / u.s
        spectrum.set_dm_mass(mass * u.GeV)

        spectrum.sigmav.bounds = (1e-30,1e-12)
        model = Model(myDwarf)
        ### End model Building ####

        jl = JointLikelihood(model,datalist,verbose=False)

        try:
            result, lhdf = jl.fit(compute_covariance=False)
            ts = -2.*(jl.minus_log_like_profile(1e-30) - jl._current_minimum)
            # Also profile the LLH vs sv
            ll = jl.get_contours(spectrum.sigmav, sigVs[0],
                                 sigVs[-1], len(sigVs),
                                 progress=False, log=['False'])

            sigv_ul = au.ut.calc_95_from_profile(ll[0], ll[2])
            # Write results to file
            outFileLL = outPath+f"/LL_{dSph}_{ch}_mass{int(mass)}_GD.txt"
            np.savetxt(outFileLL, (sigVs, ll[2]),
                       delimiter='\t', header='sigV\tLL\n')

            with open(outPath+f"/results_{dSph}_{ch}_mass{int(mass)}_GD.txt", "w") as results_file:
                results_file.write("mDM [GeV]\tsigV_95\tTS\tsigV_B.F.\n")

                results_file.write("%i\t%.5E\t%.5E\t%.5E"%(mass, sigv_ul,
                                    ts, result.value[0]))
```

```
                # End write to file
            except FitFailed: # Don't kill all threads if a fit fails
                print("Fit failed. Go back and calculate this spectral model later")
                fits.append((ch, mass, -1, -1))
                with open(log_file+'.fail', 'w') as f_file:
                    f_file.write(f'{ch}, {mass}\n')

                progress[i_job] += 1
                matplotlib.pyplot.close() # Prevent leaky memory

            fits.append((ch, mass, result.value[0], ts))
            progress[i_job] += 1
            matplotlib.pyplot.close()
    except KeyboardInterrupt:
        progress[i_job] = -1

    fits = np.array(fits)
    if queue is None:
        return fits
    else:
        queue.put((i_job, fits))

def main(args):
    masses = np.loadtxt(MASS_LIST, dtype=int)
    chans = np.loadtxt(CHAN_LIST, delimiter=',', dtype=str)
    mass_chan = au.ut.permute_lists(chans, masses)

    print(f"DM masses for this study are: {masses}")
    print(f"SM Channels for this study are XX -> {chans}")
    print(mass_chan)

    # extract information from input argument
```

```
    dSph = args.dSph
    data_mngr = au.ut.Data_Selector('P5_NN_2D')
    dm_profile = srcs.Spatial_DM(args.catalog, dSph, args.sigma, args.decay)

    ### Extract Source Information ###
    if dm_profile.get_dec() < -22.0 or dm_profile.get_dec() > 62.0:
        raise ValueError("HAWC can't see this source D: Exitting now...")

    print(f'{dSph} information')
    print(f'jfac: {dm_profile.get_factor()}\tRA: {dm_profile.get_ra()}\tDec: {dm_profile.get_dec()}\n')

    shape = SpatialTemplate_2D(fits_file=dm_profile.get_src_fits())
    ### Finish Extract Source Information ###

    ### LOAD HAWC DATA ###
    roi = HealpixConeROI(data_radius=2.0, model_radius=8.0,
                         ra=dm_profile.get_ra(), dec=dm_profile.get_dec())
    bins = choose_bins.analysis_bins(args, dec=dm_profile.get_dec())

    hawc = HAL(dSph, data_mngr.get_datmap(), data_mngr.get_detres(), roi)
    hawc.set_active_measurements(bin_list=bins)
    datalist = DataList(hawc)
    ### FINISH LOAD HAWC DATA ###

    # set up SigV sampling. This sample is somewhat standardized
    sigVs = np.logspace(-28,-18, 1001, endpoint=True) # NOTE This will change whith HDM

    if args.n_threads == 1:
        # No need to start || programming just iterate over the masses
        kw_arg = dict(sigVs=sigVs, datalist=datalist, shape=shape, dSph=dSph,
                      jfactor=dm_profile.get_factor(), mass_chan=mass_chan,
```

```
                    log_file=args.log)
        some_mass_fit(**kw_arg)
    else:
        # I Really want to suppress TQMD output
        from tqdm import tqdm
        from functools import partialmethod
        tqdm.__init__ = partialmethod(tqdm.__init__, disable=True)

        x = np.array_split(mass_chan, args.n_threads)
        n_jobs = len(x)

        print("Thread jobs summary by mass and SM channel")
        for xi in x:
            print(f'{xi}')

        queue = mp.Queue()
        progress = mp.Array('i', np.zeros(n_jobs, dtype=int))

        # Define task pool that will be split amongsts threads
        kw_args = [dict(sigVs=sigVs, datalist=datalist, shape=shape,
                        dSph=dSph, jfactor=dm_profile.get_factor(),
                        mass_chan=mass_chan, progress=progress,
                        queue=queue, i_job=i, log_file=args.log)
                   for i, mass_chan in enumerate(x)]

        # Define each process
        procs = [mp.Process(target=some_mass_fit, kwargs=kw_args[i]) \
                 for i in range(n_jobs)]

        ### Start MASTER Thread only code block ###
        # Begin running all child threads
        for proc in procs: proc.start()

```

```
        try:
            # In this case, the master does nothing except monitor progress of the threads
            # In an ideal world, the master thread also does some computation.
            n_complete = np.sum(progress)
            while_count = 0

            while n_complete < len(mass_chan):

                if np.any(np.asarray(progress) < 0):
                    # This was no threads are stranded when killing the script
                    raise KeyboardInterrupt()
                if while_count%1000 == 0:
                    print(f"{np.sum(progress)} of {len(mass_chan)} finished")

                n_complete = np.sum(progress)
                time.sleep(.25)
                while_count += 1

        except KeyboardInterrupt:
        # signal to jobs that it's time to stop
            for i in range(n_jobs):
                progress[i] = -2
                print('\nKeyboardInterrupt: terminating early.')
        ### End MASTER Thread only code block ###

        fitss = [queue.get() for proc in procs]
        print(fitss)
        print(f'Thread statuses: {progress[:]}')

    # putting results in a file

    print("QUACK! All Done!")
```

```python


if __name__ == '__main__':
    import argparse

    p = argparse.ArgumentParser(description="Run a DM annihilation analysis on a dwarf spheroidal for a specific SM channel for DM masses [1 TeV to 10 PeV]")

    # Dwarf spatial modeling arguements
    p.add_argument("-ds", "--dSph", type=str,
                    help="dwarf spheroidal galaxy to be studied", required=True)
    p.add_argument("-cat", "--catalog", type=str, choices=['GS15', 'LS20'],
                   default='LS20', help="source catalog used")
    p.add_argument("-sig", "--sigma", type=int, choices=[-1, 0, 1], default=0,
                   help="Spatial model uncertainty. 0 corresponds to the median. +/-1 correspond to the +/1sigma uncertainty respectively.")

    # Arguements for the energy estimators
    p.add_argument("-e", "--estimator", type=str,
                   choices=['P5_NHIT', 'P5_NN_2D'],
                   default="P5_NN_2D", required=False,
                   help="The energy estimator choice. Options are: P5_NHIT, P5_NN_2D. GP not supported (yet).")
    p.add_argument("--use-bins", default=None, nargs="*",
                    help="Bins to  use for the analysis", dest="use_bins")
    p.add_argument('--select_bins_by_energy', default=None, nargs="*",
                   help="Does nothing. May fill in later once better understood")
    p.add_argument('--select_bins_by_fhit', default=None, nargs="*",
                   help="Also does nothing see above")
    p.add_argument( '-ex', "--exclude", default=None, nargs="*",
```

```
                    help="Exclude Bins", dest="exclude")

    # Computing and logging arguements.
    p.add_argument('-nt', '--n_threads', type=int, default=1,
                     help='Maximum number of threads spawned by script. Default is 4')
    p.add_argument('-log', '--log', type=str, required=True,
                     help='Name for log files. Especially needed for threads')

    p.add_argument('--decay', action="store_true",
                    help='Set spectral DM hypothesis to decay')

    args = p.parse_args()
    print(args.decay)
    if args.exclude is None: # default exclude bins 0 and 1
        args.exclude = ['B0C0Ea', 'B0C0Eb', 'B0C0Ec', 'B0C0Ed', 'B0C0Ee']

    if args.decay: OUT_PATH += '_dec'
    else: OUT_PATH += '_ann'

    OUT_PATH = OUT_PATH + '_' + args.catalog
    if args.sigma != 0: OUT_PATH += f'_{args.sigma}sig'

    main(args)
```

BIBLIOGRAPHY

[1] Anne M. Green. "Dark matter in astrophysics/cosmology". In: *SciPost Phys. Lect. Notes* (2022), p. 37. DOI: 10.21468/SciPostPhysLectNotes.37. URL: https://scipost.org/10.21468/SciPostPhysLectNotes.37.

[2] Bing-Lin Young. "A survey of dark matter and related topics in cosmology". In: *Frontiers of Physics* 12 (Oct. 2016). DOI: https://doi.org/10.1007/s11467-016-0583-4. URL: https://doi.org/10.1007/s11467-016-0583-4.

[3] Gianfranco Bertone, Dan Hooper, and Joseph Silk. "Particle dark matter: evidence, candidates and constraints". In: *Physics Reports* 405.5 (2005), pp. 279–390. ISSN: 0370-1573. DOI: https://doi.org/10.1016/j.physrep.2004.08.031. URL: https://www.sciencedirect.com/science/article/pii/S0370157304003515.

[4] Gianfranco Bertone and Dan Hooper. "History of dark matter". In: *Rev. Mod. Phys.* 90 (4 Aug. 2018), p. 045002. DOI: 10.1103/RevModPhys.90.045002. URL: https://link.aps.org/doi/10.1103/RevModPhys.90.045002.

[5] Fritz Zwicky. "The Redshift of Extragalactic Nebulae". In: *Helvetica Physica* Acta 6. (1933), pp. 110–127. DOI: 10.5169/seals-110267.

[6] Vera C. Rubin and Jr. Ford W. Kent. "Rotation of the Andromeda Nebula from a Spectroscopic Survey of Emission Regions". In: *ApJ* 159 (Feb. 1970), p. 379. DOI: 10.1086/150317.

[7] K. G. Begeman, A. H. Broeils, and R. H. Sanders. "Extended rotation curves of spiral galaxies: dark haloes and modified dynamics". In: *Monthly Notices of the Royal Astronomical Society* 249.3 (Apr. 1991), pp. 523–537. ISSN: 0035-8711. DOI: 10.1093/mnras/249.3.523. eprint: https://academic.oup.com/mnras/article-pdf/249/3/523/18160929/mnras249-0523.pdf. URL: https://doi.org/10.1093/mnras/249.3.523.

[8] *Different types of gravitational lenses*. website. Feb. 2004. URL: https://esahubble.org/images/heic0404b/.

[9] Douglas Clowe et al. "A Direct Empirical Proof of the Existence of Dark Matter". In: *apjl* 648.2 (Sept. 2006), pp. L109–L113. DOI: 10.1086/508162. arXiv: astro-ph/0608407 [astro-ph].

[10] Planck Collaboration and N. et. al. Aghanim. "Planck 2018 results I. Overview and the cosmological legacy of Planck". In: *A&A* 641 (2020). DOI: 10.1051/0004-6361/201833880. URL: https://doi.org/10.1051/0004-6361/201833880.

[11] Wayne Hu. *Matter Density Animation*. web. 2024. URL: http://background.uchicago.edu/~whu/animbut/anim2.html.

[12] Wenlong Yuan et al. “A First Look at Cepheids in a Type Ia Supernova Host with JWST”. in: *The Astrophysical Journal Letters* 940.1 (Nov. 2022). DOI: 10.3847/2041-8213/ac9b27. URL: https://dx.doi.org/10.3847/2041-8213/ac9b27.

[13] Wendy L. Freedman. “Measurements of the Hubble Constant: Tensions in Perspective”. In: *The Astrophysical Journal* 919.1 (Sept. 2021), p. 16. DOI: 10.3847/1538-4357/ac0e95. URL: https://dx.doi.org/10.3847/1538-4357/ac0e95.

[14] Jodi Cooley. “Dark Matter direct detection of classical WIMPs”. In: *SciPost Phys. Lect. Notes* (2022), p. 55. DOI: 10.21468/SciPostPhysLectNotes.55. URL: https://scipost.org/10.21468/SciPostPhysLectNotes.55.

[15] “Search for new phenomena in events with an energetic jet and missing transverse momentum in pp collisions at $\sqrt{s} = 13$ TeV with the ATLAS detector”. In: *Phys. Rev. D* 103 (11 July 2021), p. 112006. DOI: 10.1103/PhysRevD.103.112006. URL: https://link.aps.org/doi/10.1103/PhysRevD.103.112006.

[16] *Jetting into the dark side: a precision search for dark matter*. website. July 2020. URL: https://atlas.cern/updates/briefing/precision-search-dark-matter.

[17] Celine Armand et. al. “Combined dark matter searches towards dwarf spheroidal galaxies with Fermi-LAT, HAWC, H.E.S.S., MAGIC, and VERITAS”. in: *Proceedings of Science*. Vol. 395. Mar. 2022. DOI: https://doi.org/10.22323/1.395.0528.

[18] Tracy R. Slatyer. “Les Houches Lectures on Indirect Detection of Dark Matter”. In: *SciPost Phys. Lect. Notes* (2022), p. 53. DOI: 10.21468/SciPostPhysLectNotes.53. URL: https://scipost.org/10.21468/SciPostPhysLectNotes.53.

[19] Christian W Bauer, Nicholas L. Rodd, and Bryan R. Webber. “Dark matter spectra from the electroweak to the Planck scale”. In: *Journal of High Energy Physics* 2021.1029-8479 (June 2021). DOI: https://doi.org/10.1007/JHEP06(2021)121.

[20] Riccardo Catena and Piero Ullio. “A novel determination of the local dark matter density”. In: *Journal of Cosmology and Astroparticle Physics* 2010.08 (Aug. 2010), p. 004. DOI: 10.1088/1475-7516/2010/08/004. URL: https://dx.doi.org/10.1088/1475-7516/2010/08/004.

[21] B. P. Abbott et al. “Observation of Gravitational Waves from a Binary Black Hole Merger”. In: *Phys. Rev. Lett.* 116 (6 Feb. 2016), p. 061102. DOI: 10.1103/PhysRevLett.116.061102. URL: https://link.aps.org/doi/10.1103/PhysRevLett.116.061102.

[22] R. Abbasi et. al. “Observation of high-energy neutrinos from the Galactic plane”. In: *Science* 380.6652 (June 2023), pp. 1338–1343.

[23] NASA Goddard Space Flight Center. *Fermi’s 12-year view of the gamma-ray sky*. website.

2022. URL: https://svs.gsfc.nasa.gov/14090.

[24] Marco Cirelli et al. "PPPC 4 DM ID: a poor particle physicist cookbook for dark matter indirect detection". In: *Journal of Cosmology and Astroparticle Physics* 2011.03 (Mar. 2011), p. 051. DOI: 10.1088/1475-7516/2011/03/051. URL: https://dx.doi.org/10.1088/1475-7516/2011/03/051.

[25] Javier Rico. "Gamma-Ray Dark Matter Searches in Milky Way Satellites—A Comparative Review of Data Analysis Methods and Current Results". In: *Galaxies* 8.1 (Mar. 2020), p. 25. DOI: 10.3390/galaxies8010025. arXiv: 2003.13482 [astro-ph.HE].

[26] W. B. Atwood et al. "The Large Area Telescope on the Fermi Gamma-Ray Space Telescope Mission". In: *apj* 697.2 (June 2009), pp. 1071–1102. DOI: 10.1088/0004-637X/697/2/1071. arXiv: 0902.1089 [astro-ph.IM].

[27] M. Ackermann et al. "Searching for Dark Matter Annihilation from Milky Way Dwarf Spheroidal Galaxies with Six Years of Fermi Large Area Telescope Data". In: *prl* 115.23, 231301 (Dec. 2015), p. 231301. DOI: 10.1103/PhysRevLett.115.231301. arXiv: 1503.02641 [astro-ph.HE].

[28] Mattia Di Mauro, Martin Stref, and Francesca Calore. "Investigating the effect of Milky Way dwarf spheroidal galaxies extension on dark matter searches with Fermi-LAT data". In: *Phys. Rev. D* 106 (12 Dec. 2022), p. 123032. DOI: 10.1103/PhysRevD.106.123032. URL: https://link.aps.org/doi/10.1103/PhysRevD.106.123032.

[29] F. et al. Aharonian. "Observations of the Crab Nebula with H.E.S.S.". In: *Astron. Astrophys.* 457 (2006), pp. 899–915. DOI: 10.1051/0004-6361:20065351. arXiv: astro-ph/0607333.

[30] J. Albert et al. "VHE γ-Ray Observation of the Crab Nebula and its Pulsar with the MAGIC Telescope". In: *The Astrophysical Journal* 674.2 (Feb. 2008), p. 1037. DOI: 10.1086/525270. URL: https://dx.doi.org/10.1086/525270.

[31] N. Park. "Performance of the VERITAS experiment". In: *Proceedings, 34th International Cosmic Ray Conference (ICRC2015): The Hague, The Netherlands, July, 30th July - 6th August*. Vol. 34. 2015, p. 771. arXiv: 1508.07070 [astro-ph.IM].

[32] A. Abramowski et al. "H.E.S.S. constraints on Dark Matter annihilations towards the Sculptor and Carina Dwarf Galaxies". In: *Astropart. Phys.* 34 (2011), pp. 608–616. DOI: 10.1016/j.astropartphys.2010.12.006. arXiv: 1012.5602 [astro-ph.HE].

[33] A. Abramowski et al. "Search for dark matter annihilation signatures in H.E.S.S. observations of Dwarf Spheroidal Galaxies". In: *Phys. Rev. D* 90 (2014), p. 112012. DOI: 10.1103/PhysRevD.90.112012. arXiv: 1410.2589 [astro-ph.HE].

[34] H. Abdalla et al. "Searches for gamma-ray lines and 'pure WIMP' spectra from Dark Matter annihilations in dwarf galaxies with H.E.S.S". in: *JCAP* 11 (2018), p. 037. DOI: 10.1088/1475-7516/2018/11/037. arXiv: 1810.00995 [astro-ph.HE].

[35] J. Aleksić et al. "Optimized dark matter searches in deep observations of Segue 1 with MAGIC". in: *JCAP* 1402 (2014), p. 008. DOI: 10.1088/1475-7516/2014/02/008. arXiv: 1312.1535 [hep-ph].

[36] V.A. Acciari et al. "Combined searches for dark matter in dwarf spheroidal galaxies observed with the MAGIC telescopes, including new data from Coma Berenices and Draco". In: *Physics of the Dark Universe* (2021), p. 100912. ISSN: 2212-6864. DOI: https://doi.org/10.1016/j.dark.2021.100912. URL: https://www.sciencedirect.com/science/article/pii/S2212686421001370.

[37] M. L. Ahnen et al. "Indirect dark matter searches in the dwarf satellite galaxy Ursa Major II with the MAGIC Telescopes". In: *JCAP* 1803.03 (2018), p. 009. DOI: 10.1088/1475-7516/2018/03/009. arXiv: 1712.03095 [astro-ph.HE].

[38] S. et al. Archambault. "Dark matter constraints from a joint analysis of dwarf Spheroidal galaxy observations with VERITAS". in: *prd* 95.8 (Apr. 2017). DOI: 10.1103/PhysRevD.95.082001. arXiv: 1703.04937 [astro-ph.HE].

[39] Louise Oakes et al. "Combined Dark Matter searches towards dwarf spheroidal galaxies with Fermi-LAT, HAWC, HESS, MAGIC and VERITAS". in: *Proceedings of Science*. 2019.

[40] Celine Armand et al. on behalf of the Fermi-LAT, HAWC, HESS, MAGIC, VERITAS. "Combined Dark Matter searches towards dwarf spheroidal galaxies with Fermi-LAT, HAWC, HESS, MAGIC and VERITAS". in: *Proceedings of Science*. 2021.

[41] Daniel Kerszberg et al. on behalf of the Fermi-LAT, HAWC, HESS, MAGIC, and VERTIAS collaborations. "Search for dark matter annihilation with a combined analysis of dwarf spheroidal galaxies from Fermi-LAT, HAWC, H.E.S.S., MAGIC and VERITAS". in: *Proceedings of Science*. 2023.

[42] A. U. Abeysekara et al. "Observation of the Crab Nebula with the HAWC Gamma-Ray Observatory". In: *The Astrophysical Journal* 843.1 (June 2017), p. 39. DOI: 10.3847/1538-4357/aa7555. URL: https://doi.org/10.3847/1538-4357/aa7555.

[43] Giacomo Vianello et al. *The Multi-Mission Maximum Likelihood framework (3ML)*. 2015. arXiv: 1507.08343 [astro-ph.HE].

[44] Marco Cirelli et al. "PPPC 4 DM ID: a poor particle physicist cookbook for dark matter indirect detection". In: *Journal of Cosmology and Astroparticle Physics* 2011.03 (Mar. 2011). ISSN: 1475-7516. DOI: 10.1088/1475-7516/2011/03/051. URL: http://dx.doi.org/10.1088/1475-7516/2011/03/051.

[45] Alex Geringer-Sameth, Savvas M. Koushiappas, and Matthew Walker. “DWARF GALAXY ANNIHILATION AND DECAY EMISSION PROFILES FOR DARK MATTER EXPERIMENTS”. in: *The Astrophysical Journal* 801.2 (Mar. 2015), p. 74. ISSN: 1538-4357. DOI: 10.1088/0004-637x/801/2/74. URL: http://dx.doi.org/10.1088/0004-637X/801/2/74.

[46] A. Albert et al. “Dark Matter Limits from Dwarf Spheroidal Galaxies with the HAWC Gamma-Ray Observatory”. In: *The Astrophysical Journal* 853.2 (Feb. 2018), p. 154. ISSN: 1538-4357. DOI: 10.3847/1538-4357/aaa6d8. URL: http://dx.doi.org/10.3847/1538-4357/aaa6d8.

[47] V. Bonnivard et al. “Spherical Jeans analysis for dark matter indirect detection in dwarf spheroidal galaxies - Impact of physical parameters and triaxiality”. In: *Mon. Not. Roy. Astron. Soc.* 446 (2015), pp. 3002–3021. DOI: 10.1093/mnras/stu2296. arXiv: 1407.7822 [astro-ph.HE].

[48] M. Ackermann et al. “Searching for Dark Matter Annihilation from Milky Way Dwarf Spheroidal Galaxies with Six Years of Fermi Large Area Telescope Data”. In: *prl* 115.23, 231301 (Dec. 2015), p. 231301. DOI: 10.1103/PhysRevLett.115.231301. arXiv: 1503.02641 [astro-ph.HE].

[49] M. L. Ahnen et al. “Limits to Dark Matter Annihilation Cross-Section from a Combined Analysis of MAGIC and Fermi-LAT Observations of Dwarf Satellite Galaxies”. In: *JCAP* 1602.02 (2016), p. 039. DOI: 10.1088/1475-7516/2016/02/039. arXiv: 1601.06590 [astro-ph.HE].

[50] Javier Rico et al. *gLike: numerical maximization of heterogeneous joint likelihood functions of a common free parameter plus nuisance parameters*. https://doi.org/10.5281/zenodo.4601451. Version v00.09.03. Mar. 2021. DOI: 10.5281/zenodo.4601451. URL: https://doi.org/10.5281/zenodo.4601451.

[51] Tjark Miener and Daniel Nieto. *LklCom: Combining likelihoods from different experiments*. https://doi.org/10.5281/zenodo.4597500. Version v0.5.3. Mar. 2021. DOI: 10.5281/zenodo.4597500. URL: https://doi.org/10.5281/zenodo.4597500.

[52] T. Miener et al. “Open-source Analysis Tools for Multi-instrument Dark Matter Searches”. In: *arXiv e-prints*, arXiv:2112.01818 (Dec. 2021), arXiv:2112.01818. arXiv: 2112.01818 [astro-ph.IM].

[53] Alex Geringer-Sameth and Matthew Koushiappas Savvas M. andWalker. “Dwarf galaxy annihilation and decay emission profiles for dark matter experiments”. In: *Astrophys. J.* 801.2 (2015), p. 74. DOI: 10.1088/0004-637X/801/2/74. arXiv: 1408.0002 [astro-ph.CO].

[54] Gianfranco Bertone, Dan Hooper, and Joseph Silk. “Particle dark matter: evidence, can-

didates and constraints". In: *Physics Reports* 405.5-6 (Jan. 2005), pp. 279–390. ISSN: 0370-1573. DOI: 10.1016/j.physrep.2004.08.031. URL: http://dx.doi.org/10.1016/j.physrep.2004.08.031.

[55] V. Bonnivard et al. "Dark matter annihilation and decay in dwarf spheroidal galaxies: The classical and ultrafaint dSphs". In: *Mon. Not. Roy. Astron. Soc.* 453.1 (2015), pp. 849–867. DOI: 10.1093/mnras/stv1601. arXiv: 1504.02048 [astro-ph.HE].

[56] A. et al. Albert. "Searching for Dark Matter Annihilation in Recently Discovered Milky Way Satellites with Fermi-LAT". in: *Astrophys. J.* 834.2 (2017), p. 110. DOI: 10.3847/1538-4357/834/2/110. arXiv: 1611.03184 [astro-ph.HE].

[57] Mattia Di Mauro and Martin Wolfgang Winkler. "Multimessenger constraints on the dark matter interpretation of the Fermi-LAT Galactic Center excess". In: *prd* 103.12, 123005 (June 2021), p. 123005. DOI: 10.1103/PhysRevD.103.123005. arXiv: 2101.11027 [astro-ph.HE].

[58] HongSheng Zhao. "Analytical models for galactic nuclei". In: *Mon. Not. Roy. Astron. Soc.* 278 (1996), pp. 488–496. DOI: 10.1093/mnras/278.2.488. arXiv: astro-ph/9509122 [astro-ph].

[59] H. C. Plummer. "On the Problem of Distribution in Globular Star Clusters: (Plate 8.)" In: *Monthly Notices of the Royal Astronomical Society* 71.5 (Mar. 1911), pp. 460–470. ISSN: 0035-8711. DOI: 10.1093/mnras/71.5.460. eprint: https://academic.oup.com/mnras/article-pdf/71/5/460/2937497/mnras71-0460.pdf. URL: https://doi.org/10.1093/mnras/71.5.460.

[60] Daniel R. Hunter. "Derivation of the anisotropy profile, constraints on the local velocity dispersion, and implications for direct detection". In: *JCAP* 02 (2014), p. 023. DOI: 10.1088/1475-7516/2014/02/023. arXiv: 1311.0256 [astro-ph.CO].

[61] Barun Kumar Dhar and Liliya L. R. Williams. "Surface mass density of the Einasto family of dark matter haloes: are they Sersic-like?" In: *Mon. Not. Roy. Astron. Soc.* (2010). DOI: 10.1111/j.1365-2966.2010.16446.x.

[62] M. Baes and E. Van Hese. "Dynamical models with a general anisotropy profile". In: *Astron. Astrophys.* 471 (2007), p. 419. DOI: 10.1051/0004-6361:20077672. arXiv: 0705.4109 [astro-ph].

[63] Matthew G. Walker, Edward W. Olszewski, and Mario Mateo. "Bayesian analysis of resolved stellar spectra: application to MMT/Hectochelle observations of the Draco dwarf spheroidal". In: *mnras* 448.3 (Apr. 2015), pp. 2717–2732. DOI: 10.1093/mnras/stv099. arXiv: 1503.02589 [astro-ph.GA].

[64] Nicholas L. Rodd et al. "Dark matter spectra from the electroweak to the Planck scale". In:

J. High Energy Physics 121.10.1007 (June 2021).

[65] Pace, Andrew B and Strigari, Louis E. "Scaling relations for dark matter annihilation and decay profiles in dwarf spheroidal galaxies". In: *Monthly Notices of the Royal Astronomical Society* 482.3 (Oct. 2018), pp. 3480–3496. ISSN: 0035-8711. DOI: 10.1093/mnras/sty2839.

[66] Albert, A. et al. "Search for gamma-ray spectral lines from dark matter annihilation in dwarf galaxies with the High-Altitude Water Cherenkov observatory". In: *Phys. Rev. D* 101 (10 May 2020), p. 103001. DOI: 10.1103/PhysRevD.101.103001. URL: https://link.aps.org/doi/10.1103/PhysRevD.101.103001.

[67] Victor Eijkhout and Edmund Show and Robert van de Geijn. *The Science of Computing. The Art of High Performance Computing*. Vol. 3. Open Copy published under CC-BY 4.0 license, 2023, pp. 63–66.